Continued Monitoring of the Varina-Enon Bridge: Estimation of Effective Prestress

http://www.virginiadot.org/vtrc/main/online_reports/pdf/22-r23.pdf

SETH LINDLEY
Associate II, Wiss, Janney, Elstner, Inc.

RACHEL BRODSKY
Structural Engineer, EIT, Jacobs

ANKUJ DAHIYA
Graduate Research Assistant, Charles E. Via, Jr. Department of Civil & Environmental Engineering
Virginia Tech

CARIN L. ROBERTS-WOLLMANN, Ph.D., P.E.
Professor, Charles E. Via, Jr. Department of Civil & Environmental Engineering
Virginia Tech

IOANNIS KOUTROMANOS, Ph.D.
Associate Professor, Charles E. Via, Jr. Department of Civil & Environmental Engineering
Virginia Tech

Final Report VTRC 22-R23

Standard Title Page - Report on Federally Funded Project

1. Report No.: FHWA/VTRC 22-R23	2. Government Accession No.:	3. Recipient's Catalog No.:
4. Title and Subtitle: Continued Monitoring of the Varina-Enon Bridge: Estimation of Effective Prestress		5. Report Date: March 2022
		6. Performing Organization Code:
7. Author(s): Seth Lindley, Rachel Brodsky, Ankuj Dahiya, Carin L. Roberts-Wollmann, Ph.D., P.E., and Ioannis Koutromanos, Ph.D.		8. Performing Organization Report No.: VTRC 22-R23
9. Performing Organization and Address: Virginia Transportation Research Council 530 Edgemont Road Charlottesville, VA 22903		10. Work Unit No. (TRAIS):
		11. Contract or Grant No.: 114321
12. Sponsoring Agencies' Name and Address: Virginia Department of Transportation Federal Highway Administration 1401 E. Broad Street 400 North 8th Street, Room 750 Richmond, VA 23219 Richmond, VA 23219-4825		13. Type of Report and Period Covered: Final Contract
		14. Sponsoring Agency Code:

16. Abstract:

Prestress loss due to creep, shrinkage, and relaxation can cause serviceability issues, and in the case of structures post-tensioned with unbonded tendons, can reduce the flexural capacity. The accurate estimation of prestress losses is vital for making good decisions about the remaining life of a structure. The Varina-Enon Bridge is a post-tensioned concrete box-girder bridge near Richmond, Virginia. Flexural cracks in the bridge prompted an investigation into the magnitude of prestress loss experienced by the structure.

Long-term prestress losses were estimated using two methods. First, a finite element model was created, and multiple code expressions for creep and shrinkage were applied to a time-step analysis of the structure. The code expressions investigated in this research were from the CEB-FIP 1978, CEB-FIP 1990, CEB-FIP 2010, and AASHTO (2017) codes. The second method utilized data from sensors installed on the bridge to back-calculate the effective prestressing force based on recorded openings of the flexural cracks.

For the four spans monitored in this research, the field-determined effective prestress varied between 161 ksi and 166 ksi. Using the commercially available bridge design software, LARSA 4D, along with the creep and shrinkage model used in the original design, CEB-FIP 1978, the calculated effective prestress varied between 169 ksi and 171 ksi. This indicates that prestress losses were higher than anticipated in the original design, but the measured effective prestress was still, on average, about 96% of the design effective prestress. The more modern creep and shrinkage models of CEB-FIP 1990 and CEB-FIP 2010 also predicted higher than measured effective prestress, with both being very similar to CEB-FIP 1978. The effective prestress predicted by the AASHTO (2017) model was slightly higher. Calculation of flexural capacity using the effective prestress estimated by the field measurement system resulted in estimates of strength 1 to 4% smaller than using the effective prestress estimated by the original creep and shrinkage model used for design.

Measured thermal gradients over the period studied in this project were smaller than the AASHTO LRFD design gradients; however, the restraint moment calculated for the worst case measured gradient was very similar to the restraint moment calculated using the design gradient.

17 Key Words: prestress loss, effective prestress, creep, shrinkage, post-tensioned concrete, thermal gradient	18. Distribution Statement: No restrictions. This document is available to the public through NTIS, Springfield, VA 22161.		
19. Security Classif. (of this report): Unclassified	20. Security Classif. (of this page): Unclassified	21. No. of Pages: 68	22. Price:

Form DOT F 1700.7 (8-72)   Reproduction of completed page authorized

FINAL REPORT

**CONTINUED MONITORING OF THE VARINA-ENON BRIDGE:
ESTIMATION OF EFFECTIVE PRESTRESS**

Seth Lindley
Associate II
Wiss, Janney, Elstner, Inc.

Rachel Brodsky
Structural Engineer, EIT
Jacobs

Ankuj Dahiya
Graduate Research Assistant
Charles E. Via, Jr. Department of Civil & Environmental Engineering
Virginia Tech

Carin L. Roberts-Wollmann, Ph.D., P.E.
Professor
Charles E. Via, Jr. Department of Civil & Environmental Engineering
Virginia Tech

Ioannis Koutromanos, Ph.D.
Associate Professor
Charles E. Via, Jr. Department of Civil & Environmental Engineering
Virginia Tech

DISCLAIMER

The project that is the subject of this report was done under contract for the Virginia Department of Transportation, Virginia Transportation Research Council. The contents of this report reflect the views of the authors, who are responsible for the facts and the accuracy of the data presented herein. The contents do not necessarily reflect the official views or policies of the Virginia Department of Transportation, the Commonwealth Transportation Board, or the Federal Highway Administration. This report does not constitute a standard, specification, or regulation. Any inclusion of manufacturer names, trade names, or trademarks is for identification purposes only and is not to be considered an endorsement.

Each contract report is peer reviewed and accepted for publication by staff of Virginia Transportation Research Council with expertise in related technical areas. Final editing and proofreading of the report are performed by the contractor.

ABSTRACT

Prestress loss due to creep, shrinkage, and relaxation can cause serviceability issues, and in the case of structures post-tensioned with unbonded tendons, can reduce the flexural capacity. The accurate estimation of prestress losses is vital for making good decisions about the remaining life of a structure. The Varina-Enon Bridge is a post-tensioned concrete box-girder bridge near Richmond, Virginia. Flexural cracks in the bridge prompted an investigation into the magnitude of prestress loss experienced by the structure.

Long-term prestress losses were estimated using two methods. First, a finite element model was created, and multiple code expressions for creep and shrinkage were applied to a time-step analysis of the structure. The code expressions investigated in this research were from the CEB-FIP 1978, CEB-FIP 1990, CEB-FIP 2010, and AASHTO (2017) codes. The second method utilized data from sensors installed on the bridge to back-calculate the effective prestressing force based on recorded openings of the flexural cracks.

For the four spans monitored in this research, the field-determined effective prestress varied between 161 ksi and 166 ksi. Using the commercially available bridge design software, LARSA 4D, along with the creep and shrinkage model used in the original design, CEB-FIP 1978, the calculated effective prestress varied between 169 ksi and 171 ksi. This indicates that prestress losses were higher than anticipated in the original design, but the measured effective prestress was still, on average, about 96% of the design effective prestress. The more modern creep and shrinkage models of CEB-FIP 1990 and CEB-FIP 2010 also predicted higher than measured effective prestress, with both very similar to CEB-FIP 1978. The effective prestress predicted by the AASHTO (2017) model was slightly higher.

Calculation of flexural capacity using the effective prestress estimated by the field measurement system resulted in estimates of strength 1 to 4% smaller than using the effective prestress estimated by the original creep and shrinkage model used for design.

Measured thermal gradients over the period studied in this project were smaller than the AASHTO LRFD design gradients; however, the restraint moment calculated for the worst case measured gradient was very similar to the restraint moment calculated using the design gradient.

FINAL REPORT

CONTINUED MONITORING OF THE VARINA-ENON BRIDGE:
ESTIMATION OF EFFECTIVE PRESTRESS

Seth Lindley
Associate II
Wiss, Janney, Elstner, Inc.

Rachel Brodsky
Structural Engineer, EIT
Jacobs

Ankuj Dahiya
Graduate Research Assistant
Charles E. Via, Jr. Department of Civil & Environmental Engineering
Virginia Tech

Carin L. Roberts-Wollmann, Ph.D., P.E.
Professor
Charles E. Via, Jr. Department of Civil & Environmental Engineering
Virginia Tech

Ioannis Koutromanos, Ph.D.
Associate Professor
Charles E. Via, Jr. Department of Civil & Environmental Engineering
Virginia Tech

INTRODUCTION

The Varina-Enon Bridge is a post-tensioned concrete box-girder bridge in Richmond, Virginia. Flexural cracks in the bridge prompted an investigation into the magnitude of prestress loss experienced by the structure. In this research, long-term prestress losses were estimated using two methods. First, a finite element model was created, and multiple code expressions for creep and shrinkage were applied to a time-step analysis of the structure. The code expressions investigated in this report were from the CEB-FIP 1978, CEB-FIP 1990, CEB-FIP 2010 and AASHTO (2017) codes. The second method utilized data from sensors installed on the bridge to back-calculate the effective prestressing force based on recorded openings of the flexural cracks.

Prestressed Concrete

Prestressed concrete is a composite material, which utilizes steel strands to provide a pre-compression to concrete elements. This technique produces lighter and stiffer concrete structures. Patents for prestressed technology were filed as early as 1886, but wide use of

1

prestressed concrete was limited throughout the early 20th century because prestress losses were significant in relation to the ultimate strength of the steel strands. With the advent of high-strength steels, however, the use of prestressed concrete became widespread in Europe and America starting in the 1940s. (Naaman, 2012).

Prestressed concrete is placed into two categories: pretensioned and post-tensioned, depending on the construction process. Pretensioned concrete elements are typically fabricated in a precast plant. The high-strength strands are tensioned and anchored at temporary abutments. Then, non-prestressed reinforcement is placed, the forms are constructed, and the concrete is placed around the pretensioned strands. After the concrete has achieved an adequate strength, the exposed strands between the end of the element and the abutment are cut. The prestressing force is transferred into the concrete by the bond between the strand and concrete. Post-tensioned elements can be cast-in-place or precast, and contain empty ducts to accommodate the prestressing strands. In post-tensioned concrete, each duct typically holds more than one strand, and these multi-strand groups are referred to as tendons. Once the concrete achieves adequate strength, the tendons are threaded into the ducts, anchored at one end (referred to as the dead end), stressed, and then anchored at the opposite end (referred to as the live or stressing end). The prestressing force is transferred to the element through anchorage devices. After stressing, the tendons are typically grouted to provide corrosion protection, and for tendons internal to the concrete cross-section, to provide bond. Tendons that are external to the concrete cross-section, such as those in the Varina-Enon Bridge, are grouted, but considered to be unbonded.

Since its inception, prestressed concrete has been adopted in every major building sector. It has been exceptionally effective in the Federal Highway System, where it is a common method for constructing short to medium span bridges. As this infrastructure ages, however, it is important that engineers are able to accurately assess the remaining service life of prestressed bridges. One key aspect of the structural evaluation of prestressed bridges is the accurate prediction of prestress losses. Significant prestress losses can affect the serviceability of structures by causing cracking and excessive deflections, while, in structures post-tensioned with unbonded tendons, prestress losses can also reduce the structures' ultimate strength.

Prestress Loss

Prestress losses in concrete structures come from multiple sources, including instantaneous losses from friction and seating and long-term losses from creep, shrinkage and relaxation. Of these, the long-term losses caused by creep and shrinkage are the most difficult to predict.

Total prestress loss for a post-tensioned concrete structure is generally categorized into instantaneous losses and long-term losses, as seen in Equation 1. Instantaneous losses occur during the construction process, or shortly thereafter, and include friction and seating losses, and elastic shortening losses. The mechanics of these losses are well known and, therefore, will not be explained at length in this report. On the other hand, long-term losses, which are the focus of this study, begin at the moment of stressing, and continue throughout the life of the structure. These long-term losses are made up of creep losses, shrinkage losses, and relaxation losses. The

seminal document that outlines the methods for calculating prestress loss is ACI 423.10R *Guide to Estimating Prestress Losses* (ACI 423, 2016).

$$\Delta f_{pT} = \Delta f_{pFS} + \Delta f_{pES} + \underbrace{\Delta f_{pCR} + \Delta f_{pSH} + \Delta f_{pRE}}$$

$$\underbrace{\qquad\qquad}_{\text{Instantaneous losses}} \quad \underbrace{\qquad\qquad}_{\text{Long-term losses}}$$

Eqn. 1

where,

Δf_{pFS} = friction and seating losses
Δf_{pES} = elastic shortening losses
Δf_{pCR} = creep losses
Δf_{pSH} = shrinkage losses
Δf_{pRE} = relaxation losses

Instantaneous Prestress Losses

As tendons are stressed, they rub against the duct and some of the tendon stress is lost to the friction in this interaction. Losses could be due to the friction from intentional curvature in a tendon profile, or due to unintentional curvature, which is known as wobble, from the duct being misaligned or not adequately supported during the casting process. Seating losses result from slippage that occurs when the strand is released from the stressing jack. The amount of curvature friction influences how far seating losses extend through the length of the tendon. Lastly, losses due to elastic shortening of concrete occur in post-tensioned structures when tendons are stressed sequentially. As the first tendon in a span is stressed, the surrounding concrete is put into compression. When the second tendon is stressed, the first tendon experiences elastic shortening loss as the concrete is put into further compression. When the third tendon is stressed, the first and second tendons experience elastic shortening loss, and so on. Elastic shortening loss in each tendon is considered to be uniform through the length of the span.

Long Term Losses

Creep is a length change that occurs due to loading applied over an extended period of time. Shrinkage is a volumetric change that occurs due to the loss of water in the pore structure of the concrete. These phenomena result in a shortening of the prestressed member causing long-term losses in the prestressing strands. These long-term losses are estimated using analytical models, which describe the development of creep and shrinkage with time.

Creep and shrinkage cause strains that progress at a decreasing rate over time, as seen in Figure 1. A number of analytical models have been developed over the years to describe this process, all of which take into account material properties and environmental conditions. Each model, however, considers slightly different aspects of the material and uses different functions to describe the progression of creep and shrinkage with time.

Creep is described analytically by a stress-independent term called the compliance function, $J(t,t_o)$. This function describes creep strain for unit stress and thus can be used to model

creep strains for any given stress. A generalized version of the compliance function is shown in Equation 2, where $\phi(t,t_o)$ represents the creep coefficient, and E_x represents some variation of the elastic modulus. Additionally, the term, t, represents the time of interest, and t_o represents the
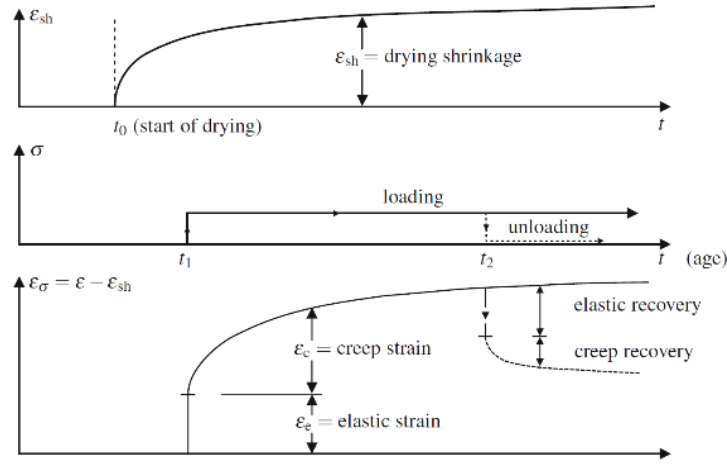

Figure 1. Creep and Shrinkage Response with Respect to Time (Bažant and Jirasek 2018).

time when the structure was loaded, both in units of days. The compliance function for each model code varies, depending on what value of elastic modulus is used, and how the creep coefficient is calculated.

$$J(t,t_o) = \frac{1 + \phi(t,t_o)}{E_x}$$

Eqn. 2

Because shrinkage does not depend on the stress in the concrete, strains due to shrinkage are simply a function of the time of drying, the material properties and the environmental conditions. Total shrinkage strains, $\varepsilon_{sh}(t,t_o)$, are defined in all models by a bounded function that approaches some ultimate value.

Several methods for calculating long-term prestress losses have been developed over the years. At the beginning of code development, long-term losses were calculated as a lump-sum value that depended only on the level of stress in the steel and concrete. These calculations were first outlined by the Bureau of Public Roads in 1954 and can be seen in Equation 3. This method, however, does not take into account any of the properties of the concrete itself and is only used today for preliminary design.

$$\Delta f_{pT} = 3000 + 11 f_{cps} + 0.04 f_{pi} \quad \text{(psi)}$$

Eqn. 3

where:

f_{cps} = the concrete stress at the center of gravity of the prestressing force due to all loads.

f_{pi} = the initial stress in the prestressing steel.

4

A simplified method for estimating long-term losses is allowed for structures under normal design conditions. This method is more accurate than the lump-sum method and is accepted in modern design but makes many simplifying assumptions about material properties. This method intends to "reasonably estimate" the losses due to creep, shrinkage, and relaxation individually. Losses depend primarily on factors for creep, shrinkage, and relaxation that are taken from tables and depend on the type of concrete, the age at load application, and the type of prestressing steel (ACI 423, 2016).

The most accurate methods of estimating prestress loss directly consider the creep, shrinkage, and relaxation models for the materials being used. These methods can generally be categorized into time-step methods and age-adjusted effective modulus methods. The age-adjusted effective modulus method modifies the modulus of elasticity using the creep coefficient and a term called the aging coefficient (χ) to calculate the total long-term strains due to a load. This age-adjusted modulus can be seen in Equation 4.

$$E''_c = \frac{E_c}{1 + \chi \phi\left(t, t_0\right)}$$ Eqn. 4

The time-step method, like the age-adjusted effective modulus method, directly utilizes creep and shrinkage models. This method is unique in that it breaks the life of the structure down into discrete periods of time and calculates the creep and shrinkage strains at each discrete time step. The time-dependent strains are then added to the mechanical strains to determine the total change in length and curvature of the structure. The prestress losses are then used to update the stresses for use in the next time-step calculation. This incremental process accounts for the fact that the rate of prestress loss due to one effect, such as creep, is altered by losses due to the other two effects, such as relaxation and shrinkage (Naaman, 2012). Most commercially available bridge design software use the time-step method for time dependent analysis.

Thermal Gradients

Thermal gradients play an important role in understanding the flexural behavior of large, box-girder bridges. Specifically for the Varina-Enon Bridge (VEB), the stresses induced by non-linear thermal gradients have been shown to be significant (Maguire et al., 2014).

Throughout a given day, the temperature through the depth of a concrete box girder may vary. This temperature differential is termed a thermal gradient and can be influenced by many factors, as seen in Figure 2. Energy from solar radiation is absorbed on the top surface, while
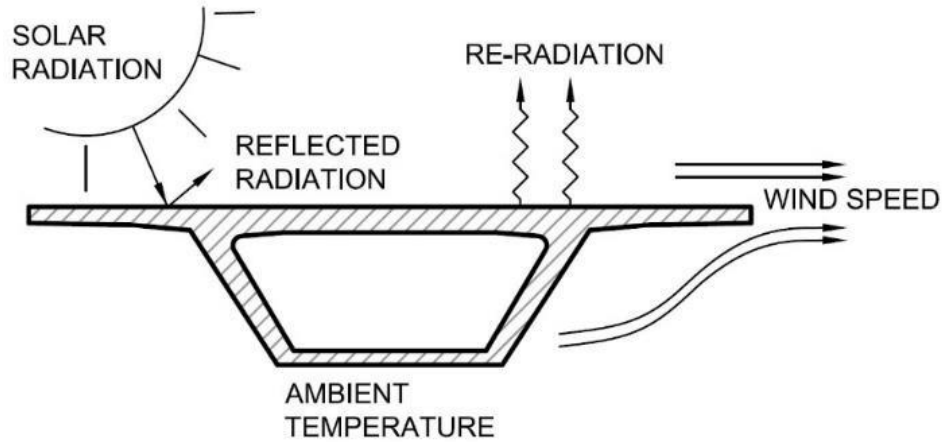
**Figure 2. Factors Affecting Thermal Gradients**

energy is gained and lost to the surrounding environment through convection and conduction (Imbsen et al., 1985). Thermal gradients can be linear or non-linear, depending on environmental and geometric conditions.

Large box girders tend to experience non-linear thermal gradients on sunny days with high temperature fluctuations. This is the result of their large top flange, which is exposed directly to solar radiation and which tends to shade the webs and bottom flange. Stresses, resulting from non-linear thermal gradients are divided into self-equilibrating (SE) stresses and continuity stresses as outlined in NCHRP Report 276 (Imbsen et al., 1985). Once these values are calculated, the principle of superposition is used to sum them together to get the total stress distribution due to the thermal gradient.

SE stresses arise from the difference between thermal strains, which would result from a free expansion of the section fibers, and the strains in the resultant plane section (Imbsen et al., 1985). SE stresses can also be conceptualized as the stresses due to the thermal gradient in an artificially restrained structure plus the stresses resulting from the axial load and moment that would be required to remove the artificial restraints, as illustrated in Figure 3. These stresses can also be thought of as the difference between the free deformations of section fibers due to the non-linear thermal gradient, and the linear strain profile assumed by the Navier-Bernoulli assumption that plane sections remain plane.

ΔT
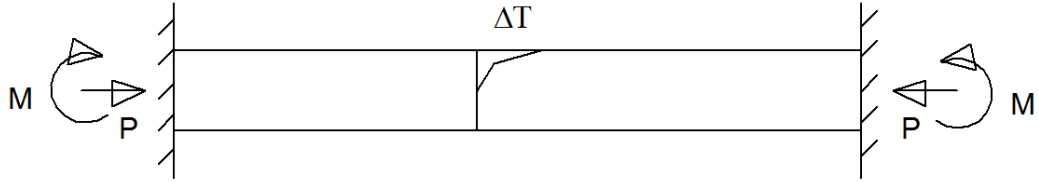
Beam with Non-linear Thermal Gradient in Artificially Restrained Condition
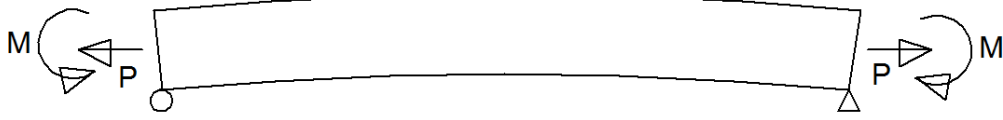
Beam with Artificial Restraints Removed
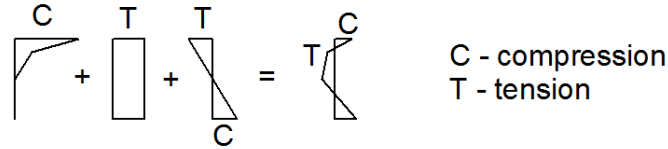
C - compression
T - tension

$$E\alpha\Delta T + \frac{P}{A} + \frac{My}{I} = self\ equilibrating\ stresses$$

Figure 3. Calculation of Self-Equilibrating Stresses from a Non-Linear Thermal Gradient.
M = moment, P = axial force, E = modulus of elasticity, α = coefficient of thermal expansion,
ΔT = temperature difference with respect to reference temperature, A = cross-sectional area,
I = moment of inertia, y = distance from centroid of section to point under consideration

To calculate the self-equilibrating stresses, first the stress at any depth, *y*, in the fully restrained system is calculated using Equation 5.

$$\sigma(y) = E \cdot \alpha \cdot \Delta T(y) \qquad\qquad \text{Eqn. 5}$$

where:
$\sigma(y)$ = the stress in the fully restrained system at a distance y from the centroid of the cross-section
E = the modulus of elasticity of the material
α = the coefficient of thermal expansion of the material
$\Delta T(y)$ = temperature at a distance y from the centroid of the cross-section

To calculate the restraint force and moment, the stresses must be integrated through the depth of the cross-section as presented in Equation 6 and 7.

$$P = E \cdot \alpha \cdot \int_{-y}^{+y} \Delta T(y)b(y)\ dy \qquad\qquad \text{Eqn. 6}$$

$$M = E \cdot \alpha \cdot \int_{-y}^{+y} \Delta T(y)b(y)y\ dy \qquad\qquad \text{Eqn. 7}$$

where:
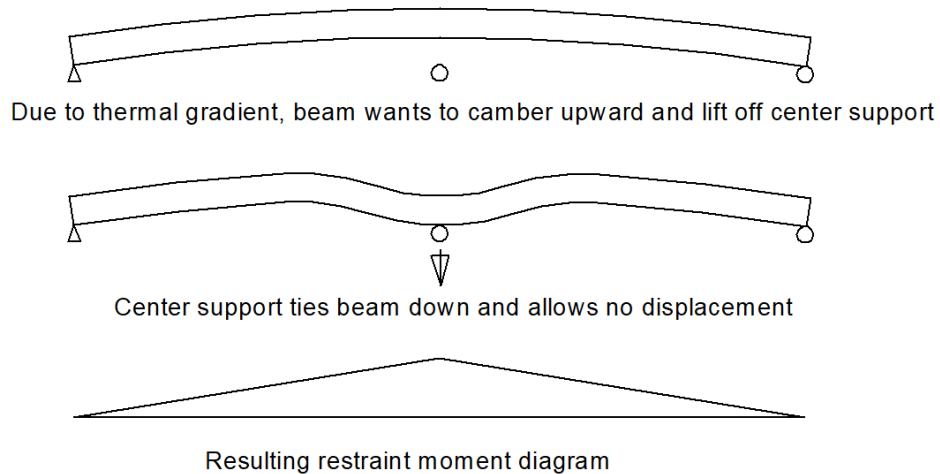P = the force required to fully restrain axial expansion of the member
M = the moment required to fully restrain curvature of the member
$b(y)$ = width of the cross-section at a distance y from the centroid of the cross-section
$-y$ = distance from the centroid to the bottom of the section

7

$+y$ = distance from the centroid to the top of the section

When redundancies are added into the structure, continuity stresses will be induced in addition to self-equilibrating stresses. This scenario can be visualized by considering a two-span continuous beam as shown in Figure 4. When subjected to a positive thermal gradient, and if the center support could not restrain the movement, the beam would camber up from exterior support to exterior support and lift off the interior support. However, the beam cannot lift off its supports due to its own self-weight reaction, so the movement is restrained by a hold-down force at the interior pier. This force could be calculated as the force required to return the structure to zero displacement at the interior support. This force causes a positive moment to develop along the length of the beam. This is known as the thermal continuity restraint moment,

Due to thermal gradient, beam wants to camber upward and lift off center support

Center support ties beam down and allows no displacement

Resulting restraint moment diagram

Figure 4. Thermal Restraint Moment

and the stresses that are generated from this moment are the thermal continuity stresses. The total thermal stresses are the sum of the self-equilibrating and continuity stresses.

Varina-Enon Bridge

The Varina-Enon Bridge (VEB) is a cable-stayed, segmentally-constructed, post-tensioned box-girder bridge. The VEB spans the James River, connecting Chesterfield and Henrico Counties in Virginia at mile marker 18 along Interstate 295. Figure 5, shows an aerial view of the VEB, which carries six lanes of traffic via two parallel box girders. The VEB was designed by Figg and Muller Inc. beginning in 1985 and was opened to traffic on July 18, 1990.

Figure 5. Aerial View of the Varina-Enon Bridge over the James River

The total length of the bridge is 4,680 ft and it is composed of 28 spans. Seven of these spans make up the cable-stayed, main span of the structure. The remaining 21 spans make up the approach units of the bridge. On the south end of the bridge, two six-span, continuous approach units make up the southernmost 12 spans of the bridge. The focus of this study is on the eastern box-girder in the two southernmost approach units, which carry northbound traffic. These approach units are each made up of six 150-ft spans, resulting in a total length of 900 ft for each unit. Piers and spans are numbered sequentially, beginning with the southernmost elements, as seen in Figure 6 and Figure 7.
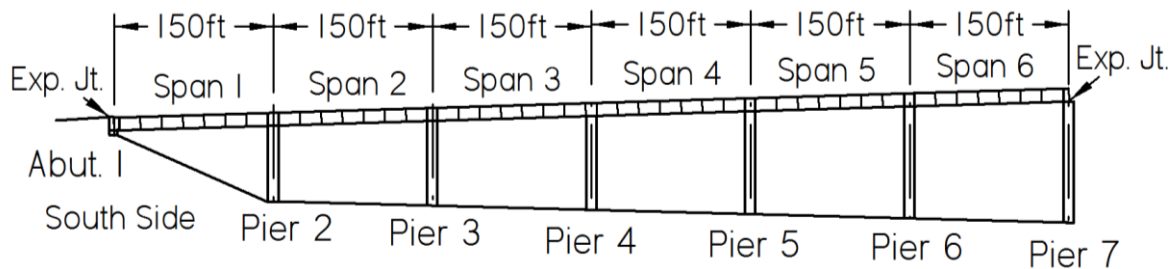
Figure 6. Elevation of the Southernmost Approach Unit
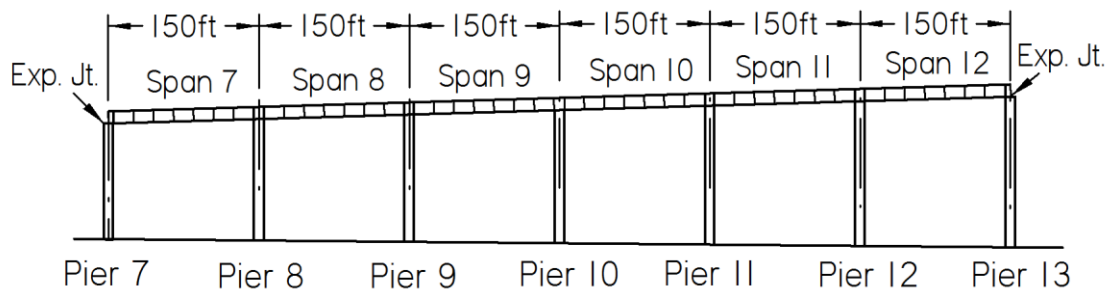
Figure 7. Elevation of the Next Southernmost Approach Unit

9

Each span of the approach units of the VEB is composed of seven 20-ft precast typical segments and two shorter pier segments. These segments were match-cast in a long-run configuration and placed using steel launch trusses (seen in Figure 8). Segments were epoxied at the joints as each was placed, then the span was post-tensioned. The cross-section of a typical precast segment is shown in Figure 9. Pier segments, which are located atop each pier, have the same outer dimensions as the typical segments but contain diaphragms on the interior, which act as anchorages for the longitudinal post-tensioning.
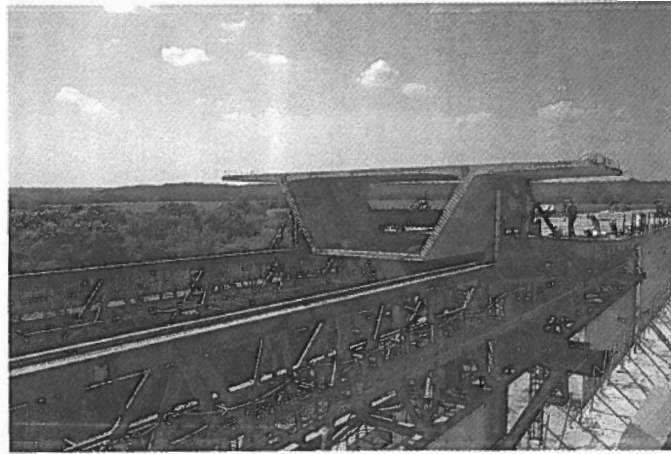
**Figure 8. Construction of Varina-Enon Approach Spans (Photo courtesy of FIGG)**
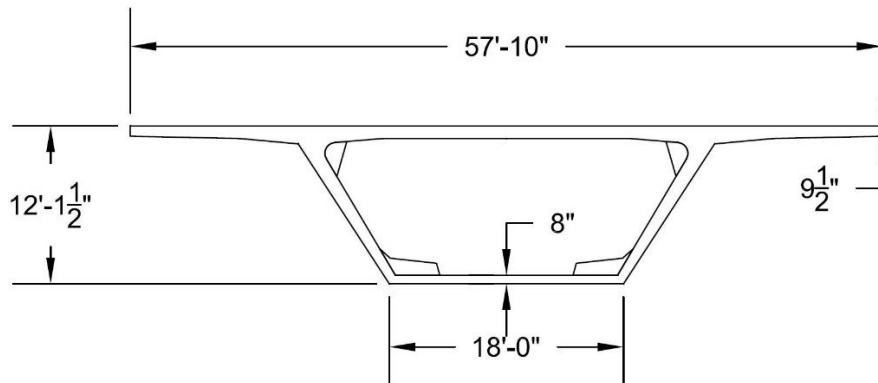
Figure 9. Typical Approach-Unit, Precast Segment

Longitudinal post-tensioning of the VEB consists of eight external tendons in each span. Each tendon contains (19) 0.6-in diameter 7-wire strands. Tendons are located in the interior of the box girder cell and are deviated via blocks at the bottom of the section, as seen in Figure 10, which shows the configuration of tendons in Span 6. Figure 10 also illustrates how the tendons provide continuity to the structure over pier supports. At the location of Pier 6, the tendons in Span 5 and Span 6 overlap in the diaphragm of the pier segment. As each span was constructed, this overlap provided continuity to the structure.

10
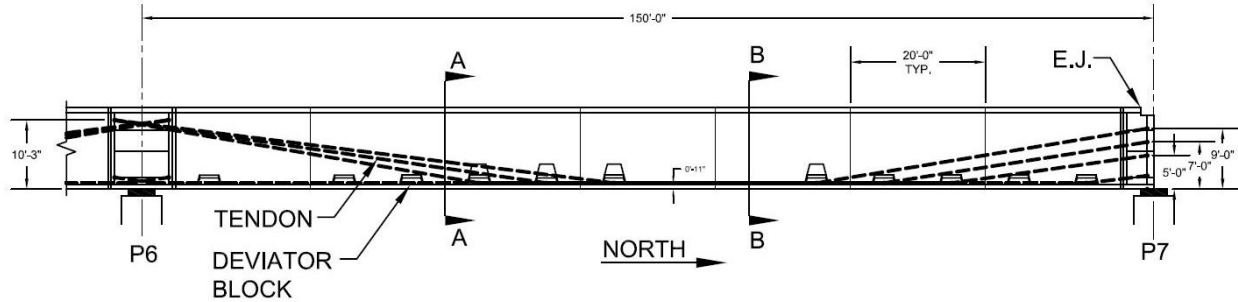
Figure 10. Section View of Span 6, (Tendons Shown by the Dashed Lines)

The performance of the Varina-Enon Bridge (VEB) came into question after a crack at a joint between two segments in Span 6 of the northbound approach unit was identified by the Virginia Department of Transportation in 2012. This crack was observed by inspectors to open and close under traffic. In addition, cracks in Span 5, Span 9 and Span 11 have been identified during inspections. There have been no observed occurrences of these cracks opening and closing under traffic. Though these cracks were partially attributed to large thermal gradients, the literature suggests that large segmentally-constructed box girders experience larger-than-expected creep deflections (Bažant et al., 2010). With this in mind, it is vital that the effective prestress of the VEB be assessed accurately. At 31 years old, the VEB should remain in service for decades to come. Left unchecked, however, excessive prestress loss can shorten the life of the bridge and reduce the flexural strength.

Previous Investigation of the Varina-Enon Bridge

Maguire et al. (2014) investigated the longitudinal behavior of the VEB under live-load testing after a 1/16-in crack was identified in the bottom flange of Span 6 of the northbound approach of the VEB. In addition to live-load testing, a long-term monitoring system was set up on the VEB to log crack opening events, and the thermal gradients associated with these events. The long-term monitoring system consisted of 27 thermocouples spread throughout the depth of the box girder, two strain transducers, and two Linear Variable Differential Transformers (LVDTs). Researchers concluded that crack openings were generally correlated with large non-linear thermal gradients in the bridge (Maguire et al. 2018) occurring simultaneously with large live load events.

In addition to thermal gradients, the issue of crack openings could also be the result of larger-than-expected prestress losses in the longitudinal post-tensioning tendons. In 2017, the long-term monitoring data was re-evaluated in an effort to calculate the effective prestress force. The study used simple beam line models to prove the concept that the field data could be used to back-calculate the effective prestress force. It was shown that with crack openings larger than 0.004 in, the back calculated forces converged to a consistent value. The study indicated that the concept could provide an estimate of effective prestress from crack opening events, but the report was not published because it was very preliminary and used very simple models.

PURPOSE AND SCOPE

The purpose of this research was to investigate the time-dependent longitudinal flexural behavior of the Varina-Enon Bridge, the final goal of which was to estimate the effective longitudinal prestress losses using existing flexural cracks, and to compare these losses to those estimated by a finite element model of the six-span approach units. The scope of this research included the following:

1. To perform additional monitoring of the Varina-Enon Bridge, and to use the collected data to continue to refine models to determine the current level of effective prestress in the bridge. In addition to the span that has been monitored (Span 6 of the northbound structure), other locations where cracks at the match cast joints have been found were monitored.

2. To better quantify the magnitude of the thermal gradients in the bridge and compare to current design gradients and the original gradient used in the design of the bridge.

3. To use the information gathered from the long-term instrumentation to estimate the effective prestress, and use this value to calculate the flexural strength of the bridge at instrumented sections.

METHODS

Overview

The tasks undertaken to achieve the project objectives were as follows:

1. Literature Review – Pertinent literature related to field measurements of prestress losses were reviewed and synthesized. In addition, literature related to previous work on the effect of creep and shrinkage on losses was studied.

2. Maintain and Upgrade Instrumentation Systems - Maintenance of the existing monitoring system was performed as required, with several new sensors added. An additional mobile system was assembled. This system was installed and left in place for four months at one crack location and then moved to a second crack location for the duration of the project.

3. Develop and Validate a LARSA 4D Model of the Bridge – The bridge design software LARSA 4D was used to develop a model of the first two units of the Varina-Enon Bridge. The model was validated using data from a live load test performed in 2012 by Maguire et al. (2014).

4. Back Calculate the Effective Prestress from Measured Data - A method was developed to use the measured data in conjunction with information from the LARSA 4D model

to back calculate the effective prestress in all monitored spans in which the cracks opened.

5. Compare Field Determined Effective Prestress to Other Models - Once the effective prestress was estimated, the detailed model which was developed in LARSA 4D was used to determine if the original creep and shrinkage model, CEB MC-78, adequately predicted the loss. The data-derived effective prestress was also compared to other creep and shrinkage models.

6. Estimate Future Losses and the Effect on Flexural Strength – The original design creep and shrinkage model was used to project into the future to determine the expected additional loss of prestress over time. This effective prestress was used to calculate flexural strength along with the data-derived effective prestress.

7. Compare Design Thermal Gradients to Measured - The thermal gradients that were measured with the long-term instrumentation system were analyzed and compared to the current AASHTO design gradient and the gradient used for the original design.

Literature Review

Pertinent literature was reviewed by using available databases to search for previous works in several areas such as:

- Methods employed to measure effective prestress in existing structures,
- Creep and shrinkage models previously and currently employed for segmental bridge design,
- Previous investigations of prestress losses in long span bridges.

Maintain and Upgrade Instrumentation Systems

The monitoring system set up in Span 6 by Maguire et al. (2014) gave reliable data for all of 2013, but started to malfunction in 2014. This system was fixed and reinstalled in Span 6 along with a new sensor across the crack in Span 5 in 2019 (Lindley, 2019). A system to monitor the crack in Span 9 was installed in the spring of 2020 (Brodsky, 2020), and was then moved to Span 11 in the summer of 2020 (Dahiya, 2021). Each span and the period of time over which the crack was monitored is presented in Table 1. Details of the instrumentation for each span are presented in this section.

Table 1. Dates Over Which Spans Were Monitored

Span Number	Date of system installation	Date of system removal
5	March 2019	N/A
6	August 2012	February 2015
	March 2019	N/A
9	March 2020	June 2020
11	June 2020	N/A

Span 6

The long-term monitoring system was originally deployed by Maguire et al. (2014) shortly after live load tests had been performed in August of 2012. The original system was designed to measure the number and magnitude of crack-opening events in Span 6. The sensors measured crack displacement, temperature, and live-load strains at the crack location and at the point of theoretical maximum live load moment in Span 6.

An elevation view presenting the locations of the sensors is shown in Figure 11. Section A-A represents the location of the transverse crack being monitored, while Section B-B represents the location of maximum positive live-load moment. Linear variable differential transformers (LVDTs) measured crack opening widths at Section A-A. The LVDTs on the top of the bottom slab were present for all monitoring, and the LVDTs on the bottom of the bottom slab were installed in December of 2020. These LVDTs were installed to determine if there was any lag between the opening of the top-of-slab and bottom-of-slab LVDTs and to confirm that the crack opened completely. In addition, a strain gage was placed adjacent to the crack to measure strain in the longitudinal direction (see Figure 12). Two strain transducers measured live-load strains at Section B-B (see Figure 13). The gage on the top of the bottom slab was present for all of the monitoring presented in this report. The gage on the bottom of the top slab was installed in March 2019.
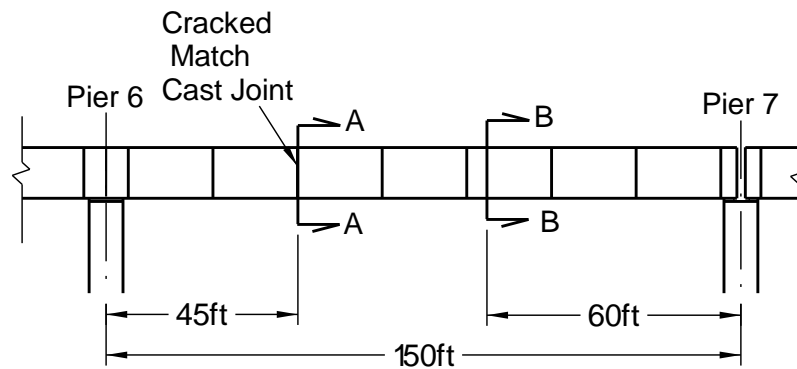
Figure 11. Span 6 Longitudinal Sensor Layout.

Thermocouples were installed throughout the depth of the box-girder section, as seen in Figure 14. Each cluster of thermocouples in the figure represents several sensors installed through the thickness of the flange or web. Each thermocouple was assigned a tributary area over which the temperature of the section was taken to be constant. Table 2 shows the location of each thermocouple from the top of the wearing surface, the tributary area, and the location of the

centroid of that area from the bottom of the section. Each of the values in Table 2 was used in the calculation of the thermal moment and axial force.
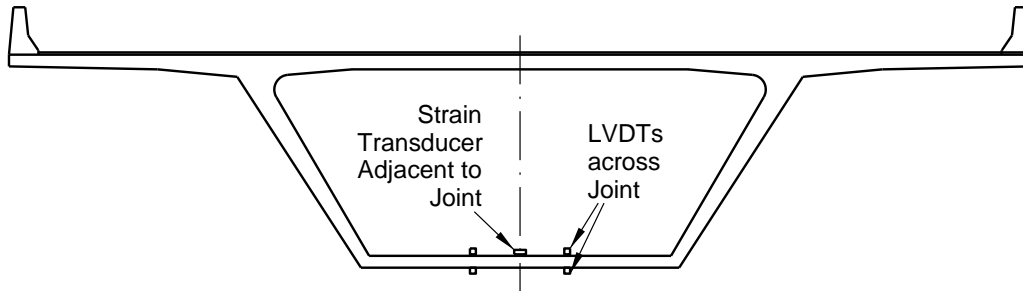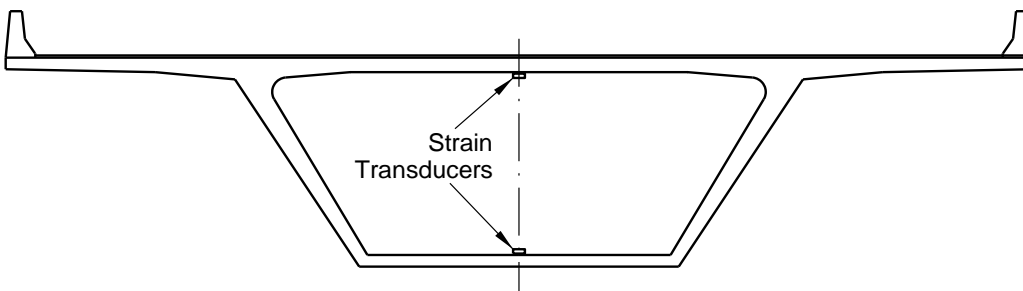

Figure 12. Section A-A Sensor Layout.

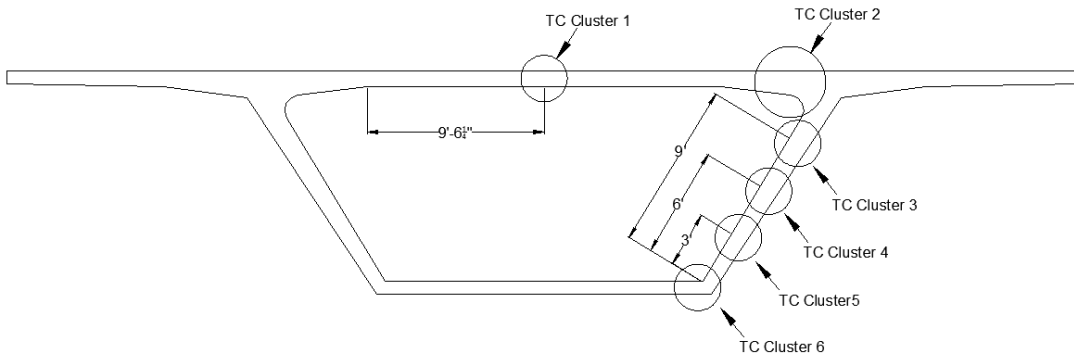**Figure 13. Section B-B Sensor Layout.**


Figure 14. Thermocouples at Section A-A

Several thermocouples in Cluster 1 and Cluster 2 were located at approximately the same depth in the section. These were used to determine if there were any differences in the temperatures in the thin top slab and the thicker web-top flange juncture. In addition, pairs of thermocouples were installed at different depths in the web to determine if there was any significant difference between the temperature on the inside and outside of the web wall. These temperature measurements were averaged and treated as one measurement for subsequent calculations. Thermocouples averaged because of proximity include 4/5, 6/7, and 8/9 in the web and thermocouples 16/21, 17/22, and 18/23 in the top flange. Thermocouple 99 represented an estimated temperature at 3/4 in from the top of the wearing surface. This temperature was interpolated from the existing temperature measurements using the fifth-order curve approximation presented by Priestley (1978).

15

Table 2. Location and Tributary Areas of Thermocouples.

TC Number (Cluster Number)	Elev. from top of wearing surface, in	CG from the bottom, in	Tot area, in²	Area*cg, in³
1 (6)	140.0	8.1	1,086.8	8,838.8
2 (6)	142.3	3.2	496.5	1,602.6
3 (6)	144.5	1.1	457.5	481.4
4 (5)	108.8	35.8	754.9	27,043.1
5 (5)	110.8			
6 (4)	78.0	66.2	848.4	56,156.3
7 (4)	80.6			
8 (3)	48.5	97.5	1,030.0	100,394.8
9 (3)	51.1			
10 (2)	15.8	122.9	667.5	82,040.1
11 (2)	13.8	131.8	317.2	41,810.9
12 (2)	11.8	133.9	673.2	90,158.4
13 (2)	9.8	135.3	713.9	96,594.5
19 (1)	9.5	136.2	692.9	94,363.8
14 (2)	7.8	137.6	1,041.0	143,241.6
15 (2)	6.5	138.9	798.1	110,876.0
16 (2)	5.5	140.0	694.0	97,160.0
21 (1)	5.5			
17 (2)	4.5	141.0	694.0	97,854.0
22 (1)	4.5			
18 (2)	3.5	142.0	694.0	98,548.0
23 (1)	3.5			
24 (1)	2.5	143.7	957.7	137,614.8
99	0.8	145.6	1,131.2	164,666.0

Span 5

Span 5 also has a joint that was cracked (See Figure 15). In this span, one LVDT was placed across the cracked joint, and was connected to the same data acquisition system that recorded the data in Span 6. This LVDT was on the top of the bottom slab.
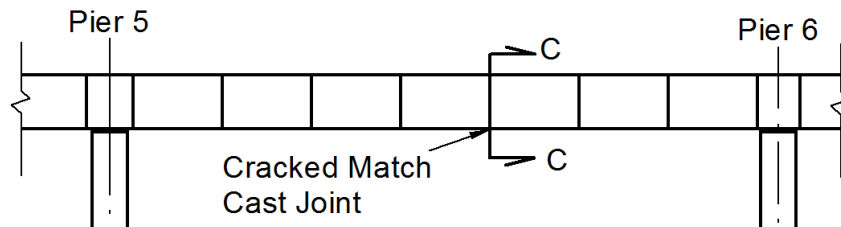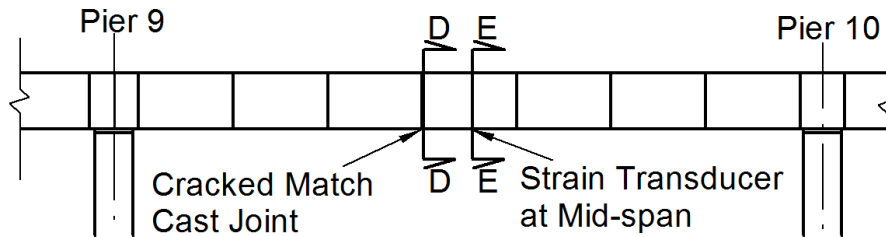

Figure 15. Location of Sensor in Span 5

Span 9

One of the joints in Span 9 was also cracked. Figure 16 is an elevation view of Span 9 indicating the sensor locations. Two LVDTs were placed across the cracked joint (Section D-D), one strain transducer was placed adjacent to the joint to gather information on decompression at the joint, and one strain transducer was placed on the top of the bottom slab at mid-span to act as the triggering gage (Section E-E). These sensors and an original data acquisition system were placed in May of 2019. The original data acquisition system had several technical problems and was replaced with a new system in March of 2020. In June of 2020, the system was moved to Span 11.

Figure 16. Location of Sensors in Span 9

Span 11

Similar to Span 9, one of the joints in Span 11 is also cracked. Figure 17 is an elevation view of Span 11 indicating the sensor locations. There are two LVDTs placed across the cracked joint, one strain transducer was placed adjacent to the joint to gather information on decompression at the joint (Section G-G), and one strain transducer was placed on the bottom slab at mid-span to act as the triggering gage (Section F-F). This system measured events from June 2020 to April 2021.
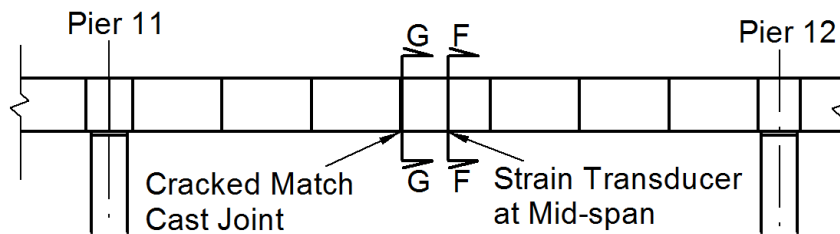

Figure 17. Location of Sensors in Span 11

Data Collection

In Spans 5 and 6, data was collected using two Campbell Scientific CR1000 data loggers. One data logger collected strain and displacement data at a rate of 33 Hz. However, data was only permanently stored on this data logger each time the trigger gage measured a strain of 11 $\mu\varepsilon$ or more. The several seconds of data that was stored is termed a load event for the remainder of this report. The second data logger collected temperature data via an analog multiplexer that sampled every 2 minutes. All of the temperature data was stored continuously in a file separate from the strain data.

In Span 9 and Span 11, a Campbell Scientific CR1000X data logger collected strain and displacement data at a rate of 33 Hz. A load event was put in permanent storage any time the strain at the midspan transducer, the trigger gage, exceeded 11 $\mu\varepsilon$.

Data Processing

Data files were regularly collected from the three data loggers and separated into discrete events by comparing the timestamp on adjacent samples. A new event was defined when the timestamp increased by a value greater than 3/100ths of a second. A thermal gradient was then matched to each event by comparing the timestamp of that event to the timestamps of the temperature data. Finally, descriptive values were extracted from the event and used to characterize it. These values included the timestamp, maximum and minimum values of the trigger gage, the maximum value of strain at the gage adjacent to the crack, and the maximum values of both LVDTs.

Develop and Validate a LARSA 4D Model of the Bridge

A detailed analytical model of the entire Varina-Enon Bridge was developed in a commercially available program, LARSA 4D. Although the full bridge was modeled, only the two approach units on the south side of the bridge in the northbound direction are used in this report. The model of the first unit, Spans 1-6, is shown in Figure 18. There were two purposes for developing this model. First, it was used to calculate prestress losses in the bridge, utilizing multiple creep and shrinkage models. Second, the FEM was used to calculate dead-load moment, prestressing moment, and general moment distributions necessary to calculate effective prestress from the field data. The second unit, Spans 7-12, is identical to the first unit, except for the details of the connection of the box girders to the piers.
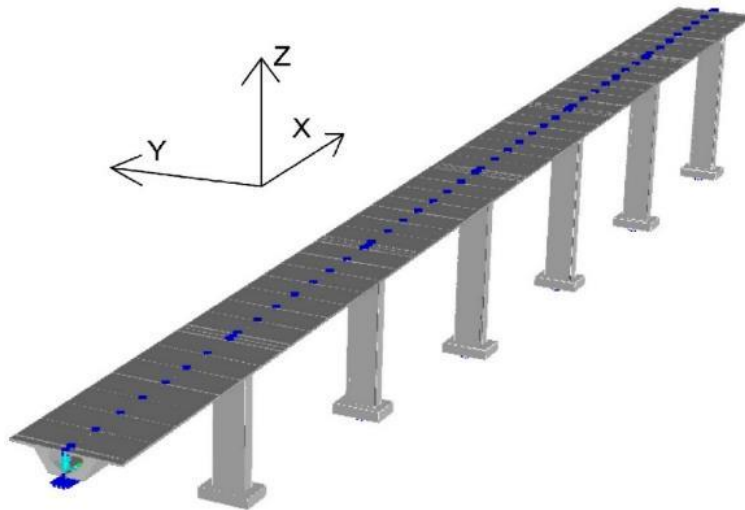

Figure 18. Depiction of the FE Model of Spans 1-6

Finite Element Model Overview

For each unit, the bridge superstructure was modeled as a six-span-continuous beam. Each precast segment was modeled as an individual beam element, which ensured that information at each joint was available. The mean elastic modulus of concrete at 9,500 days was taken as 5,000 ksi. This value was validated by live-load tests conducted by Maguire (2013). The mean 28-day ultimate strength, f'_{cm} was assumed to be 6,600 psi. The cross-sectional dimensions of the superstructure shown in Figure 9 include a 1½-in cast-in-place wearing surface, which was included in the model as dead load, and also contributed to the stiffness of the section.

For the first unit, rigid links were used at pier locations to connect joints at the centroid of the box girder to joints located at the bottom of the box girder where the bearings are located. For the entire first unit, Spans 1-6, springs were used to model the neoprene bearing pads at the joint between these rigid links and the substructure. These springs had translational stiffness in the Z- and X-axes, and rotational stiffness about the Y-axis as referenced by Figure 18. For the remaining three degrees of freedom, the superstructure was rigidly connected to the substructure. Bearing pad stiffnesses for the VEB were characterized by Maguire (2013) and are presented in Table 3.

<div align="center">Table 3. Bearing Pad Stiffnesses (from Maguire 2013)</div>

Location	Height (in)	Vertical Stiffness (kip/in)	Longitudinal Stiffness (kip/in)	Rotational Stiffness (in-kip/rad)
Abutment 1, Pier 7, Pier 13	7.6	26,000	240	1700
Piers 2, 6	4.3	38,500	490	2500
Piers 3, 4, 5	3.0	73,600	630	4900

The interior pier segments in the second unit, Spans 7-12, which are post-tensioned down to the piers, were modeled as fixed connections. The supports at each end of the unit were bearing pads, as shown in Table 3.

Prestressing tendons were modeled from dimensions found in the as-built drawings. Tendon material is A416 low relaxation prestressing steel, which has an ultimate tensile strength of 270 ksi, and an apparent modulus of elasticity of 27,400 ksi. The apparent modulus was calculated using benchmark elongation tests during the construction of the VEB (F&M Engineers, 1993). Actual jacking forces varied slightly for each tendon and were found in the as-built drawings.

All self-weight loads are included in the FE model. In addition to the gross cross section of the box girder, tendon deviation blocks, and barrier rails were incorporated into the model as point and distributed loads. However, the stiffness of the barrier rails was not considered in the overall stiffness of the section.

Staged Construction Analysis

Segmental construction of the VEB was modeled using a time-dependent construction stage analysis. This analysis method accounted for the placement and stressing of each span

during construction, as well as the long-term behavior of the structure due to creep, shrinkage, and relaxation. Several definitions are key to understanding this staged construction analysis. First, construction activities were defined as events that may include placement of an element, addition of a support, or stressing of a tendon. Second, construction steps were defined as an individual analysis and may include several construction activities. Lastly, construction stages were each defined as a group of construction steps and represent one day of construction for purposes of calculating time-dependent behavior.

The construction of each of the approach units was modeled in six stages, each consisting of the construction of one span. Construction of each span consisted of nine construction steps. In the first step, the substructure and superstructure of each span were initiated, and the self-weight was applied. In Steps 2 through 9, each of the eight tendons in the span were stressed. It is necessary to analyze the structure after stressing each tendon to account for elastic shortening losses.

A day-of-casting was assigned to each beam element in the staged construction analysis. This casting day was used to define the age of the element at loading and each subsequent construction stage. Casting dates for each element were obtained from erection logs recorded in the VEB Inspection and Maintenance Manual (F&M Engineers 1993). Day zero was defined as the day that the first superstructure segment was cast, which occurred on August 29th, 1986.

For Spans 1 through 6, the first six construction stages took place from day 554 to 1650. For Spans 7 to 12, the construction stages took place from day 669 to 743. After the construction of the two approach units, the remainder of the bridge was constructed. However, the remaining portions of the bridge model were not used in the analysis presented in this report. Following completion of the bridge, empty construction stages were placed at day 1000 and then 1000 day increments up to 5000 days. Stages were also placed at 9800 days, 12,000 days, 20,000 days, 30,000 days and 36,000 days. These construction stages did not represent any construction activity but were placed as time steps for the time-step analysis. The data recorded in Span 6 in 2013 was compared to FE model results at 9800 days. Data recorded in all spans in 2019 to 2021 was compared to FE model results at 12,000 days.

Short-Term Prestress Losses

Short-term prestress losses were incorporated into the FE model prior to the construction stage analysis. These losses were calculated as the sum of friction, seating, and elastic shortening losses. These losses depended on the stressing operation as well as the modulus of elasticity of the concrete at the time of stressing.

Curvature friction losses are caused by friction between prestressing strands and the inside of the tendon duct at any location that the strand changes direction. The curvature friction coefficient, μ, was measured to be 0.25 during construction (F&M Engineers, 1993). No wobble friction is present in the structure, since the tendons are externally post-tensioned. The solid line in Figure 19 shows an example of a tendon force profile after curvature friction losses.
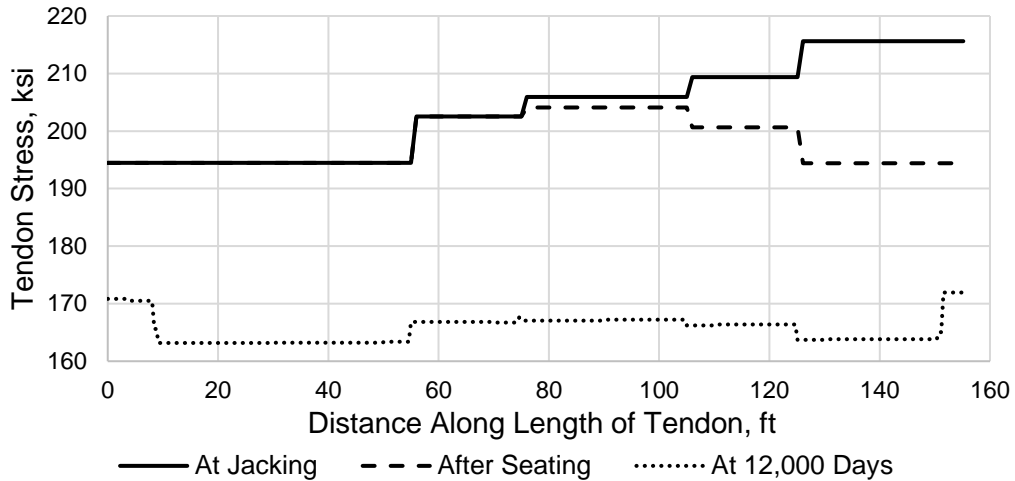
Figure 19. Tendon T9 Left in Span 6 Stress Profile

As mentioned earlier, seating losses result from slippage that occurs when the strand is released from the stressing jack. In the case of the VEB, this slippage is given in as-built documents as 3/8 in (F&M Engineers 1993). The amount of curvature friction influences how far seating losses extend along the length of the tendon. The dashed line in Figure 19 shows the loss in stress due to seating.

Long-Term Prestress Losses

Long-term prestress losses were accounted for in the FE model through the time-step analysis conducted as part of the time-dependent construction stage analysis. This time-step analysis was conducted using code expressions for creep and shrinkage from the AASHTO (2017), CEB-FIP '78, CEB-FIP '90, and CEB-FIP 2010 model codes. Creep losses depend on the change in creep strain over each time step. Change in creep strains vary through the depth of the section depending on the distribution of stress, but prestress losses due to creep are calculated from the average change in creep strain over the depth of the cross-section. Shrinkage losses are computed similarly to creep losses. Shrinkage strains are uniform through the depth of the section, and prestress losses are calculated from this change in shrinkage strain. An example of the effective prestress after long-term prestress losses can be seen by the dotted line in Figure 19.

Model Validation

The FE model was validated, by investigating its capability to reproduce deflections and strains obtained during live-load testing on the Varina-Enon Bridge (VEB), conducted in August of 2012 (Maguire, 2013). During these tests, two load trucks crossed the approach unit at highway speeds in three different load configurations. The first load configuration consisted of one truck driving in the center lane, the second consisted of the same truck driving in the left lane, and the third consisted of two load trucks side-by-side. Vertical deflections were measured at the mid-span of Span 5 by a deflectometer mounted on the bottom flange of the section and were compared to the calculated deflections. Strains predicted by the model were compared to measured strains through the depth of the girder at one location, as well.

21

Back Calculate the Effective Prestress from Measured Data

   A method, based on the crack re-opening method described in the literature, was developed to use data collected from the field to calculate the effective prestress in Spans 5, 6, 9, and 11. The starting point of the method is Equation 8, which is used to calculate the stress at any location through the depth of the girder, due to prestress, moments from self-weight and externally applied loads, and thermal stresses. To use the equation to back-calculate prestress forces, the assumption is made that, at the instant of a joint opening, the total stress at the bottom of the box where the joint opens is zero. Equation 8 includes the stresses at the bottom of the beam due to thermal effects. This has not been considered in previous investigations because most were performed in laboratory conditions where thermal effects were negligible.

$$\sigma = -\left(\frac{P_e}{A}\right) - \left(\frac{P_e e y}{I}\right) + \left(\frac{M y}{I}\right) + \sigma_{temp} \qquad \text{Eqn. 8}$$

where:

P_e = effective prestress force
A = cross-section area
e = tendon eccentricity from centroid of section
y = distance from centroid of section to location stress is calculated
I = moment of inertia of section
M = moments due to self-weight, live load, secondary prestress, creep, and shrinkage
σ_{temp} = stresses arising from thermal gradients

   The other complicating factor with the Varina-Enon Bridge is that each of the instrumented approach units is continuous for six spans. The thermal self-equilibrating and continuity stresses needed to be included in the calculation, as well as the secondary prestress moments. In addition, with time and creep, moments from permanent loads redistribute compared to the distribution immediately following completion of construction. In addition, due to the stiffness of the supports, longitudinal forces develop and then change over time. LARSA 4D computes these redistributions and presents them separately in the analytical results. This required the formulation of Equation 9, which was developed by setting the stress in Equation 8 equal to zero, rearranging and adding terms related to secondary, creep and shrinkage moments from LARSA 4D. Equation 9 was used to calculate the effective prestress from field data (Lindley 2019).

$$P_e = \left(-\sigma_{SE} + \sigma_{con} + \frac{\left(M_{sw} + M_{live} + M_{other}\right) y}{I_{cr}} + \frac{P_{sw} + P_{other}}{A_{cr}}\right) \Bigg/ \left(\frac{1}{A_{cr}} + \frac{e_{cr} y_{cr}}{I_{cr}}\right) \qquad \text{Eqn. 9}$$

where:

σ_{SE} = self-equilibrating stress at the bottom flange due to thermal gradients
σ_{con} = continuity stress associated with thermal moments
M_{sw} = self-weight moment

22

M_{live} = live-load moment

M_{other} = moment due to secondary effects from prestressing, creep, and shrinkage

I_{cr} = transformed moment of inertia of the box girder

P_{sw} = axial force due to the self-weight of the structure and restraint of movement at bearings

P_{other} = axial force due to secondary effects from prestressing, creep, and shrinkage

A_{cr} = cracked transformed area of the box girder

e_{cr} = tendon eccentricity from the cracked centroid

y_{cr} = distance from the cracked centroid to the top of the bottom flange of the section

y = distance from the uncracked centroid to the top of the bottom flange of the section

All of the terms on the right-hand-side of Eqn. 9 were obtained from either field data, known section properties, or the staged construction analysis in the finite element model. The processes of computing these values are described in the following sections. See Lindley (2019) for sample calculations following these procedures.

Section Properties

Transformed, partially-cracked section properties were used in the calculation of effective prestress force. Mild steel was not considered in the transformed section because it does not extend through the epoxy joints. A partially-cracked section was considered because of the location of the crack-monitoring LVDTs on the top of the bottom flange. All live-load strain and crack-opening data is recorded at the point at which the bottom flange is entirely decompressed, as seen in Figure 20. The full cross-sectional properties and cracked properties are presented in Table 4. Note that the areas include the composite wearing surface but not the barrier rails.
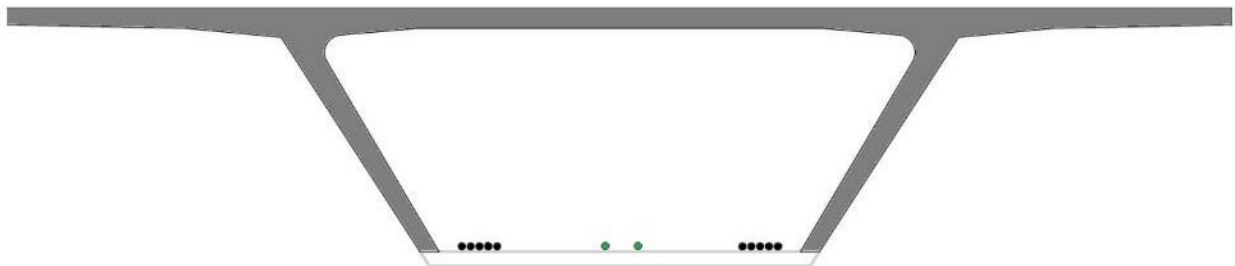
Figure 20. Cracked Section Used in the Analysis.

Table 4. Cross-sectional Properties Used for Effective Prestress Calculations

Section	Area	Location of Centroid from bottom of bottom slab	Moment of Inertia
Uncracked	14,037 in²	115 in	36,807,560 in⁴
Cracked	12,268 in²	120.7 in	16,346,893 in⁴

Self-Weight Moment

The self-weight moment was calculated through the staged construction analysis of the FE model. The self-weight of the superstructure consisted of the section of the box girder as

23

shown in Figure 9, and included deviator blocks and concrete guardrails. Deviator blocks were applied as point loads to the structure at their respective locations while the rest of the self-weight is incorporated as a distributed load totaling 15.9 klf.

Live Load Moment

An influence line analysis in the finite element model was conducted to calculate the live load moments at the locations of interest. This influence line analysis was used to correlate the live load strain measured at the trigger gage to the strains at the opening joint. Strain at the trigger gage location was measured using strain gages at that location, and that strain was used to calculate the stress, which in turn was used to calculate the moment. The influence line was then used to correlate this calculated moment at the trigger gage to find the moment at the crack location. The correlation between these two moments was used to scale the live load moments at the sections of interest. This approach was used instead of calculating the live load moment at the opening joints directly from the strain measurements adjacent to the opening joints because the bottom flange could not carry any tension force after that flange decompressed during a crack-opening event, so the strain at the crack was not considered reliable to calculate an applied live load moment.

Self-Equilibrating Thermal Stresses

The basic approach for determining thermal stresses was presented previously. Equations 6 and 7 can be used to determine the restraint force and moment, if the temperature distribution and width of the member can be described with continuous functions. For this project, it was required to develop a method to calculate the thermal stresses based on the locations of the thermocouples and the temperature measured by each thermocouple at the time of a crack opening event. Calculating SE stresses at any location through the depth of the member begins by artificially restraining the unit at the extreme ends. Equation 10 can be used to determine the stress in the cross-section at the location of each thermocouple.

$$\sigma_{TR,i} = E\alpha\Delta T_i \qquad \text{Eqn. 10}$$

where:
  $\sigma_{TR,i}$ = Thermal stress in artificially restrained condition at thermocouple i
  E = Modulus of elasticity
  α = Coefficient of thermal expansion
  ΔT_i = Difference in temperature between TC_{cool} and TC_i,
  TC_{cool} = Temperature at the coolest location in the cross-section
  $TC_{i,}$ = Temperature at thermocouple i

Next, the restraining axial force and moment are calculated using Equations 11 and 12. These equations are summations of the temperatures for each of the 18 thermocouples and their associated tributary areas, as presented in Table 2.

$$P = E \cdot \alpha \cdot \sum_{i=1}^{18} \Delta T_i A_i \qquad \text{Eqn. 11}$$

24

$$M = E \cdot \alpha \cdot \sum_{i=1}^{18} \Delta T_i A_i Y_i \qquad\qquad \text{Eqn. 12}$$

where:

ΔT_i = Difference in temperature between TC_i, and TC_{cool}
A_i = Tributary Area of thermocouple i, as presented in Table 2.
Y_i = Distance of thermocouple i from the center-of-gravity of the section.

The final SE stress at any section is calculated by adding the stresses due to the released restraint axial force and bending moment, to the stress due to the thermal gradient in the artificially restrained structure. This calculation can be seen in Equation 13.

$$\sigma_{SE} = \sigma_{TR,i} + \frac{P}{A} + \frac{My}{I} \qquad\qquad \text{Eqn. 13}$$

Thermal Continuity Forces

As presented earlier, thermal continuity forces arise from the application of a thermal gradient to a redundant structure. To calculate continuity forces at any location for a thermal gradient, the interior supports are reinstated back in the model, and the thermal moment and axial force are applied to the structure. The resulting bending moment and axial force at any section can then be found. Because a wide variety of measured thermal gradients were considered, the structure was analyzed for an applied unit moment and axial force, and the internal forces were found for bending moment and axial force respectively. These values were then used to scale Equations 11 and 12, and the continuity forces at each section were calculated.

Secondary Prestress, Creep, and Shrinkage Effects

Prestressing, creep, and shrinkage are all applied deformations to the structure. These deformations in a redundant, continuous approach unit result in secondary prestress, creep, and shrinkage forces, respectively, giving rise to moments and axial forces.

Secondary prestress effects occur when the structure is stressed. In the simply supported case, the superstructure would tend to shorten and camber upward. When redundancies are present, however, these deformations are restrained by the superstructure's own self-weight, and the stiffness of the bearing supports.

Creep and shrinkage effects are caused by the restrained deformation over the life of a structure. Creep causes axial shortening and bending in both the superstructure and the substructure. The compressive nature of the creep axial force is a result of the restrained bending of the substructure. Shrinkage only causes shortening of the superstructure and substructure without any bending. The small amount of bending moment due to shrinkage results from differential shortening of the substructure.

The axial forces and moments due to these imposed deformations were tabulated in the FE model separately from other forces. These moments and forces were calculated at each section of interest. Since forces arising from creep and shrinkage, as well as the changes in

25

prestress primary and secondary moments, are dependent on the selected creep and shrinkage functions, an iterative process was conducted to determine the creep and shrinkage parameters that best matched the back-calculated effective prestress.

Compare Field Determined Effective Prestress to Other Models

The validated LARSA 4D model was used to compare the effective prestress determined from the field data to the effective prestress predicted using available creep and shrinkage models. LARSA 4D has several models that can be used, including CEB-FIP '78, CEB-FIP '90, CEB-FIP 2010 and AASHTO (2017). The bridge model was run with each creep and shrinkage model to determine the effective prestress for each.

Estimate Future Losses and the Effect on Flexural Strength

To assist in the planning for the future maintenance of the Varina-Enon Bridge, the available creep and shrinkage models in LARSA 4D were used to estimate future prestress losses. With the resulting effective prestress, calculations of flexural strength were performed.

The following equations (Equations 5.7.3.1.2-1 and -2 from AASHTO (2017)) were used to determine the stress in the tendons at flexural strength:

$$f_{ps} = f_{pe} + 900 \left(\frac{d_p - c}{l_e} \right) \hspace{3cm} \text{Eqn. 14}$$

$$l_e = \left(\frac{2 l_i}{2 + N_i} \right) \hspace{3cm} \text{Eqn. 15}$$

where:
  f_{ps} = stress in tendon at flexural strength, ksi
  f_{pe} = effective prestress after all losses, ksi
  d_p = distance from extreme compression fiber to the centroid of the prestressing tendons, in
  c = distance from extreme compression fiber to neutral axis, in
  l_e = effective tendon length, in
  l_i = length of tendon between anchorages, in
  N_i = number of support hinges crossed by the tendon between anchorages

Equation 14 assumes a certain elongation occurs at every inelastic hinge that develops when a span experiences a complete collapse mechanism. Each span requires a mid-span hinge, and then a number of support hinges, depending on whether the span is an end span in a continuous unit or an interior span. For a continuous tendon in an end span failure mechanism, the tendon crosses one support hinge in addition to the mid-span hinge. For a continuous tendon in an interior span failure mechanism, the tendon crosses two support hinges, in addition to the mid-span hinge. However, the tendons of the Varina-Enon Bridge are not continuous. Therefore, it is possible that a tendon only crosses the mid-span hinge, and not a support hinge (See Figure 21). This would be the case if the support hinge occurs adjacent to the pier segment in the adjacent span. MacGregor (1989) observed this type of mechanism in a laboratory test of

a scaled model of a segmental bridge with external tendons. So, for conservatism, strength calculations were performed assuming the tendons cross no support hinges.
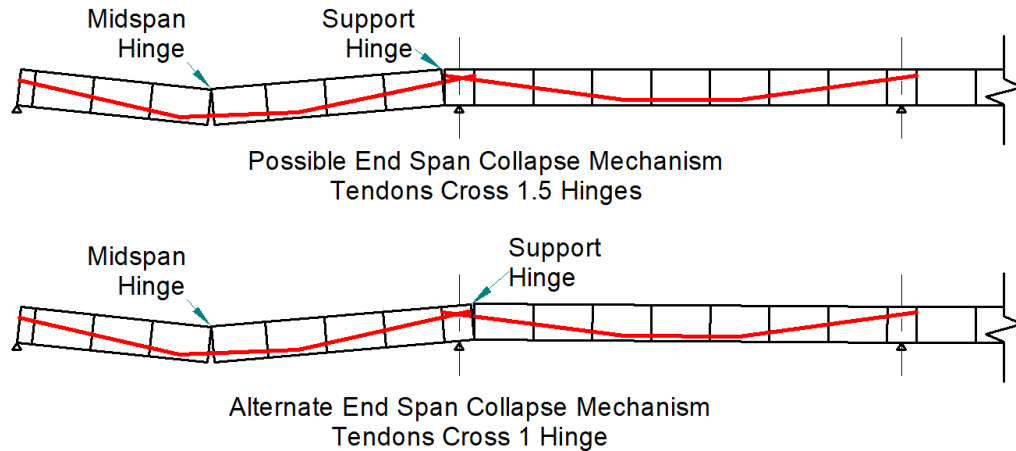
Figure 21. Possible Failure Mechanisms for an End Span in a Multi-Span Unit

Compare Design Thermal Gradients to Measured

The temperatures measured by the thermocouples were recorded every two minutes every day. The data was analyzed to determine the maximum thermal differential between the average web temperature and the hottest top slab temperature. The uppermost thermocouple in the bridge was located 2.5 in below the top of the slab. A fifth order parabola, with the zero point located at 47 in (1.2 m as recommended by Priestley (1978)) below the top surface of the girder was used to extrapolate the top thermocouple reading to the top of girder temperature. The fifth order parabola is illustrated in Figure 22. The maximum differential on each day was determined and the largest differential during the monitoring period was also determined.
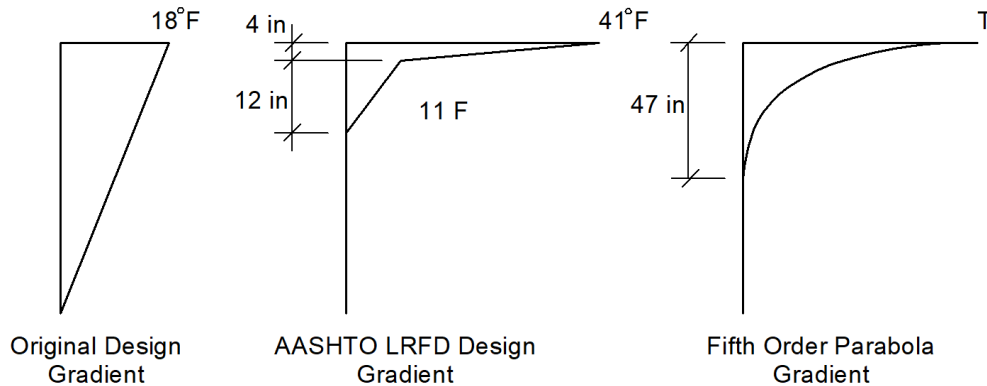
Figure 22. Design Thermal Gradients and Fifth Order Parabola Gradient

The temperature distribution through the depth of the girder, as measured by the thermocouples, was compared to two design gradients: the original design gradient, which was a linear 18°F difference between the top and bottom of the girder, and the AASHTO LRFD (2017) non-linear design thermal gradient for the Richmond area. Each gradient was used to determine the restraint force and moment and these values were compared. These gradients are presented in Figure 22.

27

RESULTS AND DISCUSSION

Literature Review

Measuring Effective Prestress Force

Effective prestress force is defined as the remaining prestress force at some specific time of interest in the life of a structure. Measuring effective prestress force is an integral part of assessing a bridge's residual flexural strength. Many methods of measuring effective prestress have been studied throughout the years. The two most well-established methods of measuring effective prestress force in the literature are the use of embedded vibrating wire gages (VWGs) and the use of crack re-opening load tests.

Embedded Vibrating Wire Gage Measurement

The measurement of effective prestress by the use of embedded VWGs involves tracking the stresses in the prestressing strands from the time of initial stressing via VWGs adhered directly to, or adjacent to, the prestressing strands. These gages are cast into the members, and track the changes in strain over time. This method requires the involvement of researchers from the time of casting and has been historically used to validate prestress loss estimation formulas. Since most structures are not cast with embedded VWGs, this is not a viable method of measuring effective prestress force for the majority of bridges.

Method Utilizing Crack Re-opening

Another well-established method for measuring effective prestress is by means of loading and re-loading the beam to the point of cracking and re-cracking. The load and the geometry of the beam at the instant of crack re-opening are then used to calculate effective prestressing force by assuming zero stress at the extreme tension fiber. Prestress loss can easily be calculated from the effective prestress force if initial jacking force is known.

The configuration for the crack re-opening test method, as conducted by Pessiki et al. (1996), can be seen in Figure 23. The test procedure consisted of loading a simply-supported beam in three-point bending. First, the beam was loaded to the point of the first occurrence of flexural cracking as identified by visual inspection. After the cracks were located and marked, the beam was unloaded. The beam was then instrumented with electric-resistance strain gages adjacent to the cracks, LVDT spanning the cracks, or a combination of both. The beams were then repeatedly loaded to the point of crack re-opening, as measured by strain gages, LVDTs, and visual inspection. Though some variation exists in the literature, this set-up represents the general procedure of tests employing this method.

The applied load measured at the occurrence of crack re-opening is used in Equation 16. At the instant of crack re-opening, the stress in the extreme tension fiber is zero. This fact is used to simplify and rearrange Equation 16, to solve for the prestress force at mid-span of the beam, as seen in Equation 17.
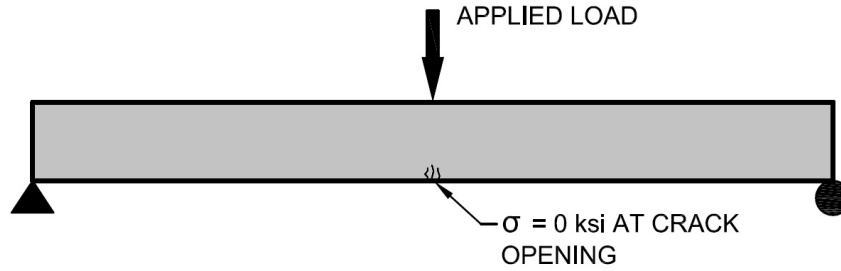
Figure 23. Testing Configuration Employed by Pessiki et al. (1996)

$$\sigma = -\frac{P_e}{A} - \frac{P_e e y}{I} + \frac{M_{sw} y}{I} + \frac{M_{applied} y}{I}$$

Eqn. 16

$$P_e = \frac{(M_{sw} + M_{applied}) y}{I} \Bigg/ \left(\frac{1}{A} + \frac{ey}{I}\right)$$

Eqn. 17

where:

P_e = the effective prestress force
A = the cross-sectional area
e = the prestressing eccentricity
y = the distance from the neutral axis to the depth in question
I = the beam moment of inertia
M_{sw} = the moment due to self-weight
$M_{applied}$ = the moment due to the applied load

Research Employing Crack Re-Opening Tests

A number of studies that utilized Equation 17 have been conducted as summarized by ACI Committee 423 (ACI 423, 2016). This summary includes studies that employed a variety of measurement methods, beam ages, and span lengths. Table 5 summarizes the relevant research conducted using methods similar to Pessiki et al. The majority of the tests summarized in Table 5 were conducted on pretensioned I-girders and box girders. All of the tests were conducted in simple span configurations in lab settings. To-date, no studies have employed crack re-opening tests on continuous-span structures or on in-service bridge girders.

Review of Creep and Shrinkage Models

For the purposes of this project, the research reviewed and compared CEB-FIP '78, CEB-FIP '90, CEB-FIP 2010 and AASHTO creep and shrinkage models. CEB-FIP '78 was the model

Table 5. Summary of Research Employing Crack Re-Opening Tests

Researchers	Number of beams tested	Age of beams, years	Length of beams, ft
Shenoy and Frantz 1991	2	27	54
Tabatabai and Dickson 1993	1	34	43
Pessiki et al. 1996	2	28	89
Halsey and Miller 1996	2	40	29
Azizinamini et al. 1996	1	25	55
Labia et al. 1997	2	20	70
Greuel et al. 2000	1	0.5	115.5
Kukay et al. 2010	8	40	34.5
Attanayake and Aktan 2011	1	49	48
Osborn et al. 2012	7	42	24
Garber et al. 2015	30	3	45.5

code used for the design of the VEB, while the remaining three represent the most widely used models in current use.

The Comité Euro-International du Béton published CEB-FIP '78 model code in 1978. This model was widely used in the United States throughout the 1980s, and the creep coefficient depends on ambient relative humidity, volume-to-surface ratio of the section, and concrete strength development. The time development of creep is defined graphically by a bounded asymptotic function which approaches an ultimate value and is defined for an age up to 10,000 days (CEB-FIP, 1978).

The CEB-FIP '90 (CEB-FIP, 1990) code is an updated version of the 1978 code expression for creep and shrinkage, which includes provisions for high-strength concretes. Again, the time-development of both creep and shrinkage are defined by a bounded function that approaches an ultimate value. The graphical depictions of these functions used in the CEB-FIP '78 model, however, were replaced with the functions themselves in the CEB-FIP '90 model. The ultimate value of the creep coefficient depends on the ambient relative humidity, volume-to-surface ratio of the section, concrete strength development, cement type, and aggregate type.

The CEB-FIP 2010 (CEB-FIP, 2013) model is an update from the CEB-FIP '90 model that reflects new information about the continuing increase of creep over time. Creep is divided into drying creep and basic creep. The time development function for basic creep is logarithmic, so this component of creep does not approach an ultimate value. The time development function for the drying creep is asymptotic. Shrinkage is also divided into basic shrinkage and drying shrinkage, each with its own time development function.

The AASHTO 2017 code expression for creep and shrinkage is based on the ACI model with modifications suggested by more recent research on the subject (AASHTO 2017). This model only takes into account ambient relative humidity, volume-to-surface ratio of the section,

and concrete strength. Like other previous models, the time-development of creep and shrinkage are defined by asymptotic functions.

Comparison of Creep Compliance Functions

In order to convey the relative behavior of the creep described in these models, the compliance function of each has been graphed in Figure 24. These compliance functions have been computed for the typical section of the VEB that is pictured in Figure 9.
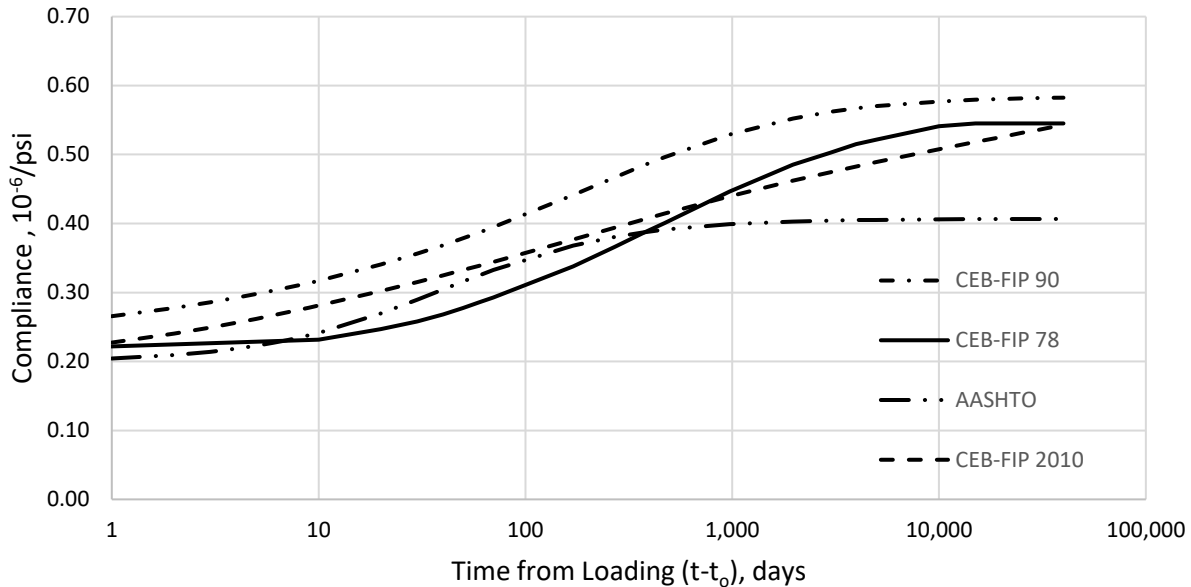

Figure 24. Comparison of Compliance Functions

Several observations can be made in Figure 24, which it should be noted, is plotted on a semi-log scale. First, the slope of the compliance functions at 40,000 days vary slightly. The CEB-FIP '78, CEB-FIP '90 and AASHTO models appear to be relatively flat, while the CEB-FIP 2010 model still has a noticeable positive slope. These differences are due to the different time-development functions that describe creep. Also, note that at 40,000 days, the magnitude of the compliance for the three CEB-FIP models are very similar, while the AASHTO model compliance is smaller.

Creep in Long-Span Structures

The CEB-FIP and AASHTO code expressions for creep and shrinkage have been utilized in a wide range of structures over the years. However, in 2008, several researchers began investigating whether these models were appropriate for use in long-span bridge structures, which are highly sensitive to creep and shrinkage. Motivated by the release of litigated data from the collapse of the Koror-Babeldaob Bridge, Bažant et al. (2010) created a finite element model of the bridge and evaluated deflections and prestress losses using the most common code expressions for creep and shrinkage. These researchers found that the current code expressions did an insufficient job of estimating long-term mid-span deflections and long-term prestress losses. Measurements taken shortly before the collapse indicated a 50% loss of prestressing force

in the Koror-Babeldaob Bridge. This greatly exceeded the design value of 22%, and the 24% loss determined from the finite element analysis utilizing the CEB-FIP '90 code expression for creep and shrinkage. Figure 25 shows the prestress loss predictions utilizing each model along with the actual measured values (Bažant et al. 2010).
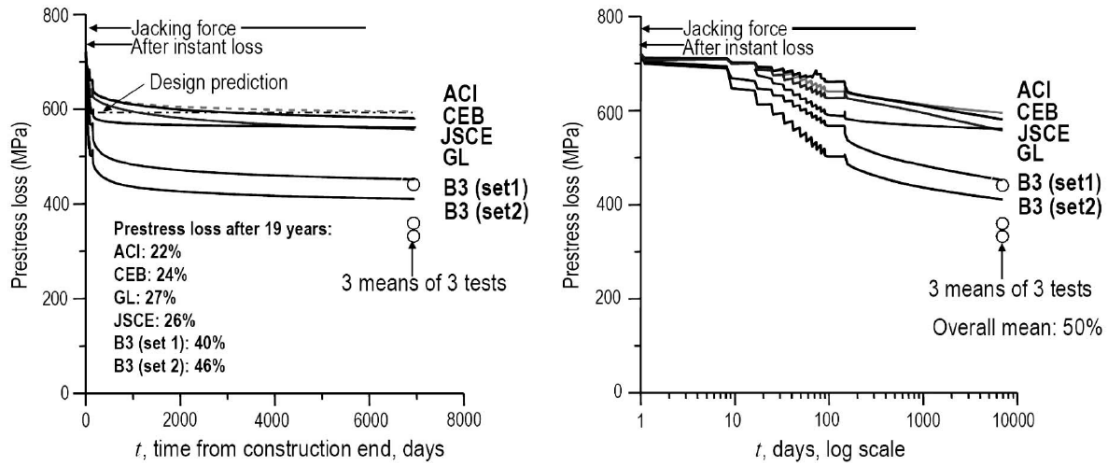
Figure 25. Prestress Loss Estimations on the Koror-Babeldaob Bridge (From Bazant et al. 2010).

Bažant et al. (2012) published data on a total of 56 large box-girder bridge spans which were experiencing excessive deflections. Most of the spans were balanced cantilevers with midspan hinges and were experiencing very similar behavior to the collapsed Koror-Babeldaob Bridge. Namely, the progression of deflections was significantly greater than those predicted by ACI and CEB models after multiple decades. Researchers concluded that these excessive deflections were far more prevalent than originally suspected and that the blame likely rests, not on poor construction, but on improper design recommendations.

Maintain and Upgrade Instrumentation Systems

The instruments and data acquisition systems were installed in the spans noted in the Methods section. Data was collected continuously, with some isolated gaps in data due to equipment malfunction, throughout the project. As explained in the *Methods* section, data was only placed in permanent storage if the trigger gage recorded a strain above the threshold set in the program.

A typical event for Span 5 and Span 6 is shown in Figure 26. Span 6 LVDT 1 and Span 6 LVDT 2 are across the crack in Span 6 and Span 5 LVDT is across the crack in Span 5. As can be seen in the graph, the crack in Span 6 opened more widely, approximately 0.003 in, than the crack in Span 5. The trigger gage recorded a strain of about 12 $\mu\varepsilon$ in this event. The Crack Gage is adjacent to the crack in Span 6. It can be seen that when the crack opens, the strain in the Crack Gage plateaus, indicating that the crack has decompressed and the joint is opening.

In some cases, events were recorded which did not represent a load passing over the crack. This may have been due to drift in the Trigger Gage, or malfunction of one of the sensors. Figure 27 shows an example of a registered event that represents drift and excessive noise in the gages.

32
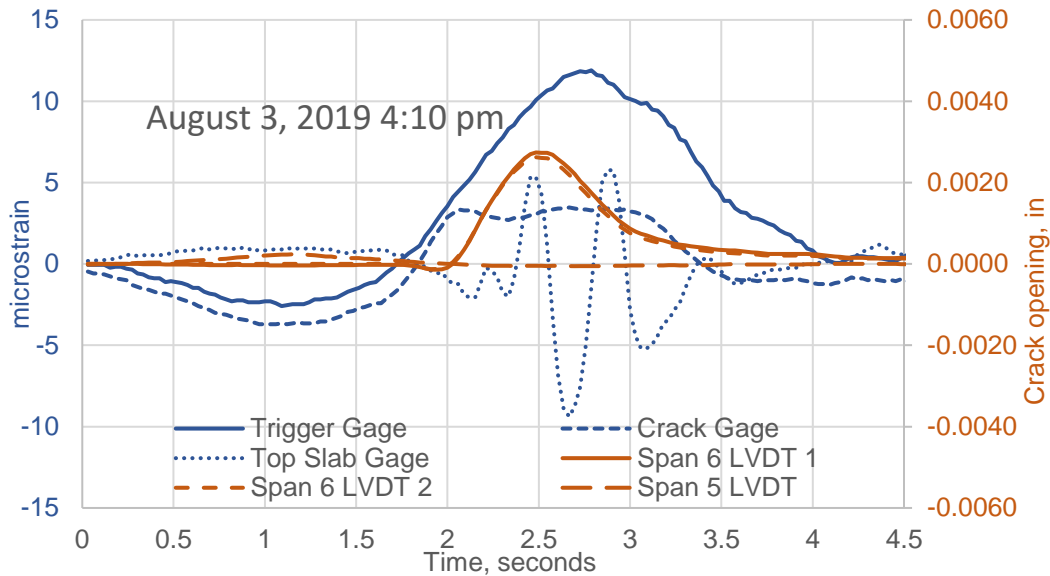
Figure 26. Typical Load Event for Spans 5 and 6. LVDT = Linear Variable Differential Transformer
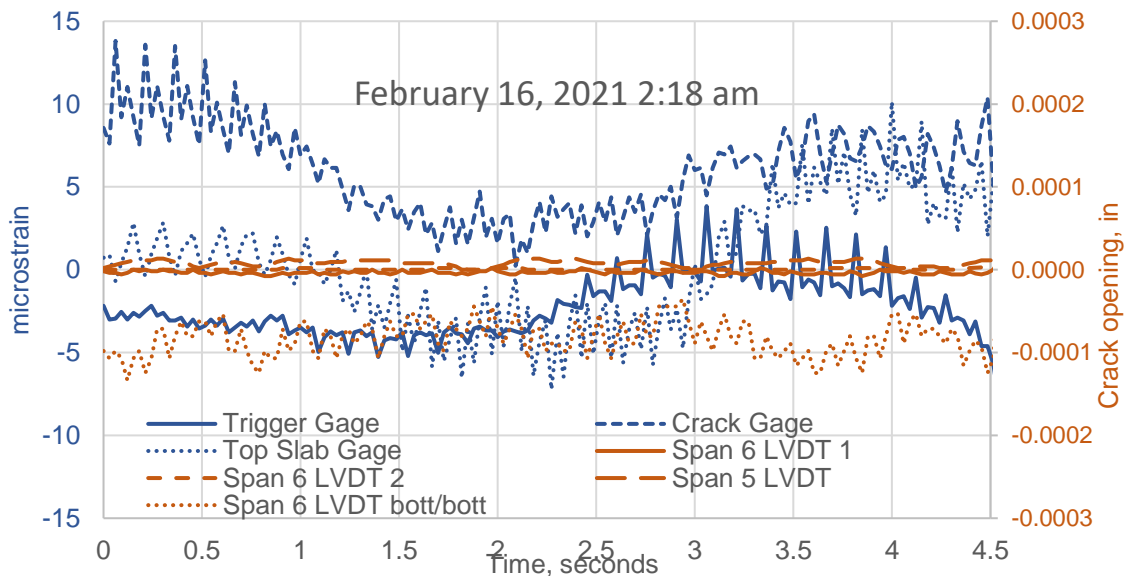
Figure 27. Example of an Event That was Filtered Out. LVDT = Linear Variable Differential Transformer

It was necessary to review the data and filter out events that did not represent a true load event. A small number of events were visually inspected, such as in Figure 26 and Figure 27. From this inspection, exclusionary criteria were calibrated and applied to all the data to filter out events that did not constitute a true load event. The strain gages were prone to drift, so a zeroing subroutine was added to the data acquisition system to ensure that the majority of captured load events were valid.

Observed Correlations in Data

Maguire et al. (2014) identified a correlation between crack openings, the magnitude of the trigger strain, and the difference between the temperature at the top of the bridge and the

33

average web temperature. The data collected in this project was investigated to determine if the trend continued, and if other correlations could be found. Figure 28 shows data from Span 6 for approximately one year (May 16, 2019 to April 4, 2020). The bubble chart shows the relationship between the trigger strain on the horizontal axis, the temperature difference on the vertical, and the crack opening, which is indicated by the size of the bubble. As can be seen in the chart, the largest crack openings typically occur with a large thermal differential. Most events which had a thermal differential less than 10°F, had crack openings less than 0.001 in. It can also be seen that very large events, in terms of the triggering strain, result in very small crack openings if the thermal differential is very small.

It had also been observed from the data that the average web temperature had an influence on the measured response of the bridge. Figure 29 shows the relationship, for the same period of time as presented in Figure 28, between average web temperature, temperature difference and crack opening size. In this chart, it is very clear that the largest crack openings consistently occur with a combination of large temperature differential and high average web temperature.
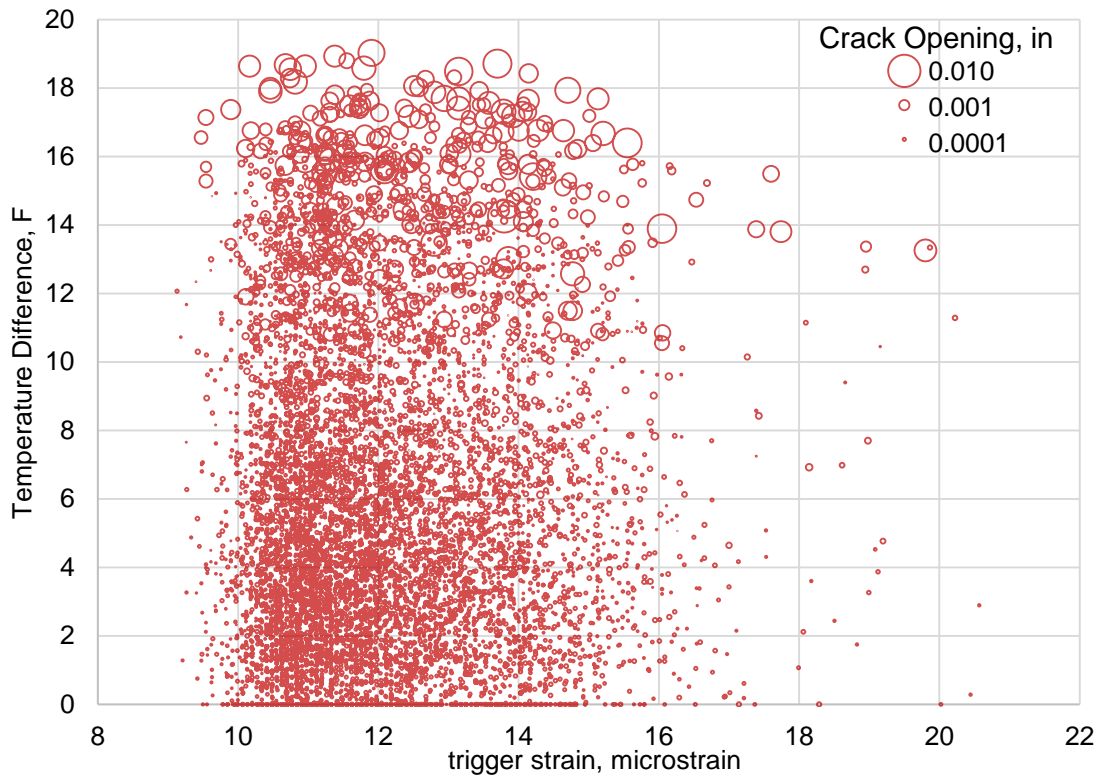
Figure 28 Correlation Between Trigger Strain, Temperature Differential and Crack Opening Size

Develop and Validate a LARSA 4D Model of the Bridge

The LARSA 4D model was developed for the first unit, Spans 1-6, and the second unit, Spans 7-12 of the northbound approaches of the Varina-Enon Bridge. As mentioned in the Methods section, the model was validated by comparing to results from a live load test performed in 2012 by Maguire et al. (2014). This section presents the comparison of test data to the FE model results.
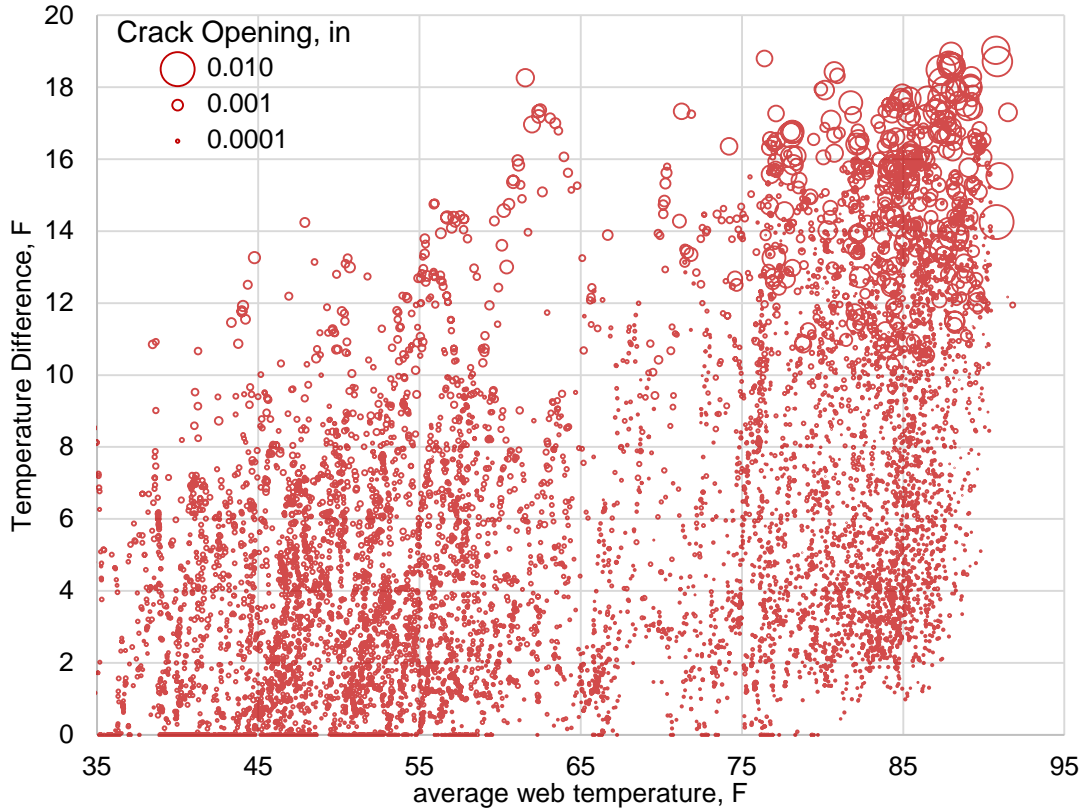
**Figure 29. Correlation Between Average Web Temperature,
Temperature Differential and Crack Opening Size**

The analytically-obtained and maximum mid-span deflections for Span 5 from the August 2012 load test are compared in Table 6. The axle loads were applied to the FE model as static loads, without any dynamic amplification factors. The FE model satisfactorily reproduced the live-load test deflection, with the normalized difference ranging from 0% for Load Configuration 2 (LC2), to 21% for Load Configuration 3 (LC3). The model is generally more flexible than the actual bridge, which could be due to an underestimated modulus of elasticity. It could also be due to the additional stiffness provided by concrete barrier rails. The rails were included as self-weight, but added no stiffness to the model. Although a 21% difference in deflection seems somewhat large, it is only a difference of 0.013 in, on a 150 ft long span. Future refinement of the model is possible, but it was deemed acceptable for the purposes of this project.

Table 6. Comparison of Vertical Deflections at Mid-Span of Span 5.

Load Configuration	Span 5, Mid-Span Deflection, in		Model Test
	Live-Load Test Results	FE Model Results	
LC1	-0.030	-0.035	1.17
LC2	-0.035	-0.035	1.00
LC3	-0.062	-0.075	1.21

35

Figure 30 compares strains measured through the depth of the cross-section at the mid-span of Span 5 during live load tests, and compares the data to the strains predicted by the LARSA 4D model. The strains are well predicted for the top two strain gages. However, the correlation for the bottom gage is not as good. This is likely due to the gage's proximity to the crack in Span 5 (Section C-C in Figure 15). However, this data further validates the LARSA 4D model.
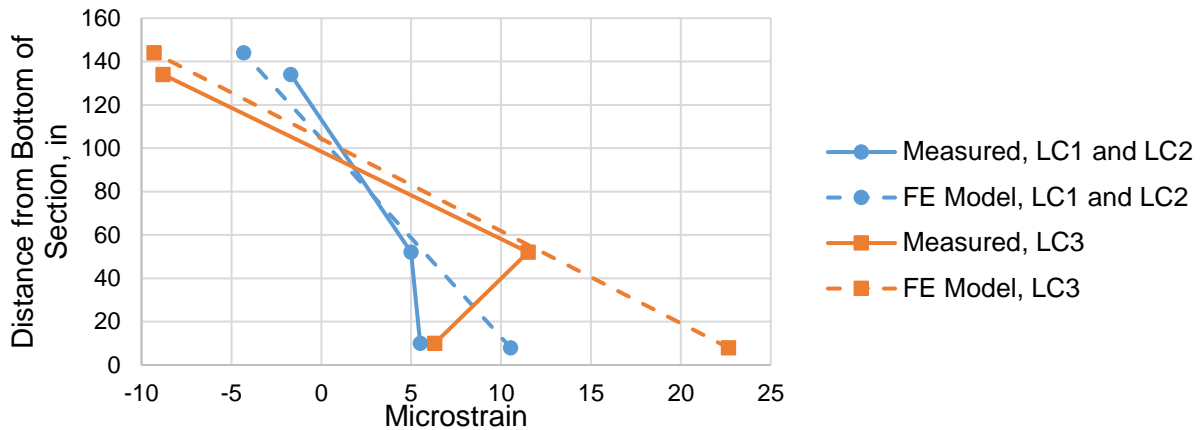
Figure 30. Strains at the Midspan of Span 5 during Live Load Tests

Back Calculate Effective Prestress from Measured Data

This section presents the results of the back-calculation of effective prestress. As described in the *Methods* section, first certain information needed to be extracted from the LARSA 4D model, then this information was used in conjunction with data collected in the field to perform the calculation. The LARSA 4D results are presented first, followed by the field data.

Self-Weight Moments

Figure 31 shows the moments in Span 5 and Span 6 due to self-weight and displays the moment calculated at Sections A-A and C-C. Dead load moments in Span 9 are shown in Figure 32, and dead load moments in Span 11 are shown in Figure 33.
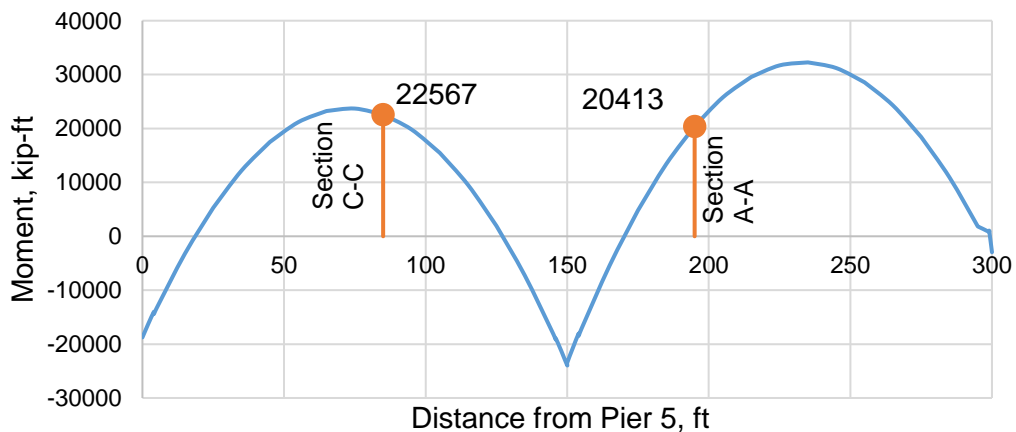
Figure 31. Dead Load Moments in Span 5 and Span 6
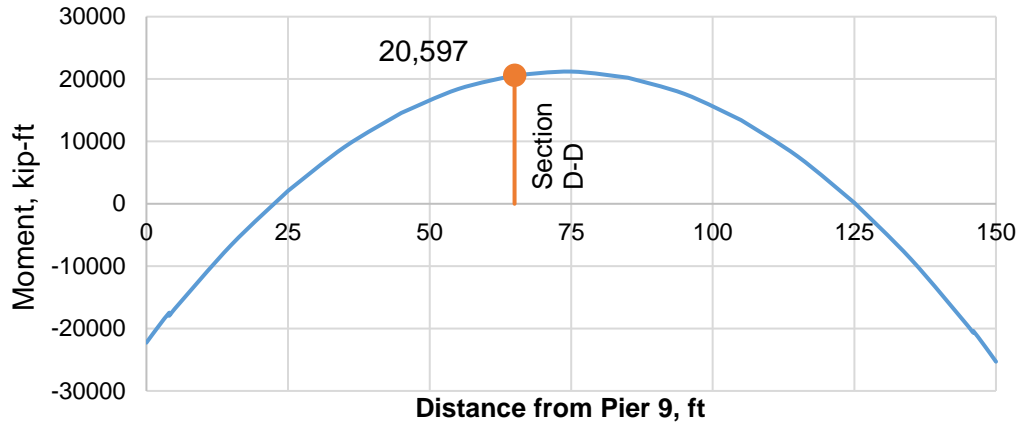
Figure 32. Dead Load Moments in Span 9
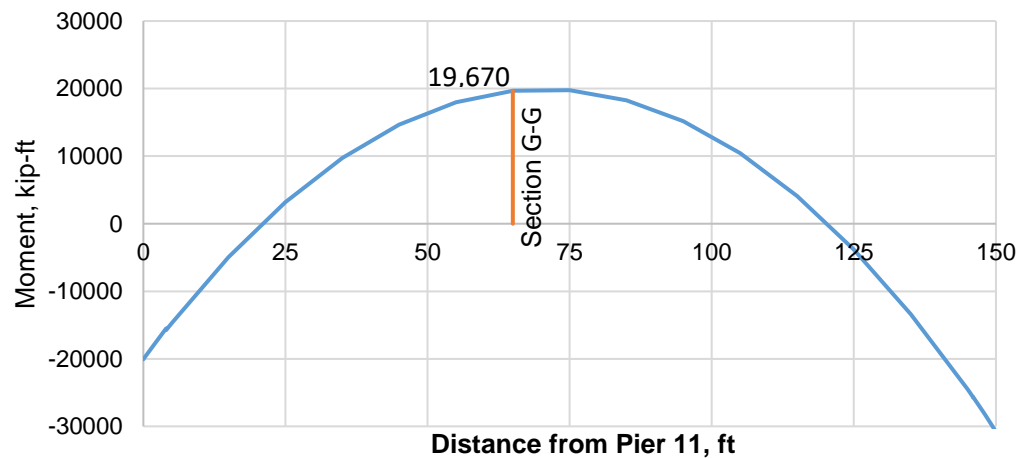
Figure 33. Dead Load Moments in Span 11

Live Load Moments

As mentioned in the Methods section, coefficients were determined from the LARSA 4D models to relate the moment at the trigger gage due to a passing vehicle to the moment at the crack location. The moment at the trigger location was calculated using the measured strain, uncracked transformed area and distance from the centroid of the cross-section to the gage on the top of the bottom slab. Then that moment was scaled with the coefficients from the influence line analysis. The coefficients indicated in Figures 34–36 were used to scale the moments determined from the trigger strain and obtain the live load moments at the sections of interest.

Thermal Continuity Forces

As described in the Methods section, the thermal continuity moment and stress was calculated for each event based on the concrete temperatures measured by the thermocouples. LARSA 4D was used to determine the continuity moment at each crack location for an applied unit moment. The moment determined for each event using Equation 12 was multiplied by the factor determined in LARSA 4D to arrive at the thermal continuity moment at the crack location. A graph illustrating the calculation of the unit bending moment is shown in Figure 37 for cracking locations in Spans 5 and 6, and in Figure 38 for Spans 9 and 11.
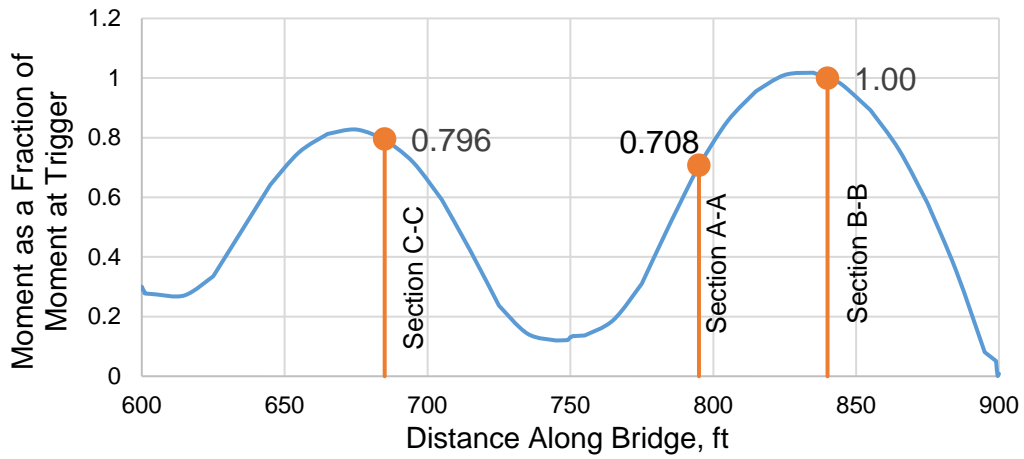
Figure 34. Envelope of Live Load Moments for Spans 5 and 6
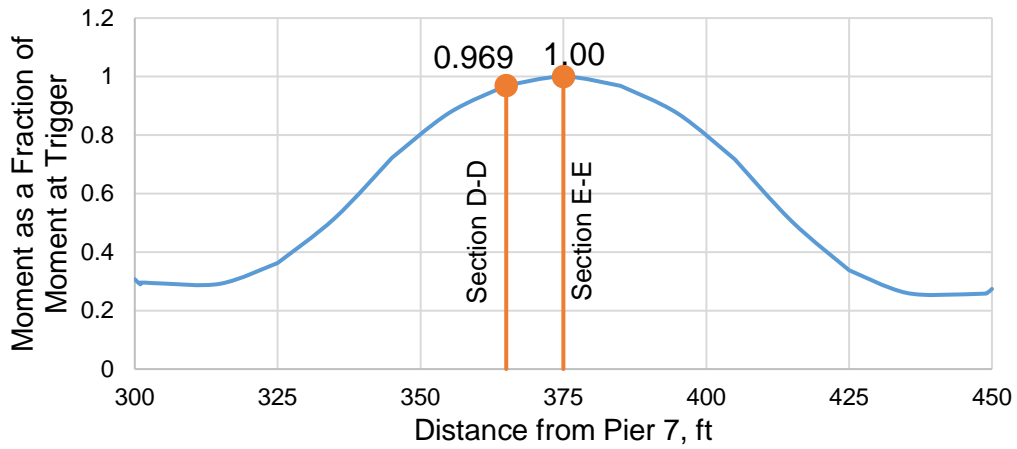
Figure 35. Envelope of Live Load Moments for Span 9
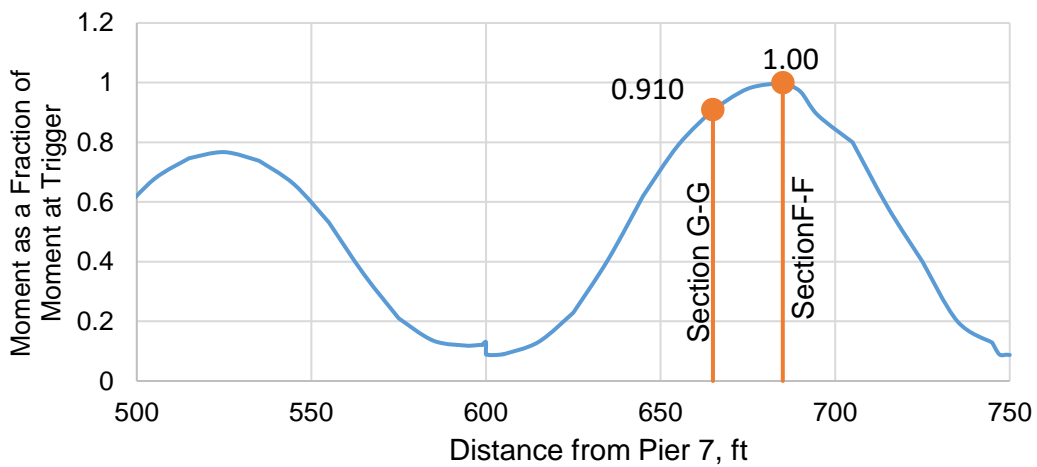
Figure 36. Envelope of Live Load Moments for Span 11
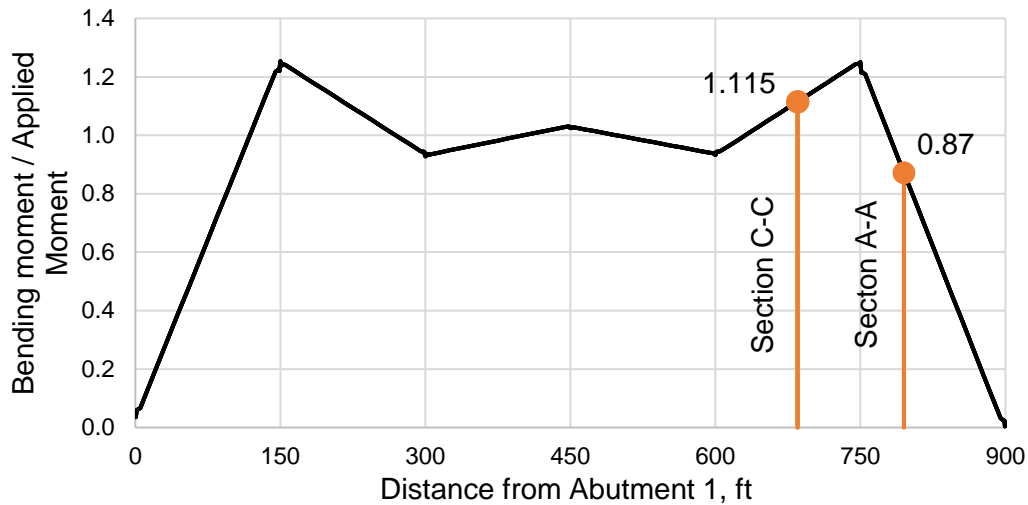
Figure 37. Thermal Continuity Moments in Spans 1-6, Due to Unit Moments
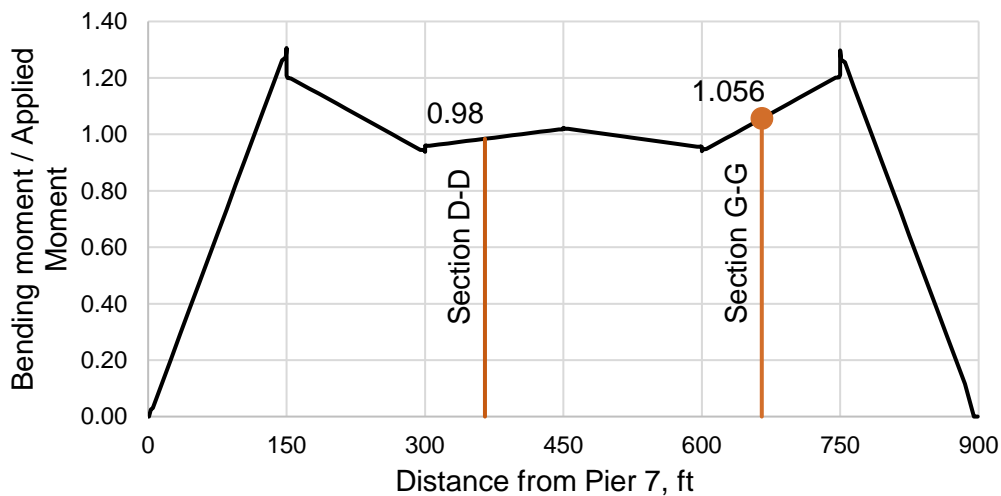
Figure 38. Thermal Continuity Moments in Spans 7-12, Due to Unit Moments

Determination of Creep Function Factor to Match Field Results

As mentioned in the Methods section, the creep, shrinkage and secondary effects calculated in the staged construction analysis were tabulated separately in the LARSA 4D results. Therefore, to use the moments in the back-calculation equation, the creep function needed to be calibrated so the LARSA effective prestress matched the data-derived effective prestress quite closely. Figure 39 presents a screen capture of the input required to use the CEB-FIP MC '90 creep and shrinkage functions in LARSA 4D. Some of the input to the model is based on the shape of the cross-section, as determined by the program. Other input is provided by the user, including the "Creep Factor" and "Shrinkage Factor". Table 7 presents how the selection of these factors influences the secondary prestress moment, and the creep and shrinkage moments. These values, in turn affect the back-calculated effective prestress. The creep and shrinkage factor of 1.85 was found to best match the LARSA 4D model effective prestress to the back-calculated value.

Figure 39. Creep and Shrinkage Input Spreadsheet from LARSA 4D

Table 7. Determination of Creep and Shrinkage Factor for LARSA 4D Model

Creep and Shrinkage Factor	Secondary Moment, k-ft	Creep Moment, k-ft	Shrinkage Moment, k-ft	LARSA 4D Effective Prestress, ksi	Back-Calculated Effective Prestress, ksi
1.0	16,920	1346	161	172.4	165.3
1.80	15,890	1940	303	165.8	165.4
1.85	15,830	1970	313	165.3	165.4
2.0	15,640	2058	341	164.1	165.3

Span 6

Results from 2013

Figures 40 and 41 show two typical events recorded for Span 6. Figure 40 presents an event on a hot day with a large thermal gradient. The maximum strain at the trigger gage was 12 με. The gage immediately adjacent to the crack indicated compression when the vehicle was in the adjacent span, Span 5, and then began to go into tension when the vehicle crossed into Span 6. However, at approximately 8 με, the strain in the crack gage plateaued and did not increase further. At the time of plateauing, the crack began to open. Then, as the vehicle crossed out of the span, the strains and crack widths reduced almost back to zero. This was a true crack opening event. Other information about this event is that the average web temperature was 91.2°F and the difference between the top slab temperature and the web temperature was 22.6°F.
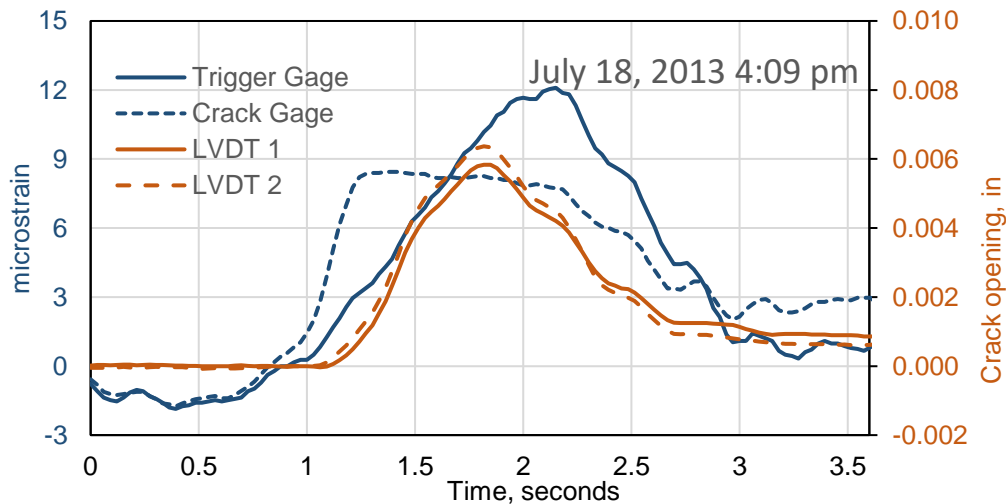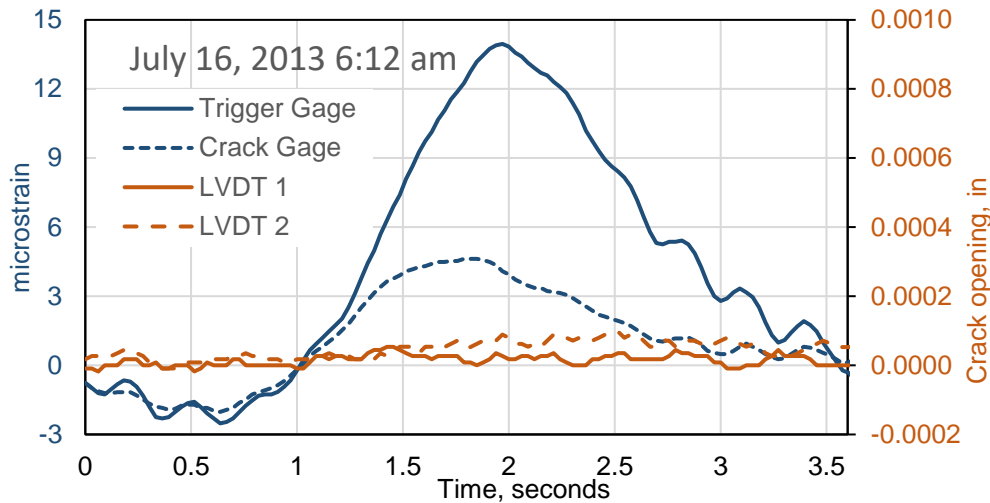

Figure 40. Span 6 Event in 2013 With Obvious Crack Opening.
**LVDT = Linear Variable Differential Transformer**

Figure 41. Span 6 Event With No Obvious Crack Opening.
**LVDT = Linear Variable Differential Transformer**

Figure 41 presents an event where it was not as clear that the crack opened during the event. In this event, the maximum trigger gage strain was even higher than in the Figure 40 event, at 14 µε, but there was no obvious plateauing of the strain measured by the gage adjacent to the crack. In addition, the LVDTs registered almost no change in the crack width, even with the large vehicle. Other information about this event is that the average web temperature was 85.5°F and the difference between the top slab temperature and the web temperature was 2.8°F. Therefore, to back-calculate the effective prestress force from the trigger events, it was necessary to determine a threshold crack width value that indicated when the crack had completely opened and the bottom slab was decompressed.

Originally, data from the long-term monitoring system was used in Eqn. 9 to calculate values of effective prestress for all triggered events. In 2013, a total of 6,697 events were recorded over a one-year period. The average effective-prestress value of these events was 153.9 ksi and the standard deviation was 6.7 ksi. The maximum crack width recorded was 0.0274 in, but the large majority of crack openings were significantly smaller than this maximum value. Effective prestress results from the 2013 data are plotted against their corresponding crack displacements in Figure 42. The distribution of prestress values can be seen in the histogram in Figure 43.

The plot in Figure 42 indicates that the scatter of prestress estimates increased as the corresponding crack widths decreased. As crack openings approached zero, the scatter in the prestress value exceeded 30 ksi. Furthermore, there appeared to be an upper bound to the prestress estimates that increased with crack width. The variation in prestress values at small crack widths is consistent with the idea that the flange may not have fully decompressed when cracks were relatively narrow. If the crack does not fully open, the basic assumption of zero stress in the derivation of Equation 9 is not valid; therefore, low prestress estimates could be expected. For this reason, events for which the crack displacements were less than 0.002 in were disregarded. This value was chosen by examining crack opening events to determine which showed the plateau behavior seen in Figure 40.

41
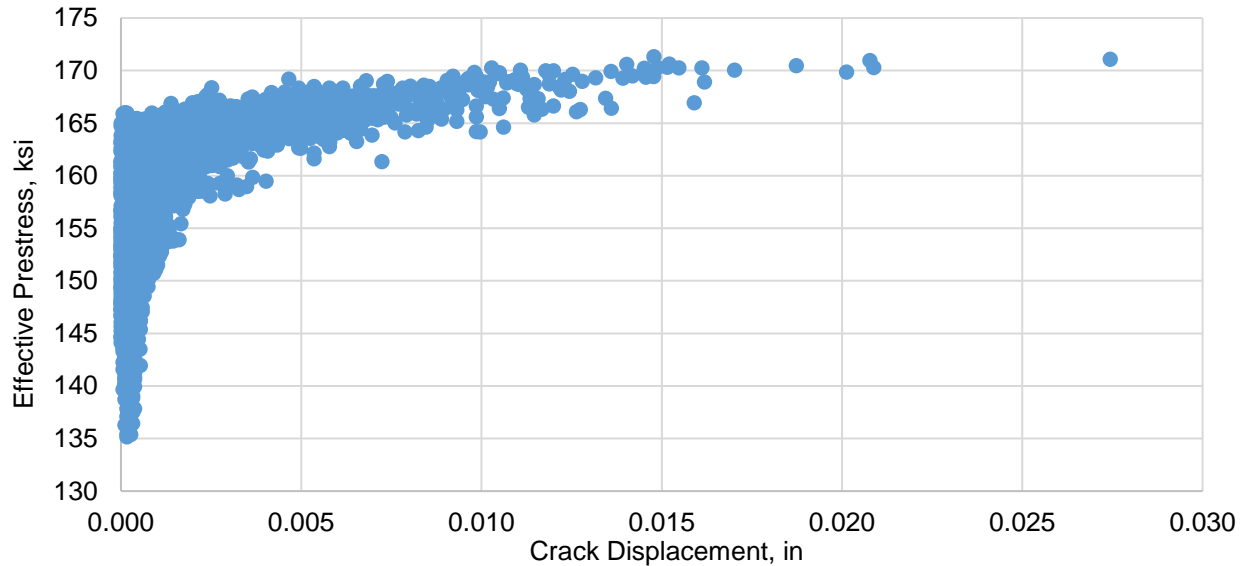
Figure 42. Effective Prestress Versus Crack Opening for Span 6 for All 2013 Events
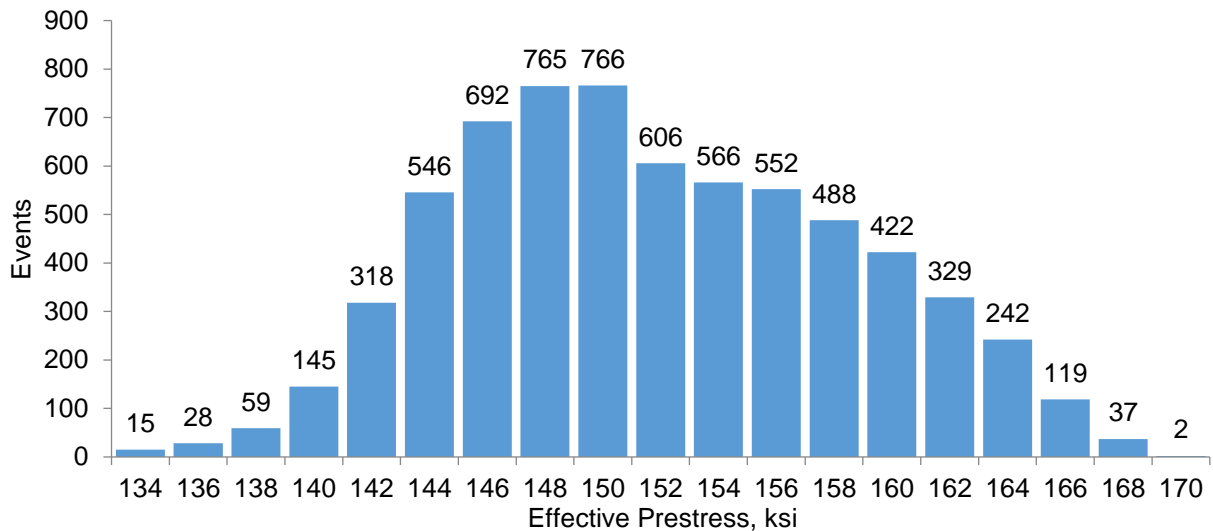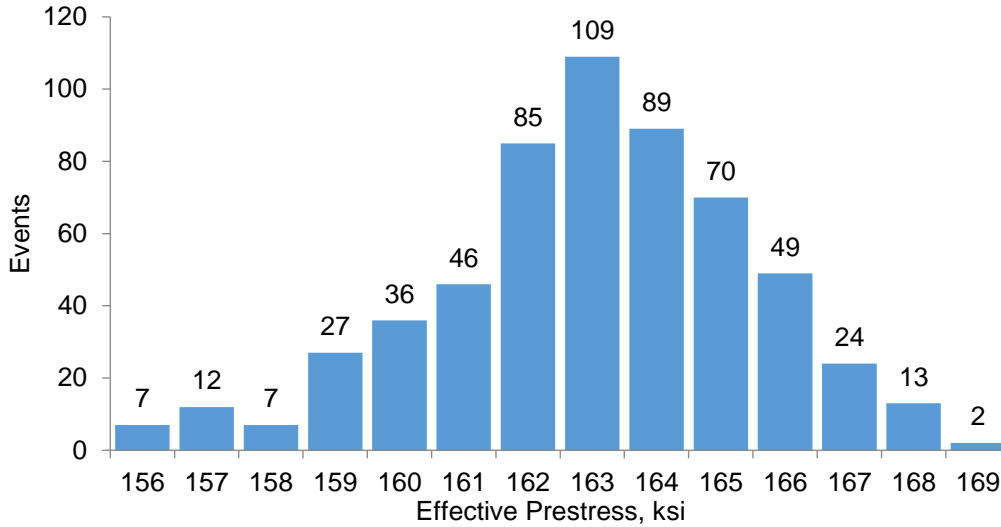

Figure 43. Histogram of Effective Prestress Values for Span 6 for All 2013 Events

Applying this 0.002-in threshold significantly reduced the size of the data set to 576 events remaining. The normal distribution of prestress estimates for this subset of events is shown in Figure 44. The mean prestress value was 166 ksi, and the standard deviation was 2.5 ksi.

Results from 2019 to 2021

As mentioned previously, the long-term monitoring system was reinstalled in Spans 5 and 6, and data has been gathered from this new system since April of 2019. The data presented herein includes measurements from the date of reinstallation up to the end of April 2021.

Figure 45 presents a plot that shows an obvious crack opening event in Span 6 from the summer of 2019. Similar to Figure 40, this figure shows that the crack opened up when the

**Figure 44. Histogram of Effective Prestress for Span 6 for 2013
Events with Corresponding Crack Openings of 0.002 in or Greater**

strain in the gage adjacent to the crack started to plateau, thus indicating decompression of the bottom slab. Recall that the new monitoring system also included an LVDT across the crack in Span 5, and a gage on the bottom of the top slab at the same location as the trigger gage. As expected, the top slab gage indicated tension when the vehicle was in Span 5, and then compression when the truck was in Span 6. However, due to local bending of the slab, the gage had a tension spike when each axle group was directly above it. The three tension spikes indicate the vehicle had a lightly loaded front axle and two more heavily loaded rear axle groups, which is typical of an 18-wheel truck. Other information about this event is that the average web temperature was 82.2°F and the difference between the top slab temperature and the web temperature was 16.5°F.
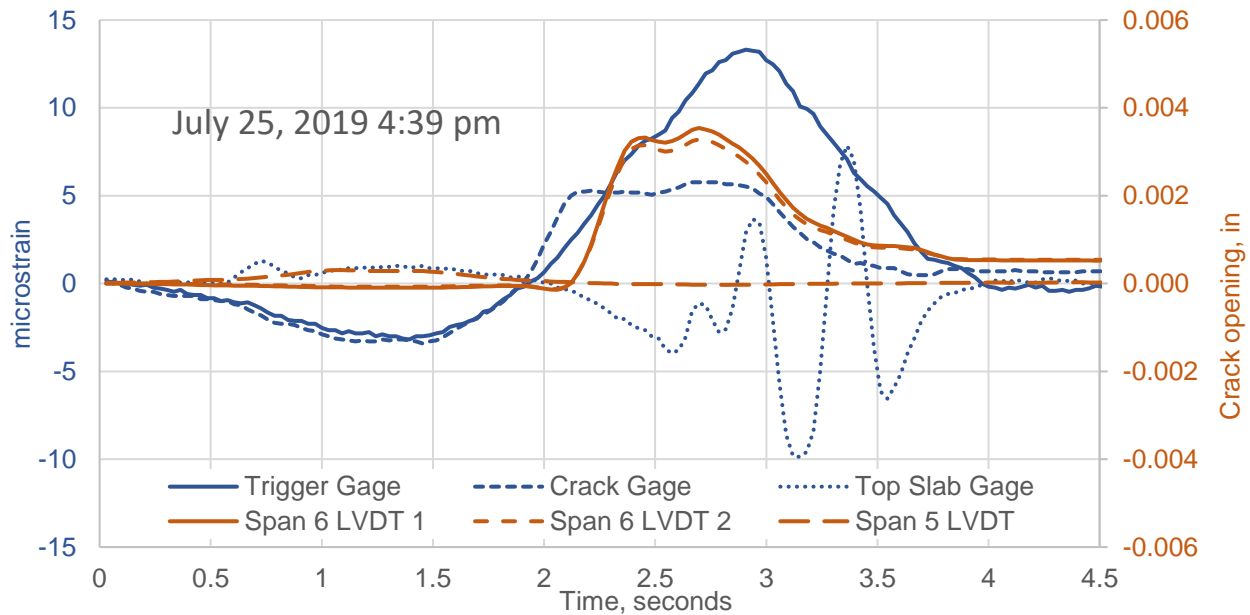
**Figure 45. Span 6 Event in 2019 With Obvious Crack Opening.
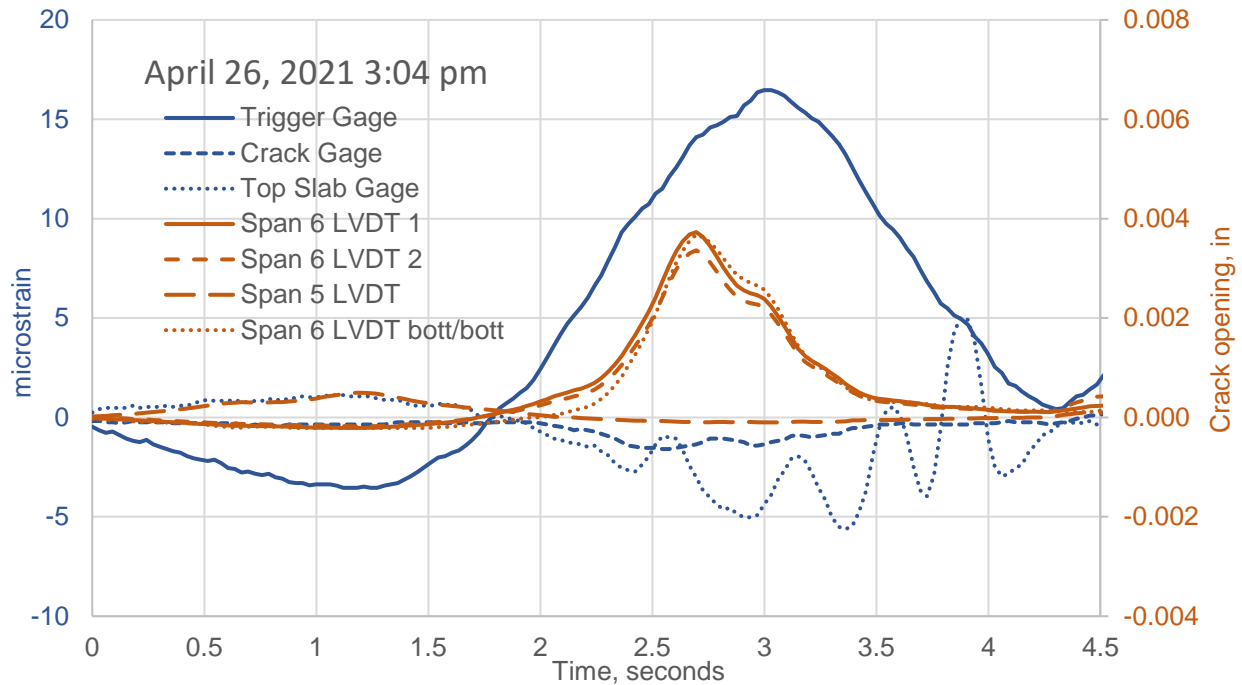LVDT = Linear Variable Differential Transformer**

43

Figure 46 presents a very similar event occurring on July 24, 2019, but in this case, there was no obvious decompression of the bottom slab. The maximum trigger gage strain, and the number and magnitudes of the peaks in the top slab gage indicate that a very similar truck caused this event as the event one day later in Figure 45. However, the crack opening magnitudes during the July 24th event were considerably smaller, with a maximum of 0.0002 inch in Span 6 and 0.00013 inch in Span 5. In addition, there was no discernable plateau in the strain measured by the gage adjacent to the crack. Additionally, the average web temperature was 78.6°F and the difference between the top slab temperature and the web temperature was 10.3°F, which were considerably cooler than the event that occurred one day later.
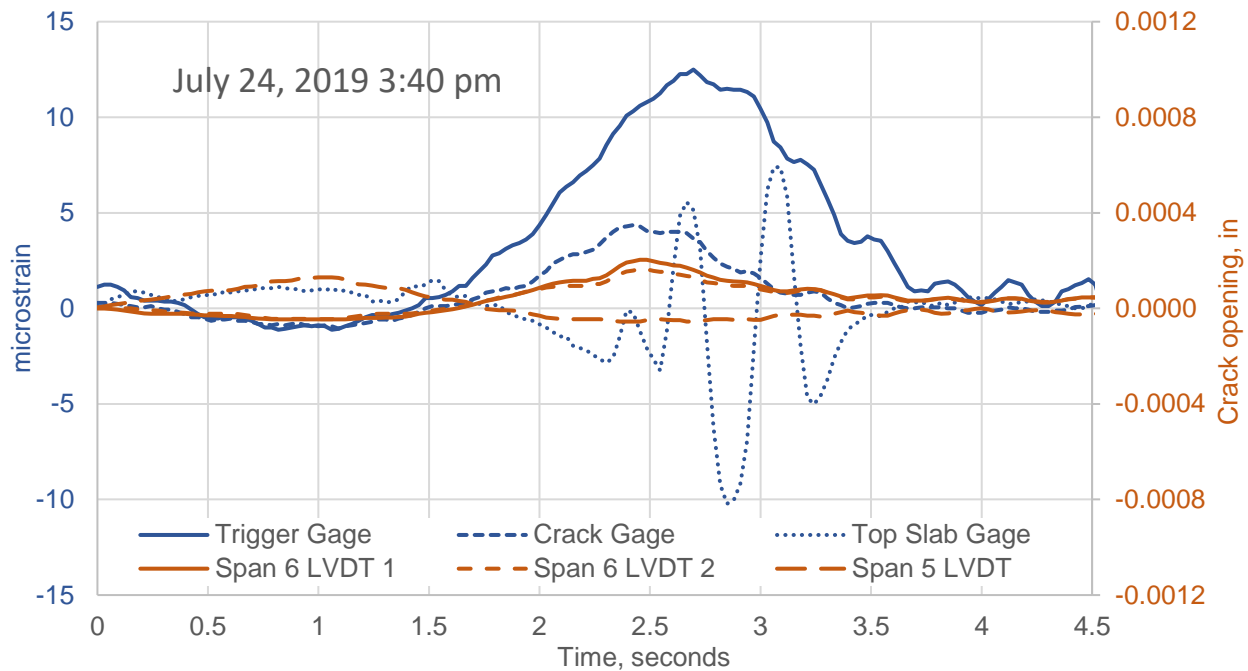

Figure 46. Span 6 Event in 2019 with No Obvious Crack Opening.
LVDT = Linear Variable Differential Transformer

Figure 47 presents a plot of an event that occurred April 26, 2021, which is interesting because the event appears to have been caused by more than one vehicle on the spans at that time, as indicated by the four tension spikes of the top flange gage. Also, the Span 6 LVDTs show an interesting pattern of a primary peak and then a smaller peak, before the crack closed. Additionally, the LVDT on the bottom of the bottom flange exhibited a response almost identical to the LVDTs on the top of the bottom flange. This observation indicates that using the LVDTs on the top of the bottom flange as indicators of bottom flange decompression was acceptable. The other odd behavior to note in this figure is that of the gage adjacent to the crack in Span 6, which showed hardly any change in strain during this rather large event. This gage was even slightly in compression when the load was in Span 6. This behavior was opposite of what had typically been seen in crack opening events, where the gage indicates tension. Other information about this event is that the average web temperature was 61.6°F and the difference between the top slab temperature and the web temperature was 15.5°F. The average web temperature has an effect on crack openings as seen in Figure 29, but the mechanics are not clear.

Figure 47. Span 6 Event in 2021 with Bottom of Bottom Flange LVDT in Place. LVDT = Linear Variable Differential Transformer. Note that "Span 6 LVDT bott/bott" is the LVDT placed on the bottom of the bottom slab

Figure 48 presents the back-calculated effective prestress of all collected events from 2019 to 2021 compared to the measured crack width opening. There was a total of 15,370 events over the two-year period, with an average effective prestress of 153 ksi and a standard deviation of 5.9 ksi. As with the 2013 data, there was considerable scatter amongst the small crack openings and significantly less scatter for crack widths greater than 0.002 in. This 0.002-in threshold reduced the size of the data set to 301 events. The distribution of prestress estimates for these 301 events is shown by the histogram in Figure 49. The data resembles a normal distribution. The mean prestress value is almost identical to the 2013 data at 166 ksi, with a standard deviation of 2.5 ksi.
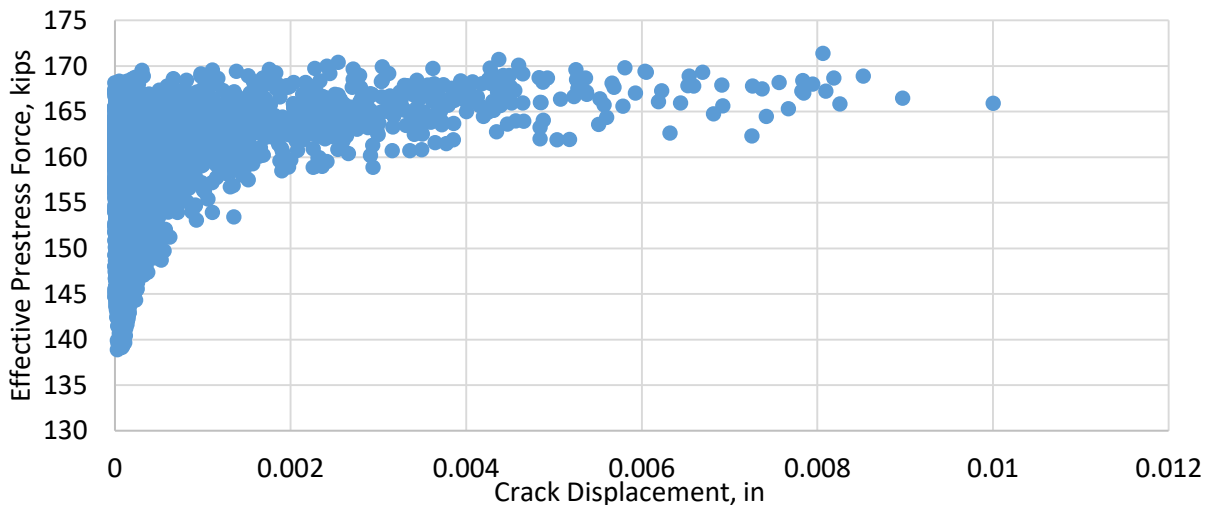

**Figure 48. Effective Prestress Versus Crack Opening for Span 6 for May 2019 to April 2021**

45
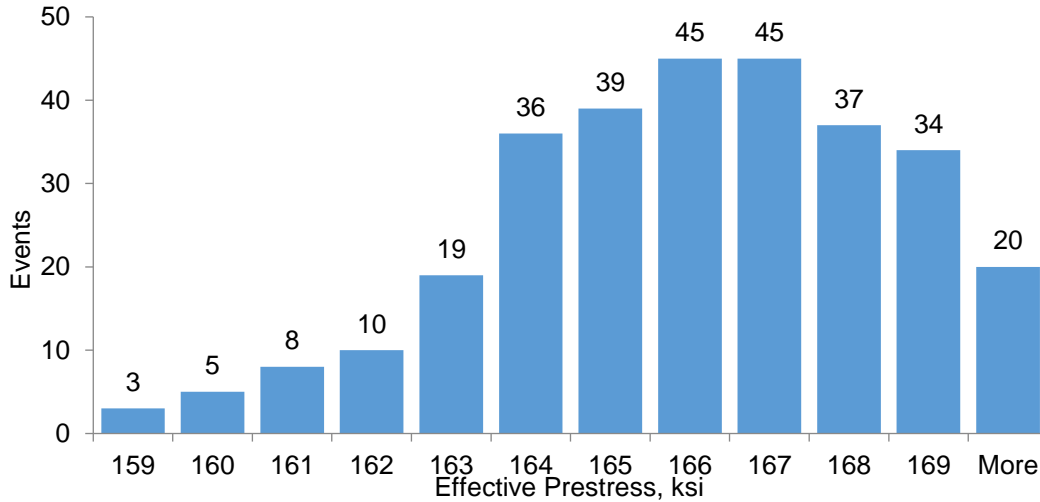
Figure 49. Histogram of Effective Prestress for Span 6 for May 2019 to April 2021 Events With Corresponding Crack Openings of 0.002 in or Greater
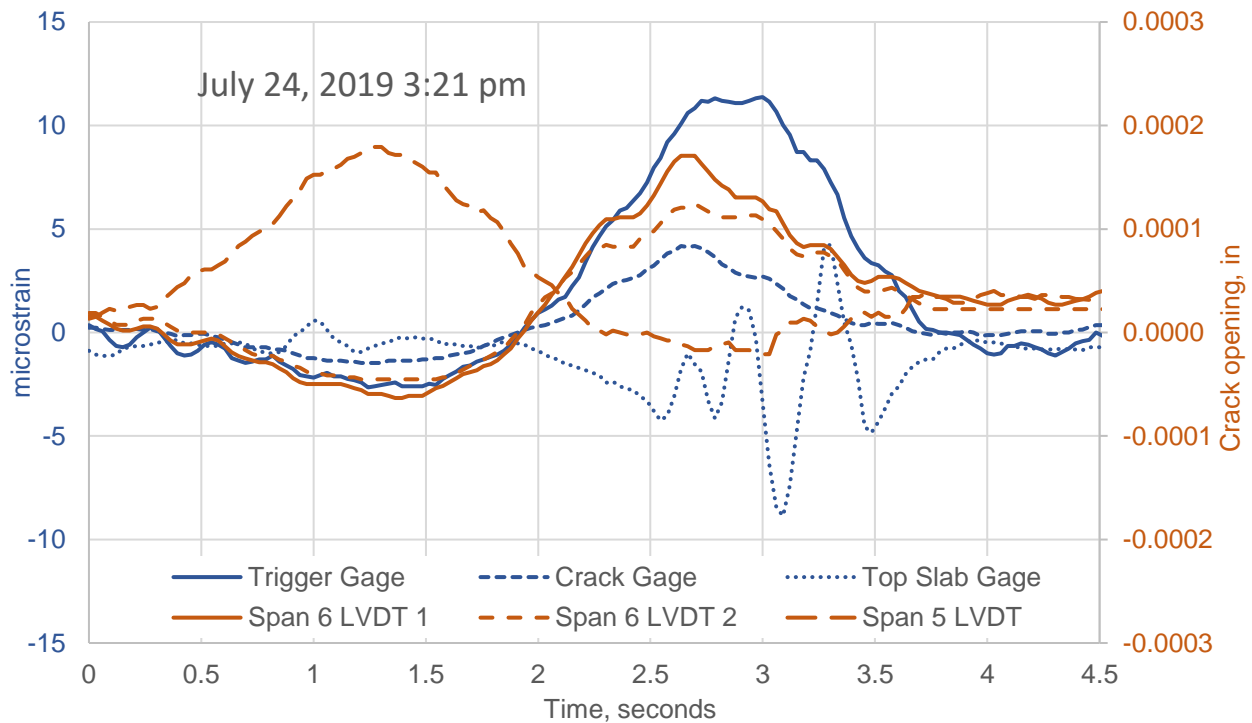
Span 5

Figures 50 and 51 show two of the larger crack opening events in Span 5. As can be seen in both plots, the crack in Span 5 never opened as widely as the crack in Span 6. During the July 3, 2019 event (Figure 50), the average web temperature was 90.8°F and the difference between the top slab and average web temperature was 14.2°F. During the July 26, 2020 event (Figure 51), the average web temperature was 90.7°F and the difference between the top slab and average web temperature was 14.0°F. For comparison, Figure 52 shows an event in which there was no obvious decompression in Span 6, and the LVDTs in the two spans show very similar readings. For this July 24th event, the average web temperature was 78.6°F and the difference between the top slab and average web temperature was 10.3°F. These subtle differences in average temperature and temperature gradient make a significant difference in the response of the structure, particularly in Span 6.
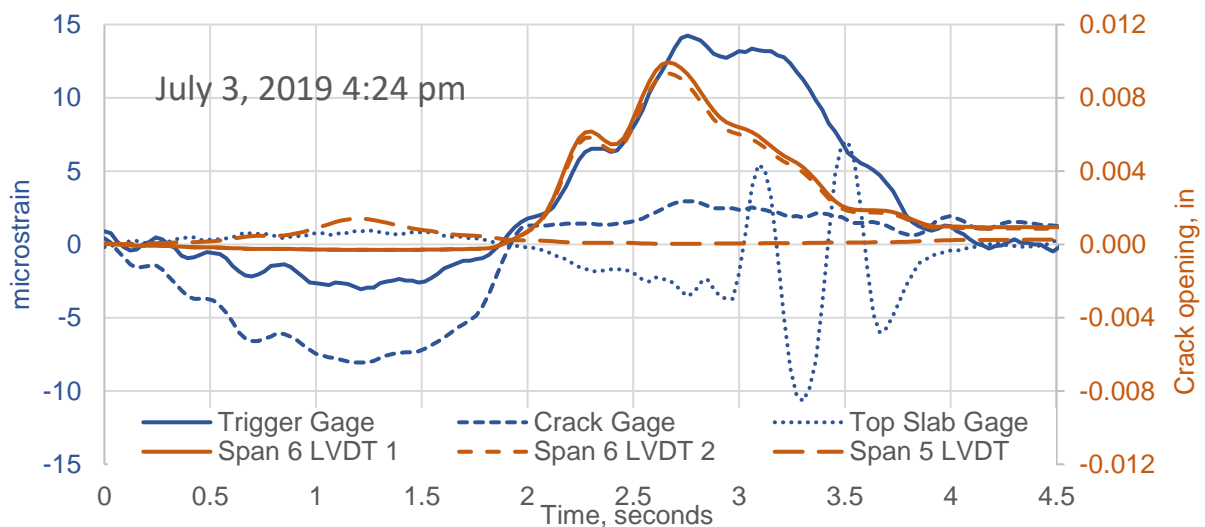
Figure 50. Span 5 and 6 Event in 2019 With Decompression in Span 6. LVDT = Linear Variable Differential Transformer

46
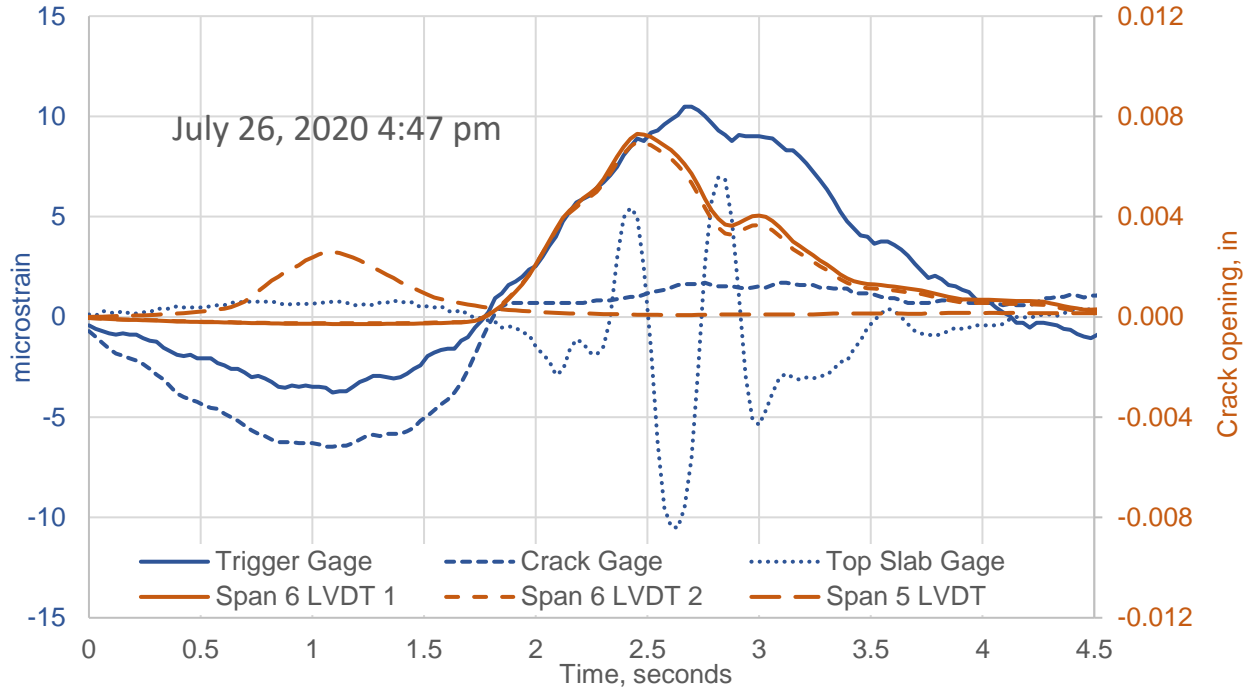
Figure 51. Span 5 and 6 Event in 2020 With Decompression in Span 6. LVDT = Linear Variable Differential Transformer

Figure 52. Span 5 and 6 Event in 2019 With No Decompression in Span 6. LVDT = Linear Variable Differential Transformer

47

Effective prestress was also back-calculated using Equation 9 for events occurring in Span 5, which had slightly larger live load, dead load, and thermal moments occurring at the crack location, compared to the crack location in Span 6, as illustrated in Figures 31, 34, and 37. The magnitudes of the crack openings in Span 5 compared to the back-calculated prestress are presented in Figure 53 for all 14,500 events. For all events, the mean effective prestress was 148 ksi with a standard deviation of 6.6 ksi. Note that the magnitudes of the crack openings in Span 5 were considerably smaller than those in Span 6. It is unclear why this is, but may be due to the restraint of longitudinal movements in the bottom slab from the bearing pads.
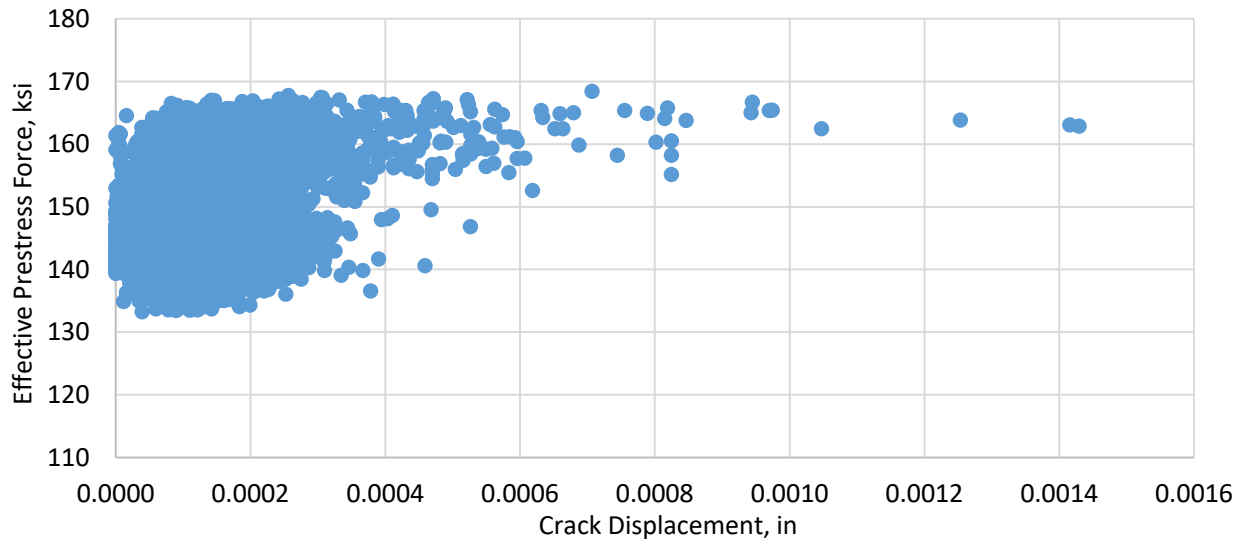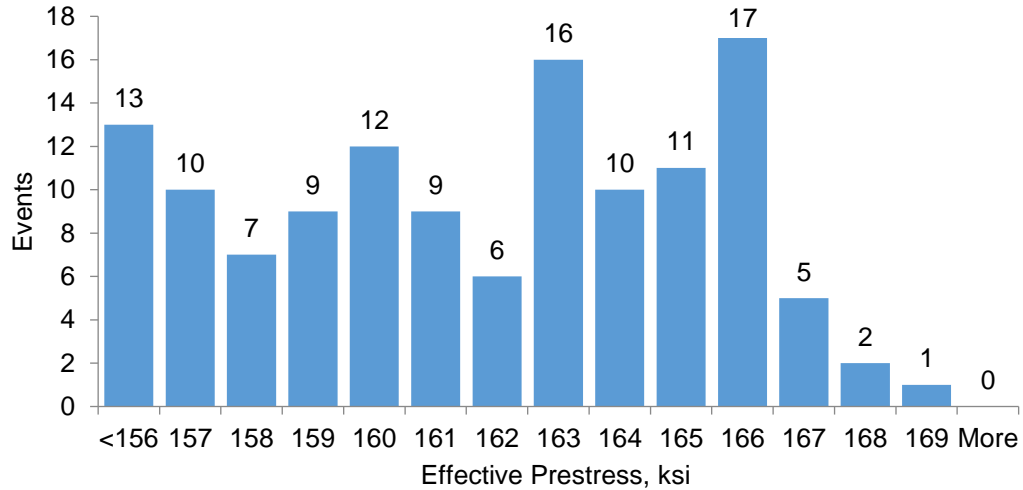

Figure 53. Effective Prestress Versus Crack Opening for Span 5 for May 2019 to April 2021

Similar to Span 6, there was considerable scatter in the effective prestress for very small crack openings in Span 5. As mentioned earlier, this result could be due to the crack not completely decompressing for the small openings. A threshold joint opening of 0.0004 in was chosen to reduce the data set and remove the small crack openings. This value was chosen because, from Figure 53, it is the value where the effective prestress values begin to converge. The remaining 128 data points were more consistent with a mean of 161 ksi and a standard deviation of 3.5 ksi. Five low outlier points were removed after closer examination of the events indicated a temporary drifting of the LVDT resulted in faulty crack opening measurements. Figure 54 presents a histogram of the remaining data points, showing the distribution was more random and less like the normal distribution of the data from Span 6.
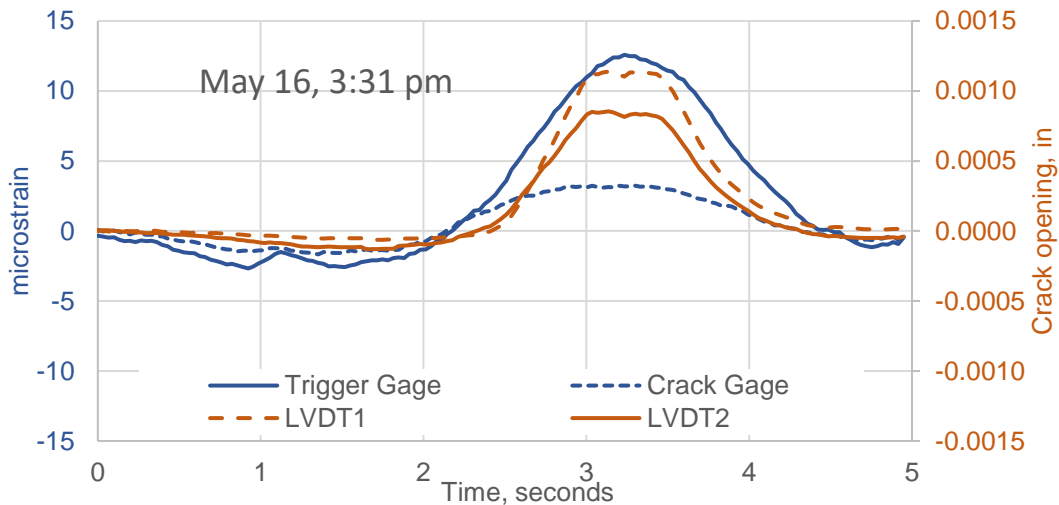
Span 9

Unfortunately, the first data acquisition system, which was installed in Span 9 in May of 2019, had a series of problems. So, that system was replaced in March of 2020. The new data acquisition system monitored the crack openings and strains in Span 9 from March 2020 to June 2020. Figure 55 presents a typical opening event in Span 9. For this event, the average web temperature was 62.9°F and the difference between the top slab and average web temperature was 12.1°F. For most events, the crack widths were quite small, compared to those in Span 6 and there was no obvious sign of decompression at the crack gage. Figure 56 presents one of the

Figure 54. Histogram of Effective Prestress for Span 5 for May 2019 to April 2021 Events With Corresponding Crack Openings of 0.0004 in or Greater
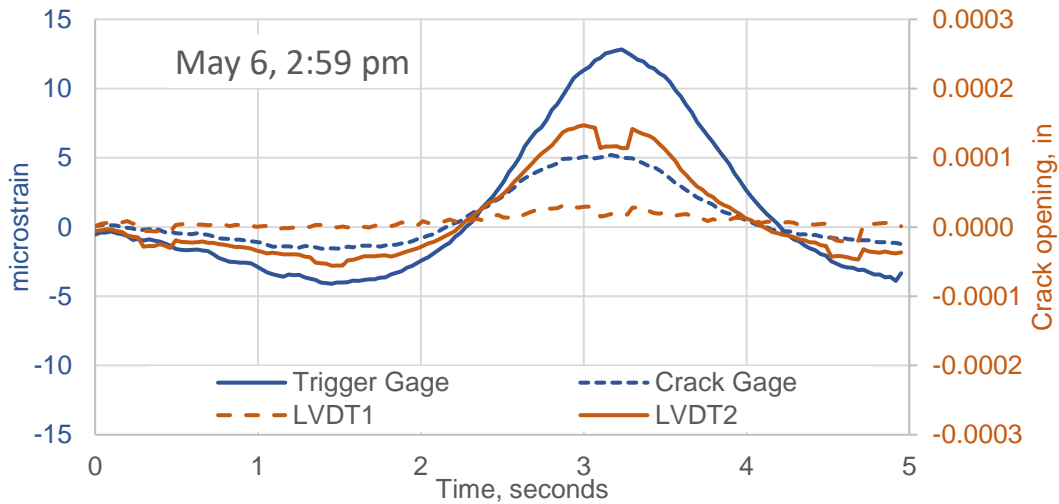
Figure 55. Span 9 Typical Event. LVDT = Linear Variable Differential Transformer


Figure 56. Span 9 Large Event. LVDT = Linear Variable Differential Transformer

larger opening event for Span 9, where the average web temperature was 79.8°F and the difference between the top slab and average web temperature was 16.4°F. The crack width opening for this event was almost ten times higher than the one shown in Figure 55, even though the vehicles that triggered both events caused almost exactly the same strain at the trigger gage. The higher average temperature and temperature differential resulted in a much wider crack opening.

One consistent characteristic of the plots of Span 9 events was the smaller than expected strain in the crack gage. According to Figure 35, the live load moment at the crack (Section D-D) was about 97% of the moment at the trigger gage (Section E-E). The data, however, showed that the strains measured by the gage at the crack were consistently less than 50% of the strain at the trigger gage. This lower-than-expected strain indicated that the crack might not have completely closed nor allowed the development of the fully-expected tension in the concrete adjacent to it.

There were 1300 events in this time period. The magnitudes of the crack openings in Span 9 compared to the back-calculated prestress are presented in Figure 57 for all events, with a mean effective prestress of 155 ksi and a standard deviation of 5.7 ksi. The crack openings in Span 9 were also quite small compared to Span 6, and a threshold crack width 0.0004 in was chosen to reduce the data set. This value was chosen based on the crack width in Figure 57 where the data began to exhibit less scatter. The reduced data set had 92 events with a mean of the effective prestress of 163 ksi and a standard deviation of 3.7 ksi. Figure 58 presents the histogram of the reduced data.
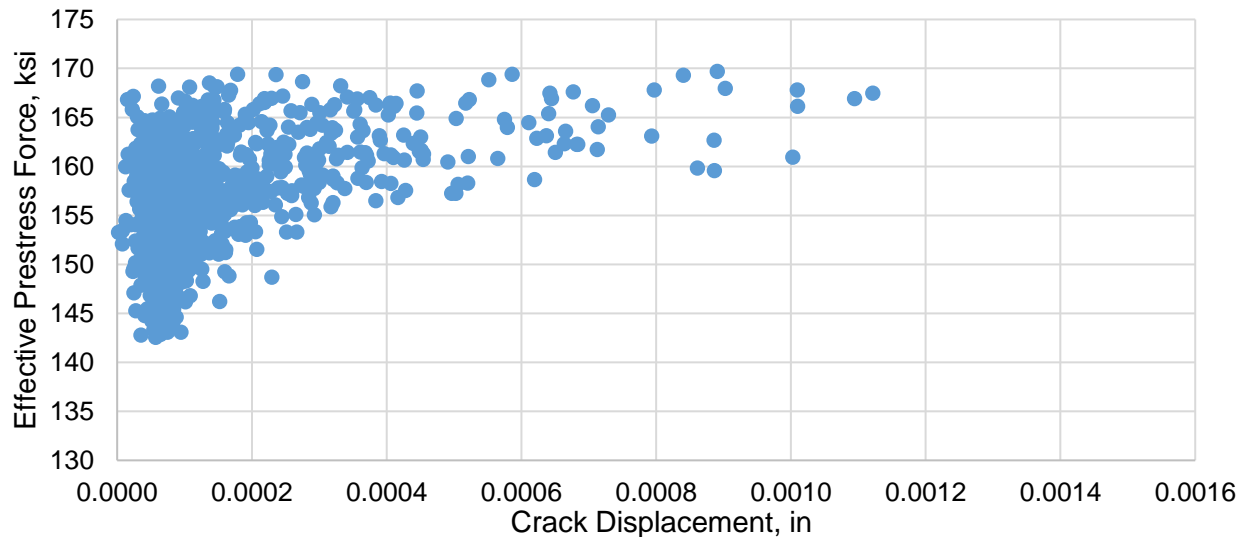

Figure 57. Effective Prestress Versus Crack Opening for Span 9 for March 2020 to June 2020

Span 11

The data acquisition system was moved to Span 11 in June of 2020 and monitored the crack openings and strains until the end of the project. Figure 59 presents a typical event in Span 11 with a significant crack opening. At the time of this event, the average web temperature was 88.4°F and the difference between the top slab and average web temperature was 17.8°F.
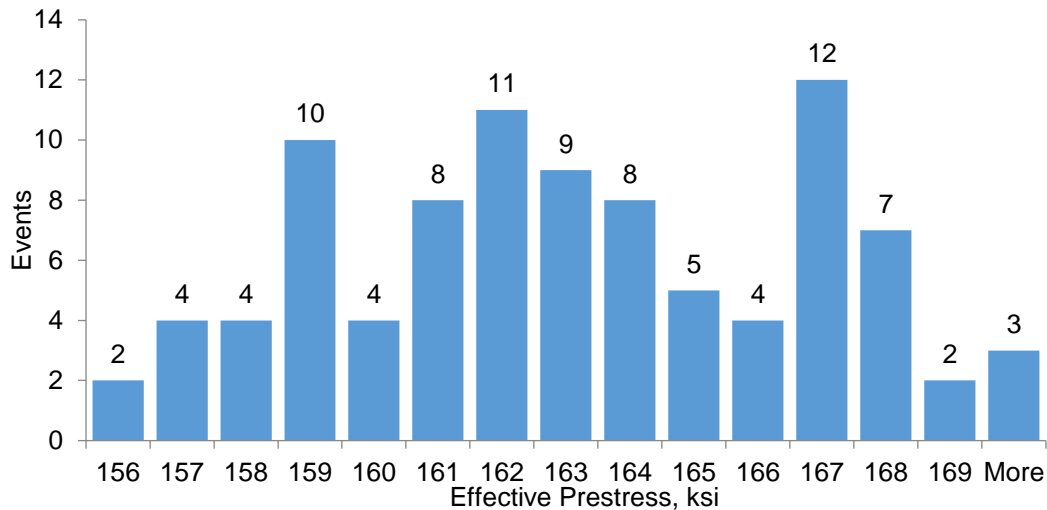
Figure 58. Histogram of Effective Prestress for Span 9 for March 2020 to June 2020 Events with Corresponding Crack Openings of 0.0004 in or Greater
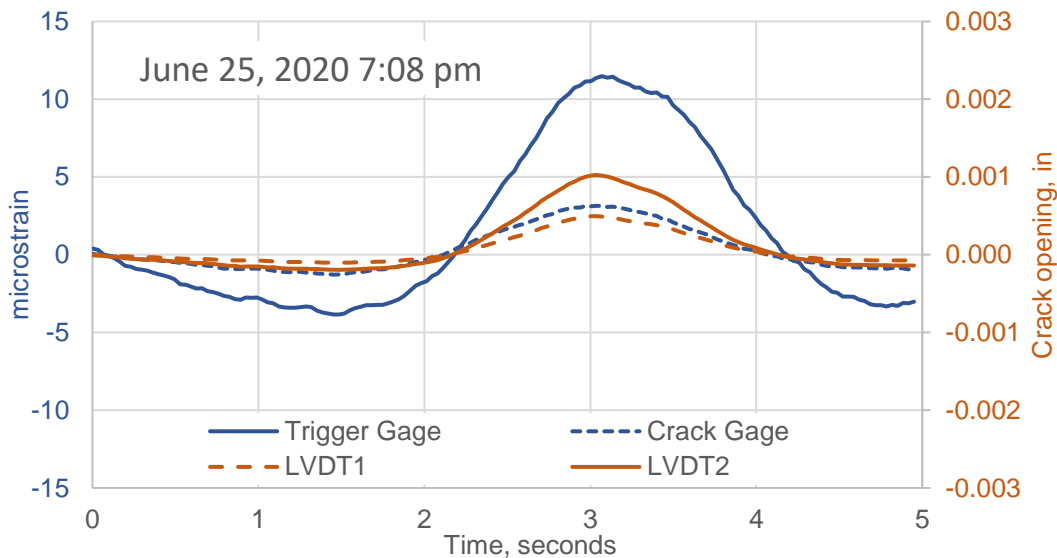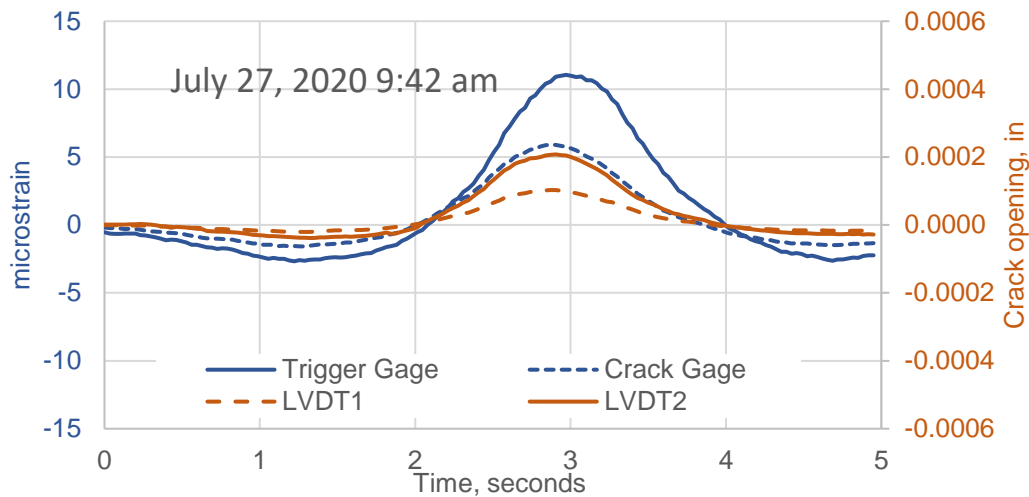

Figure 59. Span 11 Large Crack Opening Event. LVDT = Linear Variable Differential Transformer

The two LVDTs measured a somewhat different crack opening, but this could have been partially attributed to a slightly different gage length for the two gages. The LVDTs measure the crack opening plus any change in length in the concrete between the points where the LVDT is anchored. A larger gage length will include more concrete elongation. This will not be a significant difference for large crack openings, but could affect very small openings. Another observation is that the difference between the strain measured by the trigger gage and that measured by the gage adjacent to the crack was large (12 με compared to 3 με), while the analysis indicated that moment at the crack gage was about 91% of the moment at the trigger gage (see Figure 36). As in Span 9, this discrepancy indicated that the crack was already present and that there was very little compression across the crack before the truck crossed. Thus, any tension that tried to develop in the bottom slab across the crack did not register in the adjacent concrete because the crack opened with very little positive moment from the truck. Once the crack opened, the gage adjacent to the crack did not detect any additional increase in tension.

51

Figure 60 presents an event with a small crack opening. At the time of this event, the average web temperature was 91.1°F and the difference between the top slab and average web temperature was 3.3°F. Even though the event caused approximately the same strain in the trigger gage as the event in Figure 59, the crack only opened 0.0002 in, or one fifth of the opening in the cooler event. Also note that the strain in the gage adjacent to the crack was somewhat higher, meaning slightly more tension was transmitted across the crack, compared to the event in Figure 59.


Figure 60. Span 11 Small Crack Opening Event. LVDT = Linear Variable Differential Transformer

There were 7580 events in this time period. The magnitudes of the crack openings in Span 11 compared to the back-calculated prestress are presented in Figure 61 for all events. The mean effective prestress for all events was 158 ksi, with a standard deviation of 4.0 ksi. As in Span 9, the data set was reduced to only include those events with a crack opening larger than 0.0004 in. The reduced data set had 1150 events with a mean of the effective prestress of 163 ksi and a standard deviation of 2.9 ksi. Figure 62 presents the histogram of the reduced data, which approximates a normal distribution.
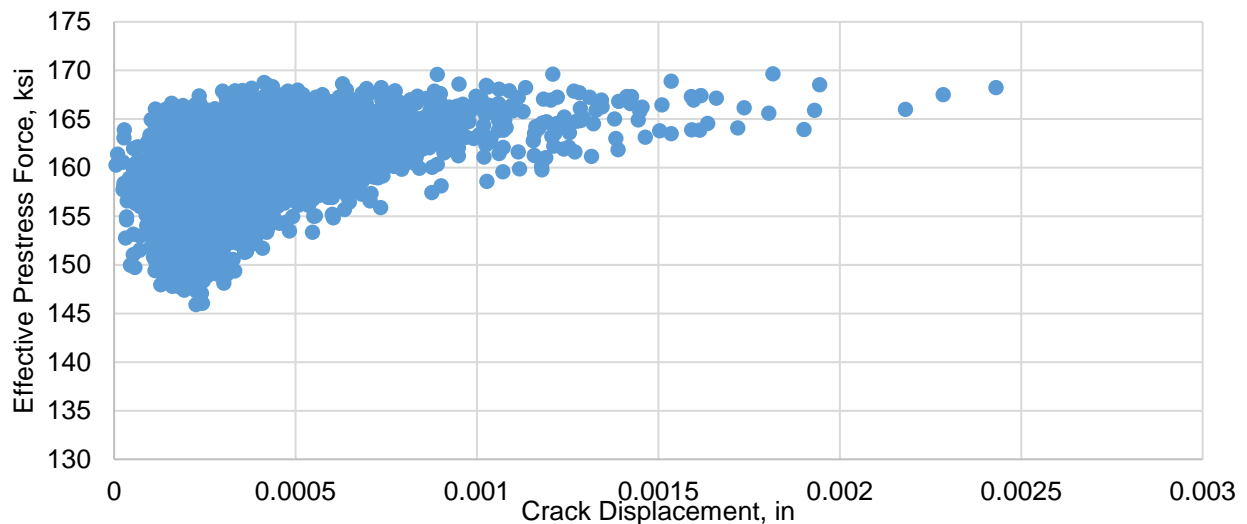
Figure 61. Effective Prestress Versus Crack Opening for Span 11 for June 2020 to April 2021

52
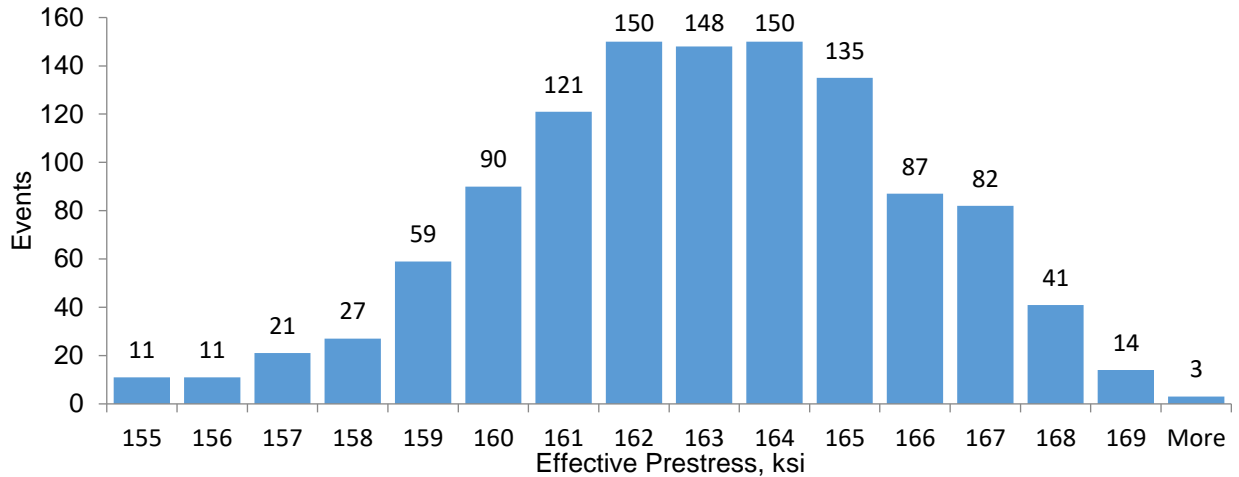
Figure 62. Histogram of Effective Prestress for Span 11 for June 2020 to April 2021 Events with Corresponding Crack Openings of 0.0004 in or Greater

Summary of Field Data Results

Table 8 summarizes the results of the effective prestress back-calculated for each span using field data in Equation 9. Span 6 results are presented separately for 2013 and 2019-2021, but show that the data was quite consistent between the two data sets. This indicates that the effective prestress is stable and not decreasing significantly with continued creep and shrinkage. Span 5, Span 9 and Span 11 effective prestress is somewhat smaller than Span 6, but crack width openings are significantly smaller. The determination of the threshold crack opening has a significant effect on the effective prestress mean.

Table 8. Summary of Effective Prestress Back-Calculated Using Field Data in Equation 9

Span	All Events			Reduced Events		
	Number of Events	Average Effective Prestress	Standard Deviation	Number of Events	Average Effective Prestress	Standard Deviation
Span 5	14,500	148 ksi	6.6 ksi	128	161 ksi	3.5 ksi
Span 6 – 2013	6,697	154 ksi	6.7 ksi	576	166 ksi	2.5 ksi
Span 6 2019-2021	15,370	153 ksi	5.9 ksi	301	166 ksi	2.5 ksi
Span 9	1,300	155 ksi	5.7 ksi	92	163 ksi	3.7 ksi
Span 11	7,580	158 ksi	4.0 ksi	1,150	163 ksi	2.9 ksi

53

Comparison of Field-Determined Effective Prestress to Other Models

In this section the effective prestress back calculated from the field data is compared to effective prestress determined with the LARSA 4D model and several methods to estimate creep and shrinkage.

Finite Element-Modeled Prestress Losses

Four time-dependent, staged-construction analyses over the life span of the structure were conducted on the FE model. The average tendon-stress profiles for these analyses are shown in Figure 63 for Span 6 along with the average tendon stress profile before any long-term losses occurred. The presented stresses are the component in the longitudinal direction of the bridge. From the construction documents, the average jacking force in Span 6 was 879 kips, resulting in average jacking stress of 213 ksi, which was the starting point for the analysis. All analyses, except the CEB-FIP '78 model, were run assuming a relative humidity of 70%, per the AASHTO Specifications. The CEB-FIP '78 model was run with the assumptions given on the design drawings, which indicated an assumption of 80% relative humidity.
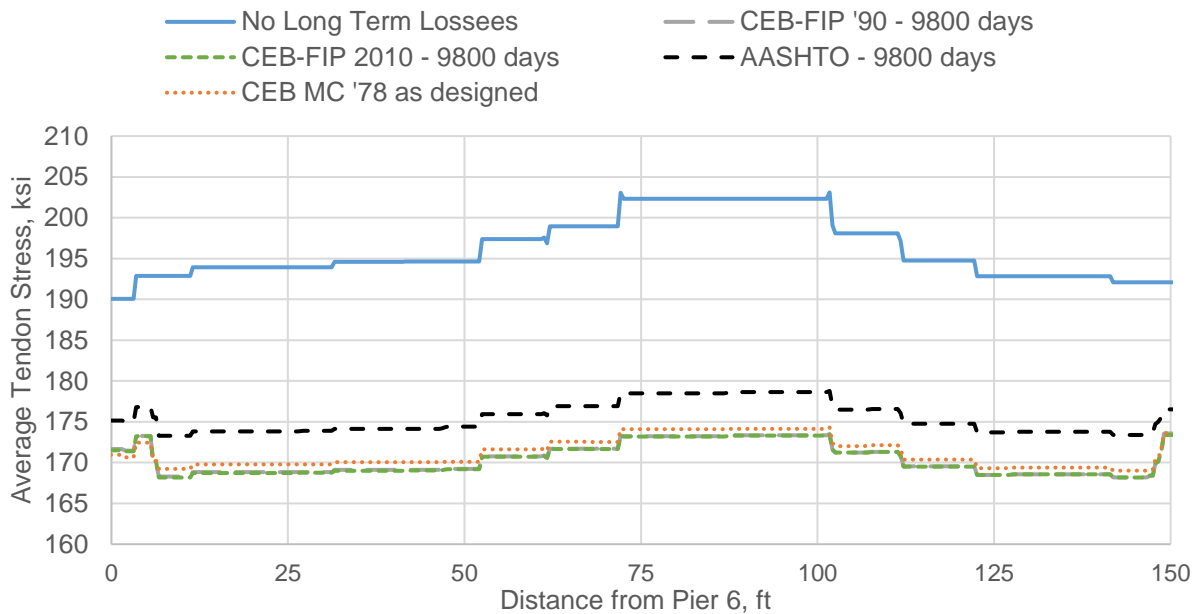

Figure 63. Span 6 Tendon Stress Profiles Taken at 9,800 days.

The original design of the VEB utilized the CEB-FIP '78 model code expression for creep and shrinkage to estimate long-term prestress losses. The average effective prestress at Section A-A using this code expression was 170 ksi. This value represents what the engineers would have expected when the bridge was designed in 1986. The effective prestress estimation from the analysis at Section A-A utilizing the CEB-FIP '90 code expression was 169 ksi, using the CEB-FIP 2010 was 169 ksi and using the AASHTO Specifications was 174 ksi.

The FE model was also used to estimate the projected prestress loss at the age of 50 and 100 years. This progression of effective prestress over time can be seen in Figure 64 for Span 6 for ages up to 20,000 and 36,000 days (approximately 50 and 100 years respectively). In

addition, the effective prestress was estimated for 2013 (9800 days) and 2020 (12,000 days) to compare to measurements. The estimated change in effective prestress over this period was very small for all models. The results of the analysis using each model is presented in Table 9. Also note that, for all models, by 2013, over 90% of all prestress loss has already occurred.

A comparison of the results from the FE analyses calculations and calculations done using field data at 12,000 days is shown in Table 10. Day zero was August 8, 1987; therefore, day 12,000 was around June 23, 2020. Results are shown for the original model used in design, the CEB-FIP '78, and for more modern creep and shrinkage models, CEB-FIP '90 and CEB-FIP 2010, and AASHTO (2017).
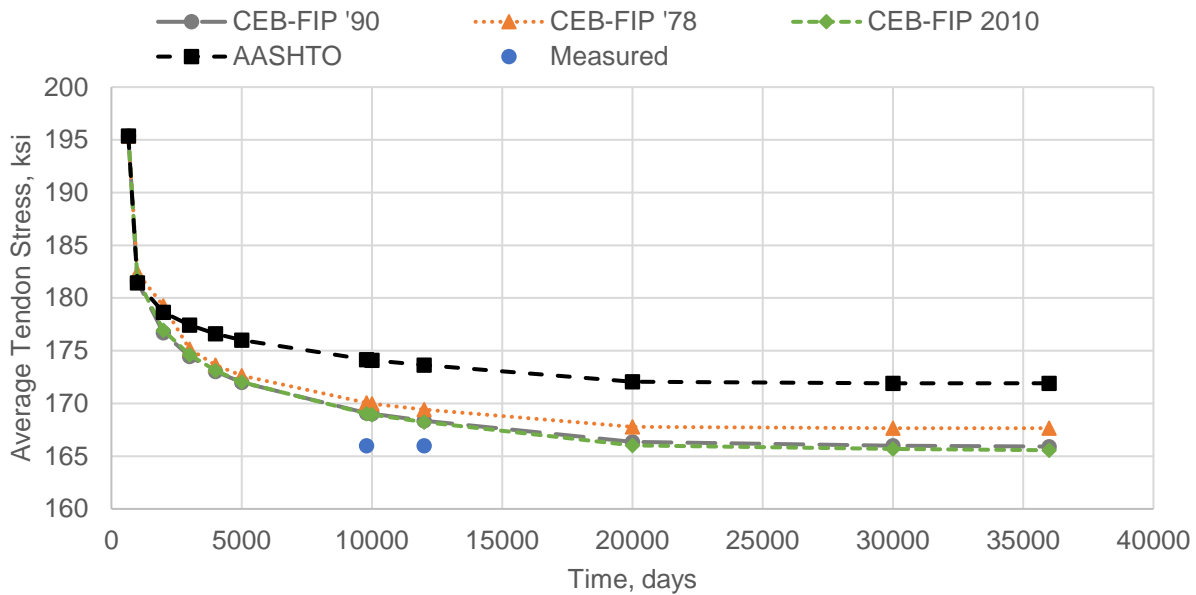

Figure 64. Progression of Prestress Loss With Time, at Section A-A of Span 6. Note that CEB MC '78 was the original design model

Table 9. Comparison of Effective Prestress Estimations at Older Ages for Span 6 at Section A-A

Model	Effective Prestress Estimate (ksi) in Span 6 at Age-			
	26 years (2013)	33 years (2020)	50 years (2037)	100 years (2087)
AASHTO (2017)	174	173	172	172
CEB-FIP '78	170	169	168	168
CEB-FIP '90	169	168	166	166
CEB-FIP 2010	169	168	166	166

Table 10. Comparison of Effective Prestress Estimations from Field Data and FE Analysis at Day 12,000 (year 2020)

Span	$P_{e\,data}$ (ksi)	CEB-FIP '78		CEB-FIP '90		CEB-FIP 2010		AASHTO (2017)	
		$P_{e\,model}$ (ksi)	Model Data	$P_{e\,model}$ (ksi)	Model Data	$P_{e\,model}$ (ksi)	Model Data	$P_{e\,model}$ (ksi)	Model Data
5	161	171	1.06	170	1.06	169	1.05	175	1.09
6	166	169	1.02	168	1.01	168	1.01	173	1.04
9	163	171	1.05	170	1.04	168	1.03	175	1.07
11	163	171	1.05	170	1.04	169	1.04	175	1.07

As can be seen in the table, all of the CEB-FIP creep and shrinkage models provided reasonable predictions of the effective prestress, just slightly higher than that which was determined using measured strains. The AASHTO creep and shrinkage model gave the highest predicted effective prestress.

Based on a jacking stress of 213 ksi, the prestress loss predicted by the CEB-FIP '90 code was, on average, 44 ksi after 33 years of service. This is 21% of the original jacking stress, which is similar to the 24% loss predicted by Bažant et al. (2010) for the Koror-Babeldaob Bridge after 27 years, using the same CEB-FIP '90 (see Figure 25). The losses in the Varina-Enon Bridge are considerably smaller than the almost 50% loss predicted for Koror-Babeldaob using the B3 or B4 model. This would indicate that the excessive prestress loss seen in the Koror-Babeldaob Bridge and other long span bridges studied by Bažant et al. (2012) is not occurring in the Varina-Enon Bridge.

When considering prestress loss, two major serviceability concerns arise. The first concern is that cracking of the structure will cause accelerated deterioration due to moisture infiltration. In the case of the VEB, this is of little concern because the tendons are fully grouted and encapsulated in HDPE ducts. The second concern is that of deflections. In this regard also, there are no concerns with the VEB itself. In the worst-case FE analysis, deflection results indicate that the VEB has experienced less than 1/2 in of additional deflection from its original camber, and all models indicate that very little additional deflection will occur over time.

Estimate Future Losses and the Effect on Flexural Strength

The effective prestress determined from field data and that predicted by the original design model, CEB-FIP '78, were used to calculate the flexural strength at the mid-span of each of the monitored spans.

Table 11 presents the results of these calculations using the effective prestress at 12,000 days. Using the CEB-FIP '78 model of effective prestress overestimated the flexural strength by only 1-3%, relative to the field data-determined effective prestress. The additional loss that occurs from 12,000 days to 36,000 days will not significantly reduce the flexural strength.

Table 11. Comparison of Calculated Flexural Strength Using CEB-FIP '78 Code Versus Field Measurements

Span	Effective Prestress to Calculate Flexural Strength						$\dfrac{M_{n\ measured}}{M_{n\ CEB\text{-}FIP\ '78}}$
	CEB-FIP '78			Measured			
	f_{pe}, ksi	f_{ps}, ksi	M_n, k-ft	f_{pe}, ksi	f_{ps}, ksi	M_n, k-ft	
5	171	235	85,890	161	225	82,300	0.96
6	169	233	85,260	166	230	84,180	0.99
9	171	235	85,890	163	227	83,010	0.97
11	171	235	85,530	163	227	83,010	0.97

Compare Design Thermal Gradients to Measured

      The thermocouple readings were analyzed to determine the maximum positive thermal gradients during the monitoring period for comparison with the current design gradient for the Richmond area per the AASHTO LRFD Specification and the original linear design gradient. Figures 65 and 66 present large thermal gradients from 2014 and 2019 respectively. In each figure, a fifth order parabola provided a good fit to the data, and hence, was used to extrapolate the temperature at the top surface of the bridge. There is somewhat more scatter in the web temperatures in Figure 66 compared to Figure 65. In the pairs of thermocouples in the web, the lower of each pair was closer to the exterior face of the box, and the higher closer to the interior face. In Figure 66, the outside thermocouples are slightly cooler than the inside, which could be due to a breezy day, or the shadow of the overhang keeping the outside cooler.
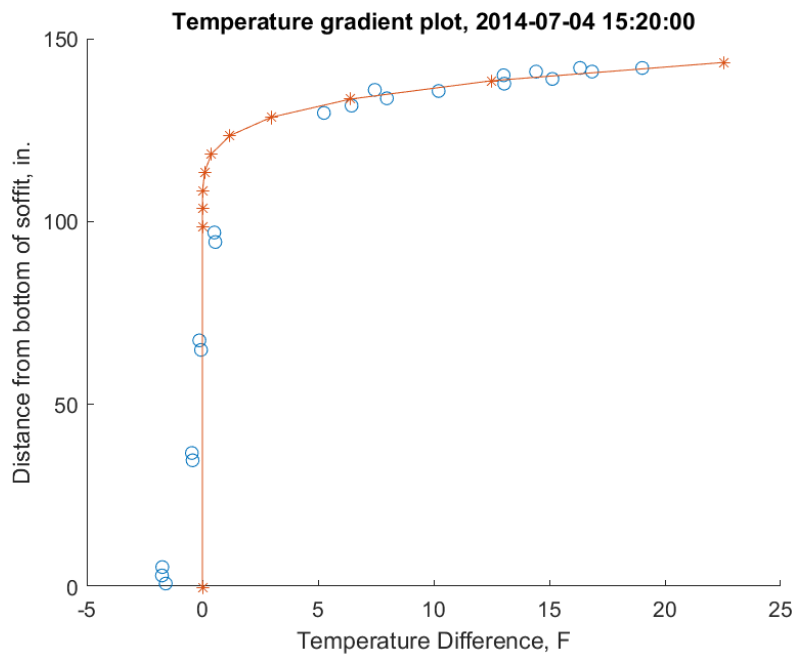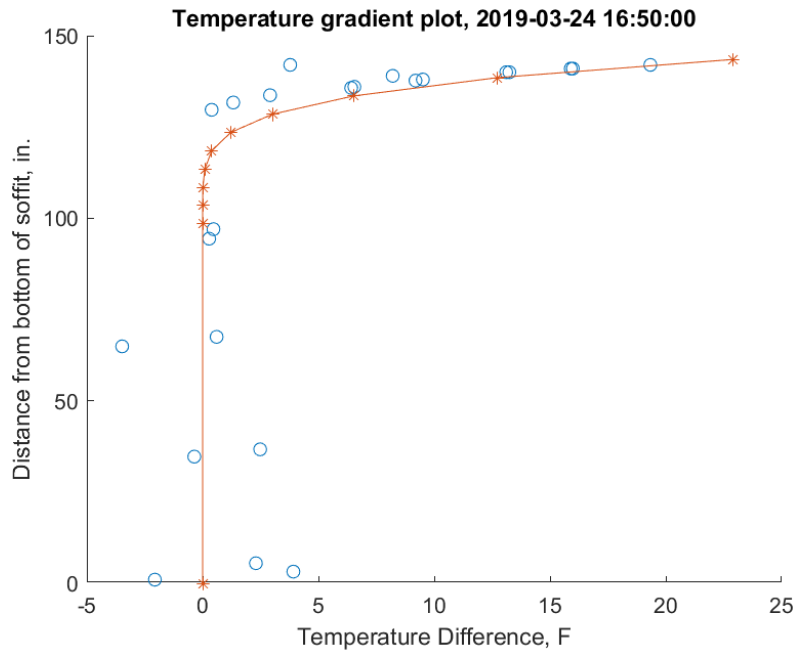

Figure 65. Thermocouple Readings from July 4, 2014, and 5ᵗʰ Order Parabolic Fit

Figure 66. Thermocouple Readings from March 24, 2019, and 5th Order Parabolic Fit

Using the fifth order parabola extrapolation, the maximum positive temperature differentials between the warmest temperature on the top of the bridge and the average temperatures in the webs were determined, as presented in Figures 67 and 68 for 2014 and 2020, respectively. As can be seen in the figures, the maximum temperature difference was less than 30°F for both years, which was considerably smaller than the 41°F design temperature difference for the Richmond area, as prescribed by AASHTO (See Figure 22). However, the difference was much higher than the temperature difference used for the original design, which was an 18°F
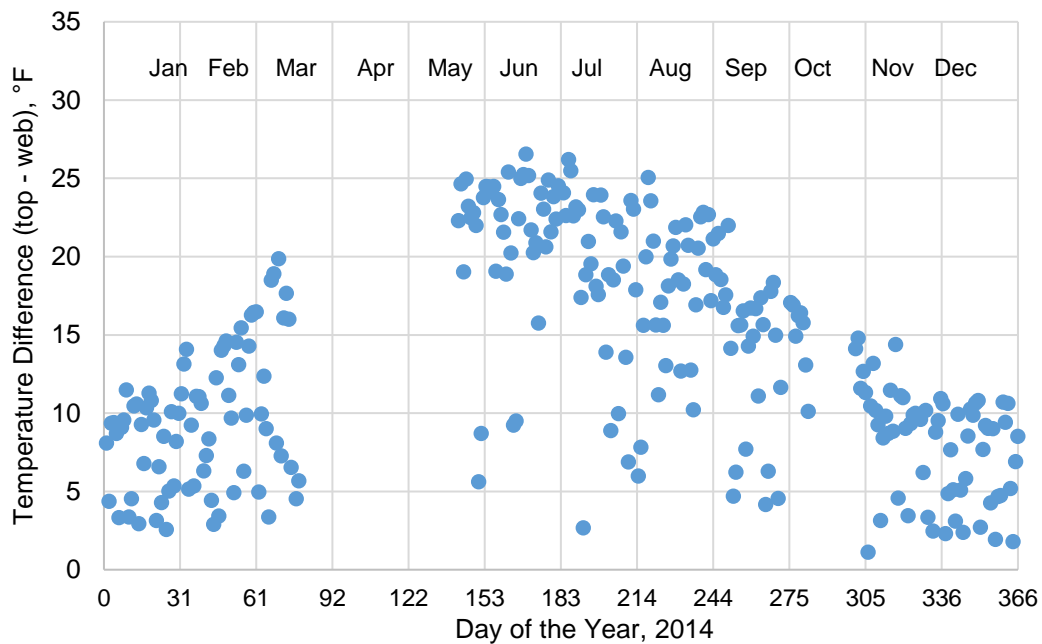
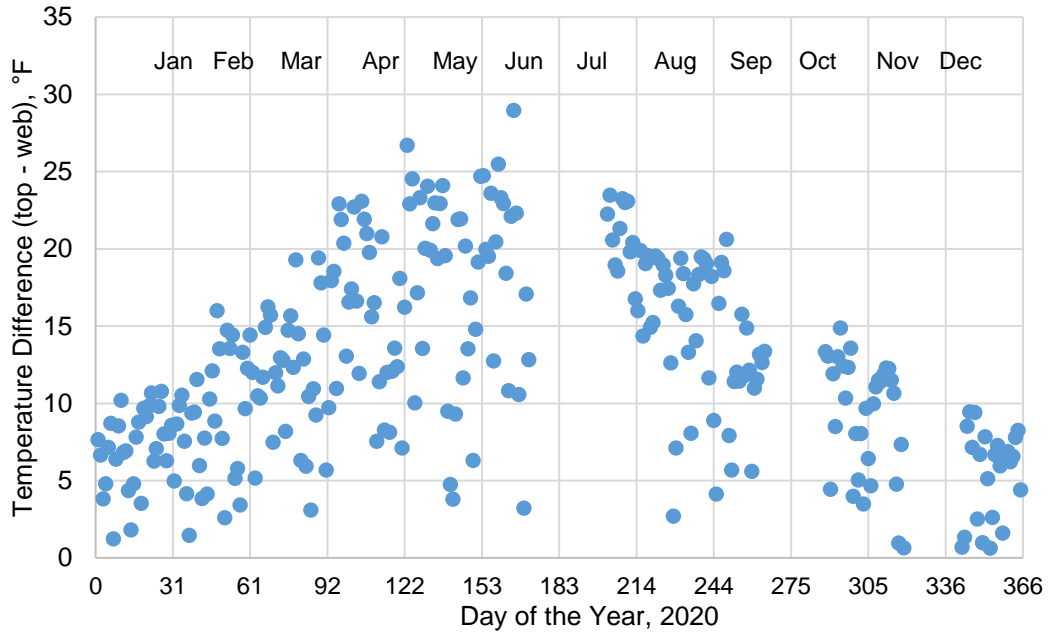**Figure 67. Maximum Daily Thermal Differentials for 2014**

58

Figure 68. Maximum Daily Thermal Differentials for 2020

differential that varied linearly between the top slab and the bottom of the box. Figure 69 compares the current AASHTO thermal gradient, the design thermal gradient, and one of the highest measured gradients during the study. Although the slope of the current AASHTO gradient is much steeper than the measured gradient at the top of the girder, the total moment to restrain the curvature (as calculated using Equation 12) was not substantially different. Table 12 presents the restraint force and restraint moment for each of the three gradients. The original design gradient resulted in a smaller restraint moment than that which was calculated using the recorded temperature data.
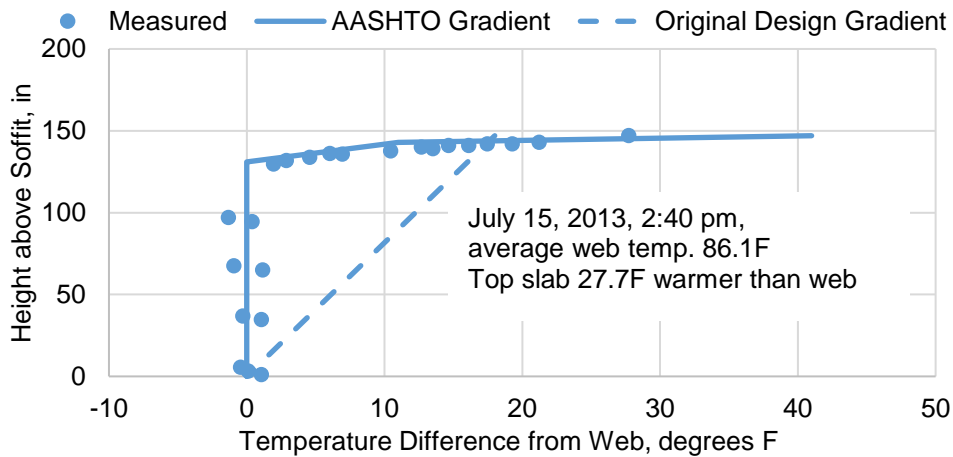

July 15, 2013, 2:40 pm,
average web temp. 86.1F
Top slab 27.7F warmer than web

Figure 69. Maximum Thermal Gradient Compared to Design Gradients

59

Table 12. Moments and Forces to Restrain Girder Subjected to Thermal Gradients

Thermal Gradient	Restraint Axial Force (kips)	Restraint Moment (kip-ft)
Maximum from Data	3819	10186
Current AASHTO Design	3373	10170
Original Design	5310	9980

CONCLUSIONS

- *The assumptions and methods used to calculate the effective prestress via crack opening observations on in-service structures are valid, as verified by the FE model.* The FE estimates more closely align with field data-based calculations when events with small crack openings are excluded.

- *The largest crack openings occurred in Span 6, which is an end span in a six-span continuous unit.* The other three monitored spans are interior spans, and it is possible that the restraint from adjacent spans or stiffer bearing conditions restrict the crack opening.

- *The effective prestress determined from the field data was only slightly smaller than what had been originally assumed when the structure was designed.* At 12,000 days, the effective prestress determined using the original creep and shrinkage model was 2-6% higher than the effective prestress determined from field data. Using the effective prestress from field data, the calculations showed the flexural capacity was only 1-4% smaller than the original design calculation.

- *The average web temperature (through the thickness of the web) and thermal gradient (through the depth of the section) occurring at the same time as large live load events have a substantial effect on the response of the bridge.* Large crack openings typically occur when a large positive thermal gradient and high average web temperatures exist at the same time as the heavy load.

- *Although the different design thermal gradient inputs can vary widely, the resulting restraint moments calculated using those various thermal gradients are very similar.* However, the original design thermal gradient resulted in a larger restraint axial force as compared to more current design gradients as well as gradients determined using field instrumentation. Depending on the amount of longitudinal restraint provided by the bearing pads in design calculations, this could have resulted in less calculated tension for the design thermal gradient.

- *Based on FE analysis, future prestress loss in the VEB does not appear to be of significant concern.* Finite element analysis results indicate that the vast majority of prestress loss had already occurred by 2013. All creep and shrinkage models investigated (CEB-FIP '78, CEB-FIP '90, CEB-FIP 2010 and AASHTO) indicate that over 90% of the total losses had occurred by 2013. The literature suggests that our current code expressions for creep and shrinkage do not adequately represent the progression of these phenomena at old ages. Three of the code expressions used in this study assumed a bounded time-development of creep, but research by Bazant et al. has shown that this is not the case.

- *Contrary to previous research presented in Bažant et al. (2010) and Bažant et al. (2012), the prestress losses in the Varina-Enon Bridge do not seem to be excessive compared to design values. In addition, any further changes in effective prestress due to creep and shrinkage are expected to be very small for this structure, which is of an advanced age.* Results from the long-term monitoring system indicate that the change in average prestress from 2013 to 2019-21 in Span 6 is essentially zero. The bridge was 26 years old in 2013 and 33 years old in 2020.

RECOMMENDATIONS

1. *VDOT's Richmond District should continue to monitor key locations in the Varina-Enon Bridge.* Although the research presented herein does not indicate any great cause for concern, monitoring can detect if effective prestress should drop significantly due to wire or strand breakage from corrosion. The prestress loss should continue to be monitored in order to assess the rate at which prestress loss progresses. Since only Span 6 was instrumented in 2013, it is unknown if the other locations also have negligible decrease in effective prestress. This progression should then be compared to current model codes. In order to determine the effective prestress, the cracks in Span 6 as well as other crack locations that have been identified should be monitored in a similar fashion to Spans 9 and 11 in this study.

2. *VDOT's Richmond District should support a more detailed investigation of the influence of the average web temperature on the behavior of the Varina-Enon Bridge, including the differences between the responses of Span 6 compared to the other spans.* Only Span 6 showed the obvious decompression at the joints along with large crack openings. Events with similar live loads and temperature differentials can result in very different responses if the average web temperature is different. This difference in behavior could be due to the magnitude of the restraint forces at the supports. The more sophisticated model developed based on the third recommendation could also be used to probe the reasons why warmer web temperatures result in wide crack openings.

3. *VTRC should support the development of a refined analytical model that improves the predicted prestress losses due to creep and shrinkage.* Ideally, this model can be incorporated into LARSA; however, a different finite element program that can also support Bažant's B4 model may need to be used. While the new model should be applicable to the Varina-Enon Bridge, the model should also be capable of assessing the current condition of other structures.

IMPLEMENTATION AND BENEFITS

Researchers and the technical review panel (listed in the Acknowledgments) for the project collaborate to craft a plan to implement the study recommendations and to determine the benefits of doing so. This is to ensure that the implementation plan is developed and approved with the participation and support of those involved with VDOT and DRPT operations. The implementation plan and the accompanying benefits are provided here.

Implementation

Regarding *Recommendation 1*, VDOT's Richmond District will continue monitoring key locations in the Varina-Enon Bridge through a contract with a structural health monitoring consultant. Installation of the monitoring equipment is set to start in February 2022 and completed by July 2022.

Regarding *Recommendation 2*, Richmond District is satisfied with the updated effective prestress information provided in this report in order to conduct a load rating of the Varina-Enon Bridge. Additional information regarding the average web temperature will likely only enable minor improvements in the modeling of the structure, and thus there would be no substantial changes in the load rating based on this supplementary data. Therefore, there is no need for further action regarding this recommendation.

Regarding *Recommendation 3*, the PI for this current project presented a research needs statement for refined creep and shrinkage modeling at the fall 2021 meeting of the Bridge Research Advisory Committee. Prioritization of BRAC-related research needs, including this topic, is forthcoming. In any event, there is no need for further action regarding this recommendation.

Benefits

Establishing a monitoring program will help to capture small changes that might be imperceptible during conventional bridge safety inspections. In addition, having a better understanding of how much of a role temperature has when large, visible cracks do occur could further alleviate concerns about live loads forcing restrictions on, or even closure of, the bridge. Thus, implementing the above recommendations will certainly help to ensure the safety of the signature Varina-Enon Bridge. Specifically, *Recommendations 1 and 2* will provide additional data that will help to refine the existing LARSA model, which suggests that the Varina-Enon Bridge is more flexible than it actually is. Also, the additional data will help to ensure that the main spans are modeled properly, which is a concern for the district.

Looking more systemically, there are large prestressed and post-tensioned concrete structures in the commonwealth other than the Varina-Enon Bridge, such as the I-895 Bridge over the James River and I-95 in Henrico County, the Lee Bridge in Richmond City, the Rte. 460 Bridge over Grassy Creek in Buchanan County, and the Wilson Creek Bridge (Smart Road Bridge) in Montgomery County. Excessive creep and shrinkage in these structures can lead to less tension in the prestressing tendons than what was in the original design. This lower tension can lead to greater cracking in primary load-carrying members, which would allow for greater ingress of chlorides, which would further exacerbate the deterioration of the concrete and reinforcement. Implementing *Recommendation 3* could help bridge engineers have a better understanding of the prestress forces in these types of structures over the long term, and thus ensure enhanced safety, greater durability, and lower life-cycle costs of these assets.

ACKNOWLEDGMENTS

REFERENCES

AASHTO. AASHTO LRFD Bridge Design Specifications. American Association of State Highway and Transportation Officials, Washington, DC, (2017).

ACI Committee 423. Guide to Estimating Prestress Losses. American Concrete Institute, Farmington Hills, MI. 2016.

Attanayake, U. and Atkan, H. Capacity Evaluation of a Severely Distressed and Deteriorated 50-Year-Old Box-Beam with Limited Data. Journal of Performance of Constructed Facilities, Vol. 25, No. 4, Aug 2010, pp. 229-308.

Azizinamini A., Keeler, B.J., Rohde, J., and Mehrabi, A.B. Application of a New Nondestructive Technique to a 25-Year-Old Prestressed Concrete Girder. PCI Journal, Vol. 41. No. 3, May-June 1996, pp. 82-95.

Bažant, Ž. P. and Baweja, S. Creep and Shrinkage Prediction Model for Analysis and Design of Concrete Structures: Model B3. Materials and Structures, Vol. 28, 1995, pp. 357-365.

Bažant, Ž. P., and Jirasek, M. Creep and Hygrothermal Effects in Concrete Structures, Springer Science+Business Media B.V., Dordrecht, The Netherlands, 2018.

Bažant, Ž. P., Yu, Q., Li, G.-H., Klein, G. J., and Křístek, V. Excessive Deflection of Record-Span Prestressed Box Girder. Concrete International, Vol. 32, No. 6, June 2010, pp 44-52.

Bažant, Ž. P., Yu, Q. and Li, G-H. Excessive Long-Time Deflections of Prestressed Box Girders. I: Record-Span Bridge in Palau and Other Paradigms. ASCE Journal of Structural Engineering, Vol. 138 No. 6, June 2012, pp. 676-686.

Brodsky, Rachel A. Effective Prestress Evaluation of the Varina-Enon Bridge Using a Long-Term Monitoring System and Finite Element Model. MS Thesis, Virginia Tech, Blacksburg, VA, 2020.

CEB-FIP. fib Model Code for Concrete Structures 1978. Wilhlem Ernst and Sohn, Berlin, Germany, 1978.

CEP-FIP. fib Model Code for Concrete Structures 1990. Wilhlem Ernst and Sohn, Berlin, Germany, 1990.

CEB-FIP. fib Model Code for Concrete Structures 2010. Wilhlem Ernst and Sohn, Berlin, Germany, 2013.

Dahiya, A. Long-Term Monitoring and Evaluation of the Varina-Enon Bridge, MS Thesis, Virginia Tech, Blacksburg, VA, 2021.

F&M Engineers, Inc. "Owner's Manual for Inspection and Maintenance of Segmental Concrete Approach and Main Span." Varina-Enon Bridge Prepared for Virginia Department of Transportation, 1993.

Garber, D. B., Gallardo, J. M., Deschenes, D. J., and Bayrak, O. Experimental Investigation of Prestress Losses in Full-Scale Bridge Girders. ACI Structural Journal, Vol. 112, No. 5, May 2015, pp. 553-564.

Greuel, A., Rogers, B.T., Miller, R.A., Shahrooz, B.M. and Baseheart, T.M. Evaluation of a High Performance Concrete Box Girder Bridge. PCI Journal, Vol. 45, No. 6, Nov-Dec. 2000, pp. 60-71.

Halsey, J. T., and Miller, R. Destructive Testing of Two Forty-Year-Old Prestressed Concrete Bridge Beams. PCI Journal, Vol. 41, No. 5, Sept-Oct 1996, pp. 84-93.

Imbsen, A., Vandershaf, D.E., Schamber, R.A. and Nutt, R.V. Thermal Effects in Concrete Bridge Superstructures. NCHRP Report 276, Transportation Research Board, National Research Council, Washington, D.C., 1985.

Kukay, B.M. Bridge Instrumentation and the Development of Non-Destructive and Destructive Techniques Used to Estimate Residual Tendon Stress in Prestrssed Girders. All Graduate Theses and Dissertations, Paper 128, Utah State University, Logan, Utah, 2008.

Labia, Y., Saiidi, M. S., and Douglas, B. Full-Scale Testing and Analysis of 20-Year-Old Pretensioned Concrete Box Girders. ACI Structural Journal, Vol. 94, No. 5, May 1997, pp. 471-482.

Larsa 4D. (2019). Larsa 4D Reference Manual. https://www.larsa4d.com/download/larsa4d_referencemanual.pdf

Lindley, S. M. Investigation of the Time-Dependent Longitudinal Flexural Behavior of the Varina-Enon Bridge. MS Thesis, Virginia Tech, Blacksburg, VA, 2019.

MacGregor, R.J.G. Strength and Ductility of Externally Post-tensioned Segmental Box Girders, PhD Dissertation, The University of Texas at Austin, Austin, TX, 1989.

Maguire, M. Transverse and Longitudinal Bending of Segmental Concrete Box Girder Bridges. PhD Dissertation, Virginia Tech, Blacksburg, VA, 2013.

Maguire, M., Moen, C. D., Roberts-Wollmann, C., and Cousins, T. Field Verification of Simplified Analysis Procedures for Segmental Concrete Bridges. Journal of Structural Engineering, Vol. 141, No. 1, Jan. 2015.

Maguire, M., Roberts-Wollman, C. L., and Cousins, T. Live Load Test and Long Term Monitoring of the Varina-Enon Bridge. Final report to the Virginia Transportation Research Council, Charlottesville, VA, 2014.

Maguire, M., Roberts-Wollmann, C., and Cousins, T. Live-Load Testing and Long-Term Monitoring of the Varina-Enon Bridge: Investigating Thermal Distress. Journal of Bridge Engineering, Vol. 23, No. 3, March 2018.

Naaman, A. E. Prestressed Concrete Analysis and Design, Techno Press 3000, Ann Arbor, MI, 2012.

OPAC. "Koror-Babeldoab Bridge." <https://www.opacengineers.com/projects/Koror>, accessed May 2000.

Osborn, G. P., Barr, P. J., Petty, D. A., Halling, M. W., and Brackus, T. R. Residual Prestress Forces and Shear Capacity of Salvaged Prestressed Concrete Bridge Girders. Journal of Bridge Engineering, Vol. 17, No. 2, Feb. 2012, pp. 302-309.

Pessiki, S., Kaczinski, M., and Wescott, H. H. Evaluation of Effective Prestress Force in 28-Year-Old Prestressed Concrete Bridge Beams. PCI Journal, Vol. 41, No. 6, Nov.-Dec. 1996, pp. 78-89.

Priestley, M. J. N. Design of Concrete Bridges for Temperature Gradients. Journal Proceedings, Vol. 75, No. 5, May 1978, pp. 209-217.

Shenoy, C., V., and Frantz, G. C. Structural Tests of 27-Year-Old Prestressed Concrete Bridge Beams. PCI Journal, Vol. 36, No. 5, Sept-Oct 1991, pp. 80-90.

Smith, M. J., and Goodyear, D. A Practical Look at Creep and Shrinkage in Bridge Design. PCI Journal, Vol. 33, No. 3, May-June 1988, pp. 108-121.

Tabatabai, H., and Dickson, T. J. Structural Evaluation of a 34-Year-Old Precast Post-Tensioned Concrete Girder. PCI Journal, Vol. 38, No. 5, Sept-Oct 1993, pp. 50-63.